Diamond Nanostructures at Different Dimensions: Synthesis and Applications

Yao Li, Limin Yang, Xin Jiang, Yang Lu*, Cuiping Han, Yongbing Tang, Nianjun Yang**

Y. Li, Prof. X. Jiang
Institute of Materials Engineering
University of Siegen
Siegen 57076, Germany
E-mail: xin.jiang@uni-siegen.de

L. Yang, Prof. Y. Lu
Nano-Manufacturing Laboratory (NML)
City University of Hong Kong Shenzhen Research Institute
Shenzhen 518057, China
E-mail: ylu1@hku.hk

Prof. Y. Lu
Department of Mechanical Engineering
The University of Hong Kong
Hong Kong 999077, China
E-mail: ylu1@hku.hk

Prof. Yongbing Tang
Advanced Energy Storage Technology Research Center
Shenzhen Institutes of Advanced Technology
Chinese Academy of Sciences
Shenzhen 518055, China

Prof. C. Han
Faculty of Materials Science and Energy Engineering
Institute of Technology for Carbon Neutrality

Shenzhen Institute of Advanced Technology
Chinese Academy of Sciences
Shenzhen 518055, China

Prof. N. Yang
Department of Chemistry
Hasselt University
Dipenbeek 3509, Belgium
E-mail: nianjun.yang@uhasselt.be

Prof. N. Yang
IMO-IMOMEC
Hasselt University
Dipenbeek 3509, Belgium

Keywords: diamond nanostructures, diamane, diamond nanothread, nanotwin diamond, synthesis, applications

Abstract: Diamond materials at different nanoscales provide them various characteristics such as elastic mechanical properties in needle-like nanotips, flexibility of two-dimensional (2D) films having atomic thicknesses and constant hardness under high pressures, superior field electron emission properties of vertically wall-like composites, unprecedented hardness and improved toughness of nanotwin diamond (nt-diamond), while the inherent excellent properties of bulk diamond (e.g., high Young's modulus, robustness, biocompatibility) can be maintained. In this paper, the newly born one-dimensional diamond nanothreads, 2D diamanes, as well as 3D nt-diamond are briefly reviewed. The innovations, progresses and achievements of different dimensional diamond nanostructures, covering lines, planes and volumes are overviewed. The topical problems and future outlooks of diamond nanostructures are outlined and discussed.

1. Introduction

Diamond is one kind of the most fascinating carbon materials, which possesses the highest

Young's modulus, with excellent thermal conductivity, high stability, chemical inertness, good biocompatibility, high resistance to surface fouling, and controllable electronic properties. When doped, it exhibits wide working potential windows as well as low and stable background currents in different solutions. Consequently, the performance exploration of diamond materials (especially those artificially synthesized diamond ones) and their optimization in various fundamental and applications fields have never stopped [1].

Up to date, the methods to synthesize diamond nanostructures mainly cover bottom-up deposition and top-down etching approaches. The bottom-up deposition method refers to the uniform coverage of a diamond layer on a substrate (in most cases with nanostructures). The morphology of the resultant diamond nanostructure is determined by the shape of the applied substrate. The reported substrate materials include one-dimensional (1D) Si nanowires [2], carbon fibers [3], and metal wires [4]; two-dimensional (2D) silicon or other metal wafers [5]; and three-dimensional (3D) copper foam [6]. To deposit a diamond layer on these substrate materials, they must be first of all stable enough to withstand the harsh environment of chemical vapor deposition (CVD) synthesis. Meanwhile, the substrate materials must have a high-quality interface connection with the diamond. In more detail, the thermal expansion coefficient of these substrates must be comparable to that of diamond, and not appearing peeling off [5]. Differently, some substrate materials that are easily etched by H plasma can be protected by surface modification [3a, 6b]. Compared with 2D substrates, deposition of a diamond layer on 1D or 3D substrates can obtain larger specific surface areas. Meanwhile, the adhesion of diamond to the bottom and back of the substrate must be considered. Conversely, the substrate would also brought some changes to the properties of diamond. For example, diamond film deposited on planar Si substrate as known was stubborn. However, when diamond was loaded onto carbon fibers, diamond nanofibers could possess flexibility [7]. What's more, the efficiency of electrosynthesis ability of diamond films on three kinds of substrates, nionium, tantalum and silicon, varied [8]. Evaluation was based on electrosynthesis of chlorine oxoanions and peroxodisulfate with diamond electrodes. The diamond coatings on tantalum substrate lead to higher concentrations of hypochlorite and perchlorate from the electrolysis of synthetic brines. These result was explained in terms of the higher production of hydroxyl radicals during the process with the Ta support. Therefore, in practical applications, the selection of substrate materials should be comprehensively considered.

The top-down etching method is more complicated than the bottom-up one. It is based on the etching of a planar thick diamond film that is grown mostly on the silicon plate substrate. The etching can be carried out by use of plasma [9], air thermal etching [10], and water vapor etching [11]. It can be supplemented with catalytically active metal nanoparticles [12]. For polycrystalline diamond films, slight etching shows that the etched effect of each crystal plane is different, leaving triangular etching pits on the [111] plane, and rectangular pits on the [100] plane [12c, 13]. When the etching time is prolonged and the etching depth is increased, 1D nanowires or nanoneedles can be obtained.

In addition to these two traditional methods, the synthesis of 1D nanothreads [14] and 2D diamanes [15] relies on the phase transformation of sp^2-carbon to sp^3-carbon under high pressures or chemisorption. It must be highlighted here that nanothreads and diamanes are new members of the diamond family. They have been actually proposed only in recent years. The former is based on the longitudinal connection of benzene molecules and the latter is the interlayer connection of single-sided H-coated single-layer graphene. Most of their researches still stay at theoretical levels. For their synthesis experiments, high pressure is usually a must since high pressure can give reactants enough energy to break the energy barrier and form new bonds between molecules.

This review article summarizes the progress and achievements of diamond nanostructures at different dimensions (e.g., 0D, 1D, 2D, 3D diamond nanostructures) mainly in past decades. Their synthesis and applications in various fields have been overviewed and discussed. The topical problems and future outlooks of diamond nanostructures are outlined.

2. 0D and 1D Diamond nanostructures

2.1. Diamond nanoparticles and nanowires

Diamond nanoparticles are referred to as zero-dimensional (0D) material. Diamond nanoparticles can be prepared in various methods. Several well developed methods include dynamic synthesis using detonation, high pressure and high pressure (HPHT) synthesis, milling of HPHT diamond, laser ablation and chemical vapor deposition (CVD) [16]. 0D diamond is a special type of diamond. The reduction of size enables 0D diamond to have a relative larger surface area and very different surface properties compared to the bulk counterpart. Moreover, the surface of 0D diamond is often tunable in terms of the chemical, electrical and biomedical

properties [17]. Thus by tuning the surface properties of nanodiamond, it can be applied to various scenarios such as bioimaging, biosensing and drug delivery.

Moreover, with the reduction of the particle size, it is possible to achieve just a few or even only one color center such as nitrogen vacancy (NV) or silicon vacancy (SiV) in a single nanodiamond. Due to the stable photon emission of color centers of diamond, nanodiamond is an ideal candidate of single photon source. For example, with the reduction of the size of the nanodiamond below 2 nm, one single diamond particle can be made with only a few hundred carbon atoms and a few or only single SiV color center, making it appropriate for fluorescent labelling in cell biology, quantum communication and quantum photonics [17-18]. Similarly, absolute single-photon source can be realized through the preparation of nanodiamond with a single NV center and it can be calibrated with respect to its photon flux and its spectral photon rate density [19]. The high emission purity indicates the great potential of nanodiamond as a stand photon source in the low photon flux regime.

Reactive-ion etching (RIE) is an effective way to fabricate diamond nanowires (DNWs) **(Figure 1a)**. To realize this, hard masks are required in most cases. The masks can be made from metal (e.g., Al micromasks [20]) or inorganic compounds (e.g., hydrogen silsesquioxane, HSQ [21]). In some other cases, the etching was conducted either without masks [22] or with self-masking [23]. Etching without masking is relatively simple since the removal of masks is not needed. Note here that self-masking means that the boron dopant atoms act as the mask. The density of the resultant nanowires is thus dependent on the boron doping level **(Figure 1b, 1c)**. The etching of a heavily boron-doped diamond film results in very dense DNWs, while that of a lightly boron-doped diamond (BDD) film leads to sparsely formed nanostructures (e.g., nanotextures) [23].

The DNWs have been formed from gathering diamond nanoparticles on the surface of nanowires (e.g., Si nanowires [2, 24], carbon nanotubes [25]) **(Figure 1a, 1d, 1e)**. The surface areas of these BDD nanowires were effectively promoted, which were several times bigger compared to that of a conventional planar BDD electrode. It has been reported that these diamond nanostructures increased transport during the electrochemical oxidation process, exhibiting much lower energy consumption in the phenol oxidation process [24]. In another study, it was revealed that the 1D Si nanowires that were prepared in metal-assisted etching were O-terminated and thus super-hydrophilic. They were not good for anti-fouling, either. Interestingly, the coating of

Si nanowires with a diamond layer not only changed the surface wettability of Si nanowires from super-hydrophilic to super-hydrophobic, but also offered more strength to improve the anti-fouling performance. For example, on these DNWs, the water contact angle increased from 41° to 150.7° and the amount of chlorella attached was decreased by 12.9 folds [2a].

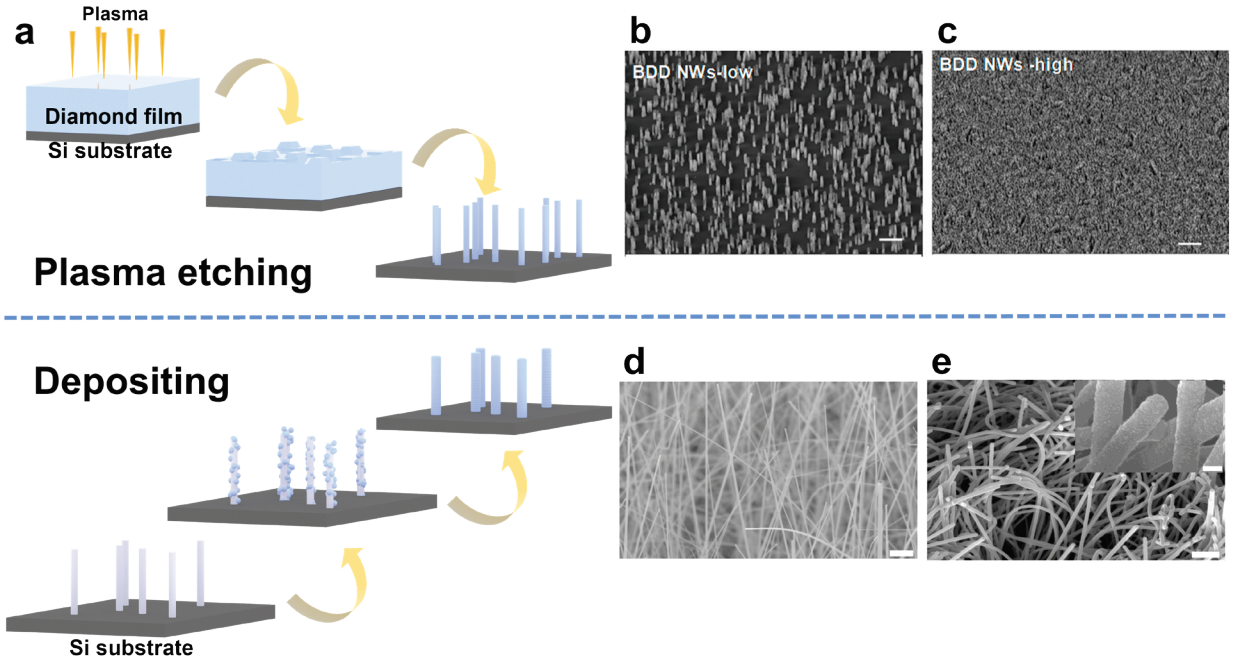

Figure 1. (a) schematic of two kinds of tactics to synthesize DNWs; (b-c) SEM images of BDD NWs in low (b) and high (c) density [23]; Reproduced under terms of the CC-BY license.[23] Copyright 2017, the Authors, published by American Chemical Society. (d-e) SEM images of Si (d) nanowires and DNWs (e) depositing on Si substrate [2b]; Reproduced with permission.[2b] Copyright 2017, Elsevier Ltd.

It has been also confirmed that the hydrogen termination of a diamond film contributes to its electronic properties [26] and vibrational modes [26b], in addition to the change of water wettability and anti-fouling properties of a diamond film. In this context, the electronic properties of DNWs with different shapes and surface terminations have been investigated under external electric fields by means of density functional theory (DFT) calculations together with the effective screening medium (ESM) method. The geometries and electronic properties of DNWs are known to be strongly dependent on their structures and surface hydrogenation. The hydrogenated DNWs were found to retain their initial cross-sectional shape. Triangular and hexagonal DNWs are known as semiconductors with direct band gaps at the Γ point of 3.26 and 3.67 eV, respectively. In contrast, the DNWs with clean surfaces act as metals, irrespective of the shape of the DNW

cross-section [26a]. Electronic inspection showed that the hydrogen atoms on the surface have the main contribution to the conduction bands of hydrogen-passivated DNWs. The vibrational modes for the ultrathin DNWs were then classified into two regions and revealed the size-dependent trend. Surprisingly, they showed opposite behaviors: blue-shift in low frequencies (namely confined modes) and red-shift in high frequencies which were mostly influenced by the surface termination effect [26b].

The thermal diffusivity of DNWs has been found to be lower than that of bulk diamond [27]. The comparative analysis by means of the force-/energy-based approaches has revealed the atomistic basis behind the diameter-dependent elastic properties of the nanowires. The DNWs have higher stiffness with a decreased diameter, whereas the energy-based method showed that the DNWs became softer with a decreased diameter [28]. In the case of a period length of ~25 Å, the thermal conductivities of DNWs were linearly increased with an increase in the period number. With a period length of ~103 Å, both the coherent phonons dominated heat conduction and thermal conductivities of the DNWs were length-dependent [29].

Several detectors with BDD ultra-nanocrystalline diamond nanowires (B-UNCD NWs) [21a, 22, 30] have been fabricated. In these works, the B-UNCD NW fabrication procedures involved diamond nanoparticle seeding, hydrogen silsesquioxane (HSQ) masking, electron beam lithography (EBL) patterning, and reactive ion etching (RIE) steps. Due to the ultra-nano size nature and the nanospherical structure, the as-prepared UNCD NWs often have properties similar with the nanoparticles of the 0D diamond. The B-UNCD NWs with oxygen functional groups possessed an intrinsic nature and were capable of adsorbing carbon monoxide (CO) [21a, 22]. The as-formed self-powered ultraviolet photodetectors exhibited an ultrahigh photoresponsivity of 388 A W^{-1} using the 300 nm wavelength light. Such performance was enhanced when Pt nanoparticles were loaded [30a]. The estimated responsivity of the zero-biased UV photodetectors using nitrogen-incorporated UNCD NWs was 2.0 A W^{-1} when a 350 nm light source was applied [30b].

2.2. Diamond nanoneedles

High-surface-area diamond nanoneedles can be produced through overgrowing vertically aligned Si nanowires (as scaffolds) with thin diamond layers. Such a Si nanowire is so-called as “black silicon”, produced through simple plasma etching. In this regard, the whole high-aspect-

ratio nano-protrusions was named as “black Diamond” **(Figure 2a)**. Such long, dense black diamond nanoneedles with sharp tips own robust mechanical bactericidal surfaces, killing bacteria based on stretching and disruption of the cell membrane **(Figure 2b, 2c, 2d)** in line with the hydrophobicity of the surface [31].

Pyramidal single crystal [100] facet diamond nanoneedles **(Figure 2e)** were collected by use of a mature two-step way. This method combined the CVD growth of a thick polycrystalline diamond film and subsequently thermal oxidation of such a diamond film in air to selective volatilization of a small fraction of diamond crystalline and disordered carbon material. The mechanism of forming these pyramidal diamond nanoneedles has been concluded as follows. In the initial step, octahedral tops formed on the surface of the diamond film as the [111] facet had a higher deposition rate. As the deposition continued, the condensation rate of [100] gradually caught up and the growth rates of [111] and [100] facets almost reached the same, although the etching rate to the [111] facet is higher than that to the [100] facet under preferable H etching plasma. Eventually, the [111] facet is separated into small fragments. They cannot grow to big crystals because of the continuous secondary nucleation or mass nucleation sites, and are shielded by neighboring overgrowing ones. Meanwhile, the initial columnar-grain texture [100] facets always remain relatively unaltered. Finally, the pyramidal diamond nanoneedles with single crystal [100] facet is retained while disordered carbon disappears during severe etching or selective air oxidation [32]. A proper etching time and etching temperature have to be carefully selected to avoid the damage of diamond nanoneedles. For example, an increase of the CVD deposition time and the tetramethylsilane (TMS) gas flow rate improved the fractions of the diamond [100] facet [32b]. Note that the formation of pyramidal diamond nanoneedles on single crystal [100] facet is relatively common, even with rectangular base planes and an apex tip [32-33].

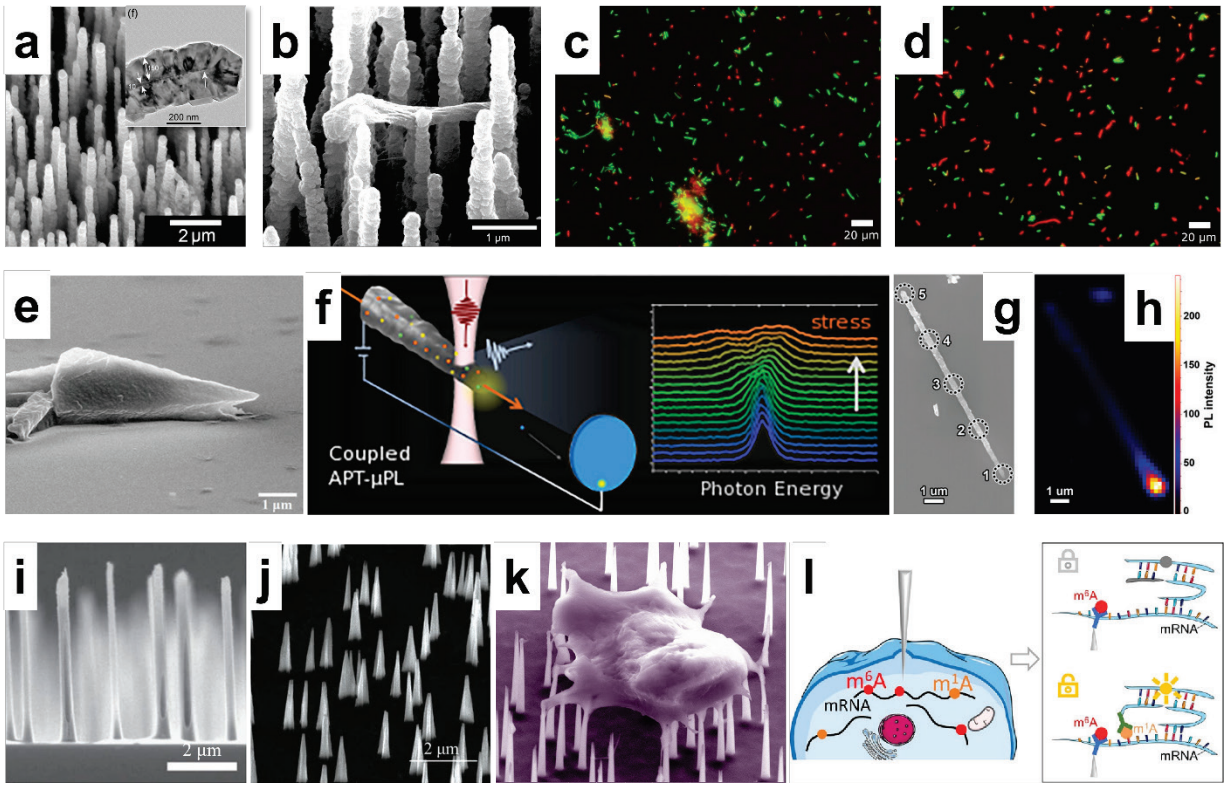

Figure 2. (a-d) (a) SEM image of "black diamond" nanoneedles, the inset shows a core-shell structure, where the diamond film thickness is ~150 nm and the Si needle core is ~10 nm [31a]; Reproduced with permission.[31a] Copyright 2018, Royal Society of Chemistry. (b) SEM image of Escherichia coli on the H-terminated "black-diamond" nanoneedle surface, which appeared deformed and flaccid; (c-d) fluorescence micrographs showing the reduction in cell aggregates from flat diamond thin film (c) to "black diamond" film surface (d) [31b]; Reproduced under terms of the CC-BY license.[31b] Copyright 2019, the Authors, published by Springer Nature. (e) SEM image of a pyramid-like diamond microneedle [33e]; Reproduced with permission.[33e] Copyright 2022, John Wiley and Sons. (f) schematic of contactless piezo-spectroscopy by the high electrostatic field at the apex of monocrystalline diamond nanoneedles, and energy splitting of the photoluminescence lines of NV centers [33a]; Reproduced under terms of the CC-BY license.[33a] Copyright 2017, the Authors, published by American Chemical Society. (g) SEM image and (h) the photoluminescence mapping image of a single diamond nanoneedle, the SiV photoluminescence intensity exhibited a maximum near the apex [32b]; Reproduced with permission.[32b] Copyright 2021, John Wiley and Sons. (i-j) SEM images of cylindrical (i) [34] and conical (j) diamond nanoneedles [35]; Reproduced with permission.[34] Copyright 2014, Springer Nature. Reproduced with permission.[35] Copyright 2016, John Wiley and Sons. (k) SEM image of protrusion of nanoneedles into intracellular [36]; Reproduced with permission.[36] Copyright 2020, American Chemical Society. (l) diagram using an array of diamond nanoneedles to isolate methylated mRNA in living cells based on the "Molecular Fishing" strategy [37]. Reproduced with permission.[37] Copyright 2022, American Chemical Society.

Diamond nanoneedles own the rectangular pyramidal-shape and nanometric apexes. Thanks to the inherent properties of diamond, this kind of diamond nanoneedles were then applied as

optical sensors of intense electrostatic fields in scanning probe microscopes [33a], high efficient sources of photoemitted electrons [33c], stable point electron sources [33d], quantum information processing, and optical sensing equipped with color centers [32b, 33b, 33e]. Their pyramidal shape makes diamond nanoneedles different from planar diamond films in many aspects. For example, the contactless assessment of the stress was built up inside a field emitter based on diamond nanoneedles. Energy splitting of photoluminescence lines of nitrogen-vacancies (NVs) inside diamond nanoneedles was observed **(Figure 2f)**, due to electrostatic stress as a consequence of the interaction between the free holes accumulated at the needle apex. The electrostatic stress reached 7 GPa at the apex of diamond nanoneedles. It rapidly evolved into uniaxial tensile stress along the needle shank and further varied as a function of distance from the apex, exhibiting an innovative way to detect mechanical properties with the contactless piezo-spectroscopy of nanoscale systems [33a]. When diamond nanoneedles with silicon-vacancy centers (SiVs) are taken as an example, one major challenge for quantum optics applications — the localization of the color centers — has been settled **(Figure 2g, 2h)**. The proof of optical characterization results indicated that SiVs were predominantly concentrated at the crystallite apexes. This is because, the only possible source of silicon is from the silicon substrate, and the incorporation of Si atoms only happens on the bottom diamond lattice during the nucleation process [32b, 33b, 33e]. On the other hand, an external silicon source can be added during the CVD process to improve the whole density of SiVs. During this process, the formation of the [100] facet was promoted by the addition of tetramethylsilane (TMS) gas percussor, eventually leading to the increased yields of diamond needles that contain SiVs as well as enhanced photoluminescence efficiency [32b].

The pyramid-like diamond microneedles with high contents of SiVs were reported to be suitable for quantum bioimaging and intracellular thermometry [33e]. If the size of the apexes are too large, complete and accurate monitoring inside the living systems would become impossible and the possibility of killing cells would become high. Diamond nanoneedles of the cylindrical shape with a vertical wall were also obtained through a RIE step **(Figure 2i, 2j)**. They performed better than the pyramid-like needles. The vertical sidewall of the cylindrical nanoneedles makes them more suitable for rapid penetration of a cell membrane. This is because the force required for the penetration is significantly smaller than that of the pyramid needle and therefore the damage to the cells is less. The process is in a reversible and minimally invasive format [35-38]. By use of these diamond nanoneedles, drugs, and biomaterials can be delivered into cytosol within

several minutes. In these studies, double-stranded DNA has not been broken and the cell membranes were fully recovered within 40 min [35]. A serious report of intracellular biopsy has been published by applying an array of cylindrical diamond nanoneedles **(Figure 2k)** [37-38]. They compared these needles with "fishing rods" that were functionalized with RNA-binding proteins as the "fishing bait" to directly and quickly pull RNA out of the cytoplasm while keeping cells alive. Directly isolation of targeted RNAs from the cytosol of a large population of cells was performed to achieve quasi-single-cell RNA analysis. Each nanoneedle worked as a separated reaction plant for parallel *in situ* amplification, visualization, and quantification of RNAs to achieve quantitative evaluation [37-38]. Based on this highly reliable and robust method, the dynamic evolution of cellular heterogeneity [38a], relative spatial dynamics of the cellular miRNAs in associated cell populations [38b], and dynamics of mRNA methylation in mammalian cells under physical or chemical stimuli have been revealed **(Figure 2l)** [37].

Diamond has very strong covalent bond which resists to deform and slip under normal pressure. Therefore it is a challenge to determine the mechanical properties of diamond experimentally, especially for the diamond of bulk size. Alternatively, theoretical work has been employed to study the strength and the deformation mechanism of diamond. It is well known that cleavage prefers to take place along the {111} plane. The reason can be attributed to the less bond density as well as the less fracture energy (for nanotwinned diamond, the fracture energy is much higher). According to Born and Huang's theory, the structure of diamond would become unstable, and failure would take place when elastic modulus reaches zero, which corresponds to the upper limit of C-C bond length [39]. Telling et al calculated the theoretical strength and cleavage of diamond using first principles calculations and found that the theoretical strength of diamond was dependent on crystallographic direction, e.g., [100], [101] and [111] directions [40]. They found that the [100] direction has the highest theoretical tensile strength (225 GPa), followed by [110] (130 GPa) and [111] (90 GPa) directions. Almost same simulation result was obtained by Zhang et al in a follow-up research [41]. They also found that during tensile straining, the dominant structure deformation was the elongation of the [111] bonds while the bond length variation in the {111} planes was very little. In a more recent work, researchers found that when ideal strengths were reached along [100] and [111], a strength of ~ 100 GPa would project to [111], which also explained that all fractures initiate from the {111} plane. First principles calculation was also employed to predict the ideal compressive strength of single crystal

diamond, with –223.1, –469.0, and –470.4 GPa obtained along [100], [110] and [111] directions, respectively [42].

The successful preparation of diamond nanoneedles has also contributed to the determination of the mechanical properties of diamond. A so-called "fishing process" has been mentioned to examine the mechanical properties of diamond needles, i.e., the ultra-elasticity at nanoscales to sustain the deformation without fracture during a puncture operation [38b]. In stark contrast to these established benchmarks of diamond (e.g., quintessential super-hard, high brittleness), ultra-large and fully reversible elastic deformation in nanoscale needles of both single-crystalline and polycrystalline diamond has been demonstrated [43]. This stems from the well-known size effect, i.e., "smaller is stronger" [44], that is, with the reduction of the material size down to macro- and nano-size, the probability of the appearance of defects (e.g., dislocation, crystal twinning and vacancy) is reduced, allowing the mechanical properties of the material closer to the theoretical levels [44-45]. As confirmed from the *in-situ* nanomechanical bending experiments on diamond nanoneedles inside a SEM nanoindenter system, the downward motion of the indenter tip was found to be generated in a sideward displacement from the inclined tip surface, thereby bending the nanoneedles after the contact. Instantaneous and full recovery of a nanoneedle to its original and undeformed shape happened when the nanoindenter tip was retracted before the onset of catastrophic fracture.

The mean maximum tensile strains and peak maximum tensile strain of the [111] oriented single crystalline were up to 6% and 9%, respectively **(**calculated by FEM simulation, as shown in **Figure 3a, 3b)**. They approached closely to the theoretical elastic limits. The corresponding maximum tensile stress reached ~89 to 98 GPa. The elastic strain of polycrystalline diamond nanoneedles was lower, approximately one-half the average of a single crystalline diamond. But overall, both elastic limits of single and polycrystalline diamond nanoneedles were higher than their bulk counterparts. The concurrent high strength and large elastic strain were ascribed to the paucity of defects in the small-volume diamond nanoneedles and to the relatively smooth surfaces compared with those of microscale and larger specimens, respectively. To further refine this epoch-making discovery, the relationship between the tensile strain, strength of diamond nanoneedles and factors of diameter, orientation and surface state have been further identified and reported [46]. The state-of-the-art nanomechanical bending experiments were conducted *in situ* inside a transmission electron microscope (TEM). The maximum achievable elastic strain of

diamond nanoneedles was clearly dependent on the size and orientation of diamond nanoneedles. For example, the diameters of diamond nanoneedles of 60, 95, 115, and 150 nm gave the achievable maximum elastic tensile strains of 13.4, 9.1, 11.1, and 6.5%, respectively. The corresponding maximum local tensile stresses were 125, 88, 105, and 65 GPa, respectively, as supplied by the thinnest one. The [100] oriented nanoneedles consistently exhibited higher fracture tensile strains than those of [110] and [111] nanoneedles at the same diameters. A maximum local tensile strain of 13.4 % was reported **(Figure 3c, 3d)**, which was stated to be the largest that has ever been experimentally achieved. Later more detailed data was provided after nanotwinned diamond (in section 3.3) was synthesized and applied as the TEM nanoindenter [47]. The maximum tensile strains of the bending nanoneedles were estimated to be as high as 8.6%, 5.2%, and 11.2% for [111], [110], and [100] oriented diamond nanoneedles, respectively. What's more, it was found that fracture was dominated by cleavage of atomic-flat [111] facets, regardless the original phase. For tension along the [111] direction, the C–C bonds perpendicular to the (111) plane had the largest bond length and the least electron density in between two neighboring C atoms. Therefore, this group of C–C bonds was the most weakened and prone to breakage. The trend was the same for the case of the [110] and [111] tension.

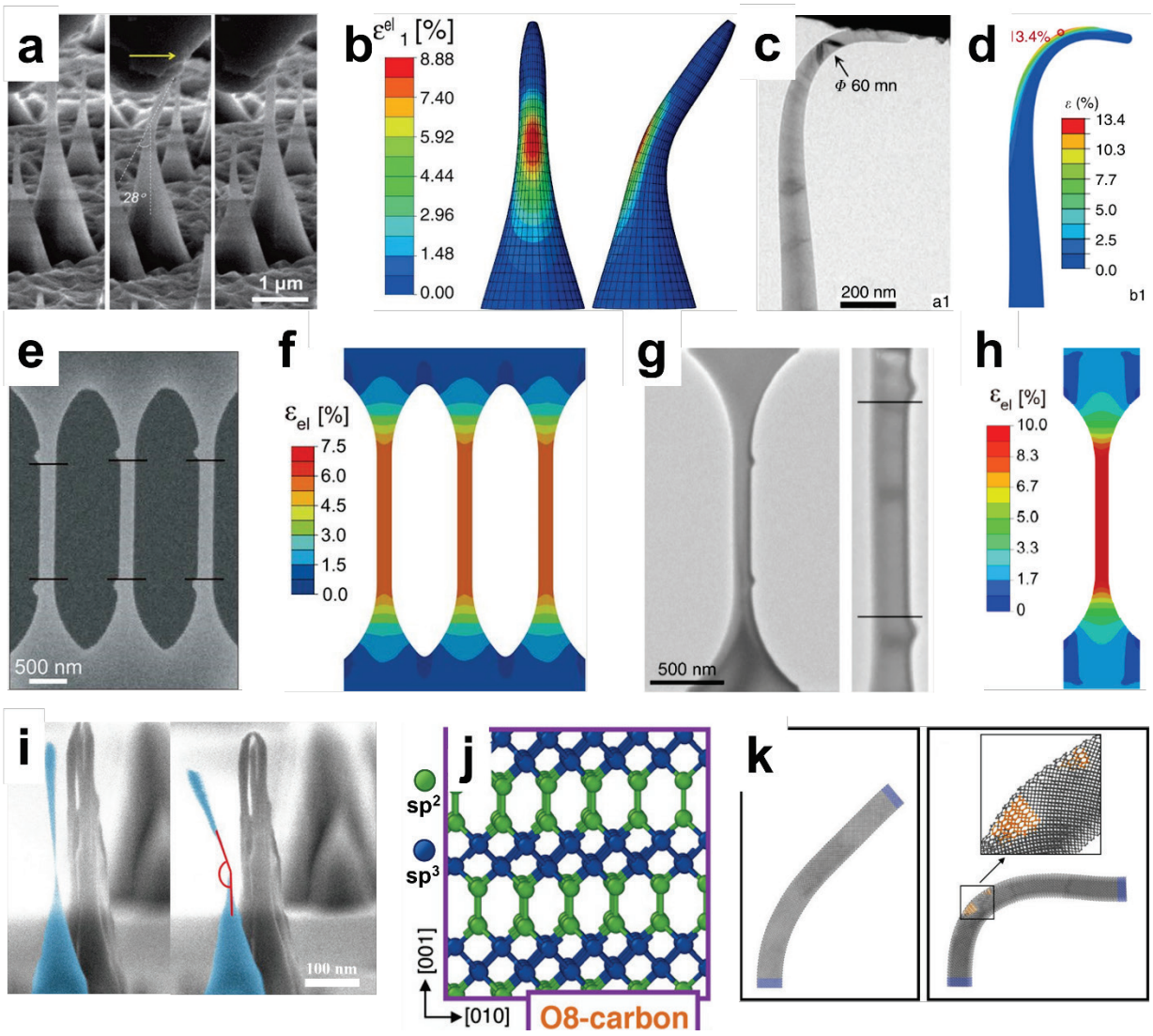

Figure 3. (a) SEM images from a reversible run by lateral pushing of the nanoneedle; (b) FEM simulation of the bending process, reproducing the shape of the bending and showing the local elastic maximum principal strain distribution for the nanoneedles [48]; Reproduced with permission.[48] Copyright 2018, the American Association for the Advancement of Science. (c) snapshot and (d) FEM simulation of the maximum deformation of a single [100] nanoneedle at a diameter of 60 nm [49]; Reproduced under terms of the CC-BY license.[49] Copyright 2019, the Authors, published by Springer Nature. (e) SEM image of loading-unloading process of a three-bridge array; (f) FEM simulation reproducing the critical geometry of the three-bridge array, showing highly uniform elastic strain distribution (~5.8%) along the tensile direction; (g) TEM image showing the optimized sample geometry; (h) FEM simulation reproducing the critical geometry of the diamond bridge sample and showing the elastic strain distribution along the longitudinal direction [50]; Reproduced with permission.[50] Copyright 2021, the American Association for the Advancement of Science. (i) SEM image of a diamond nanopillar before deformation and after bending induced by an electrostatic force with deflection of 25°; (j) schematic of the new O8-carbon phase with sp^2 and sp^3 hybridization; (k) molecular dynamics simulations of bending of a (001)-oriented diamond nanopillar under plastic deformation with

the appearance of O8-carbon (orange atoms) [51]. Reproduced with permission.[51] Copyright 2021, John Wiley and Sons.

It should be noted that the above two attempts of straining the diamond were limited by the strain being within a small volume by flexural bending, during which nonuniform strain distribution occurred. Although ultra-high elastic deformation was observed from the in-situ experiment, the deformation scale value was only estimated through FEM simulations. Therefore, the selection of the simulation methods and parameters played an important role. During nanoindentation process, the friction between the nanoindenter and diamond nanoneedle of the low-pressure environment must be taken into consideration [43]. Moreover, in the previous DFT work regarding the calculation of the theoretical strength diamond, thermal fluctuation effect was not taken into account. Besides the experimental work of ultralarge elastic deformation of diamond nanoneedle, Banerjee et al also conducted a DFT-MD simulation work which included the temperature effect to predict the tensile limit of <111> direction diamond, with a result of 13% obtained.

Compared with the nanoneedles, the microbridge structure of the diamond allowed more uniform deformation and a better observation under tensile loading [52]. These microbridges were precisely microfabricated during the focused ion beam (FIB)-assist processes. The length of the microbridge structures was about 1 μm and the width was 100 nm **(Figure 3e)**. The uniaxial tensile tests were conducted on such smooth diamond specimens by use of a nanoindenter with a customized tensile diamond gripper. Ultra-large uniform elastic strains (6% – 8%) were achieved in microfabricated diamonds that were orientated in the [100], [101], and [111] directions **(Figure 3f)**. Large uniform elastic deformation was proximately 7.5% through the entire gauge area of the bridge during quantitative tensile testing **(Figure 3g, 3h)**, rather than deforming in a limited region during bending. Up to 9.7% uniform tensile strain was realized by refining the sample shape by adopting the American Society for Testing and Materials (ASTM) standard for brittle tensile specimens. Such a high strain approached the diamond's theoretical elastic limit. In addition, *in situ* straining of the microfabricated diamond array that contained multiple bridges was realized. The large, uniform, and reversible straining among the multiple diamond bridges was believed to demonstrate the potential applications of strain engineering for diamond-based electronics.

The elastic deformation ability of diamond nanoneedles was revealed, and an unprecedented

form of plastic deformation has also been discovered [51]. Different from the fracture or restoration to its original statues in elastic deformation, plastic bending was permanent. The plastic deformation of diamond involves the formation of dislocation core and propagation driven by the compressive or shearing strain [53]. An experiment was carried out based on a contact-free electrostatic deformation technique **(Figure 3i)**. The electron beam of SEM was used to locally charge diamond nanoneedles and surroundings, giving rise to localized charge accumulation. Bending or deflecting happened when generating Coulomb forces were sufficiently strong and no physical contact was needed. An important factor was that the diameter ought to be small enough, in which the Gibbs Free energy was lower to induce ductile deformation. The authors believed that an orthorhombic unit cell with 8 atoms (named as O8-carbon) **(Figure 3j)** played an important role in continuous mechanical deformation. The O8-carbon appeared under a phase transition of diamond sp^3 carbon, which was spontaneously under strain at the edge of thin (001)-oriented diamond nanoneedles **(Figure 3k)**. The discovery of the elastic properties of diamond nanoneedles can offer the potential for new applications through optimized design of diamond nanostructure, geometry, elastic strains, and physical properties. Diamond nanostructures with uniform tensile elasticity can offer immense applications of deep elastic strain engineering for photonics, electronics and quantum information technology.

2.3. Diamond nanocones, nanopillars/nanorods

Diamond nanocone (or nanopillar, nanorod) is one of the most common diamond nanostructures. It is normally prepared through the RIE of a thick diamond film. Up to now, diamond nanocones have been successfully applied in the fields of clinical sterilization [54] as well as the construction of plasma illumination devices [55], field emission [56], and electrochemical sensors [57]. In some diamond nanopillars, only half of them were collected for photons that were guided to two directions parallel to two symmetric axes of pillars. To overcome such a drawback, mass arrays of diamond were inverted nanocones after the precise dry etching of a commercial thick diamond film inside an ingenious cone-shaped Faraday cage **(Figure 4a, 4b, 4c)**. Compared with photons obtained using diamond nanopillars, such arrays offered much improved optical properties, long spin coherence time, and scalability of the single photon sources [58].

Meanwhile, diamond nanocones have been applied for different electrochemical applications.

For example, boron-doped diamond nanocones have been employed as an electrocatalyst for the nitrogen reduction reaction **(Figure 4d, 4e, 4f)** [59]. The NH_3 yield rate was as high as 19.1 $\mu g\ h^{-1}\ cm^{-1}$ and the Faradaic efficiency was as high as 21.2%. These values were among the best of the metal-free electrocatalysts. Moreover, such a system was stably operated for at least 8 days under ambient conditions. Diamond nanocone arrays, which were produced by means of RIE, owned two different negative substrate bases and showcased better performance. In more detail, their tip architecture further enhanced the catalytic activity. The surface charges on the nanotips decreased the reaction free energy for the rate-determining step (RDS) on the diamond [111] and [110] facets, facilitating a fast nitrogen reduction reaction process [59].

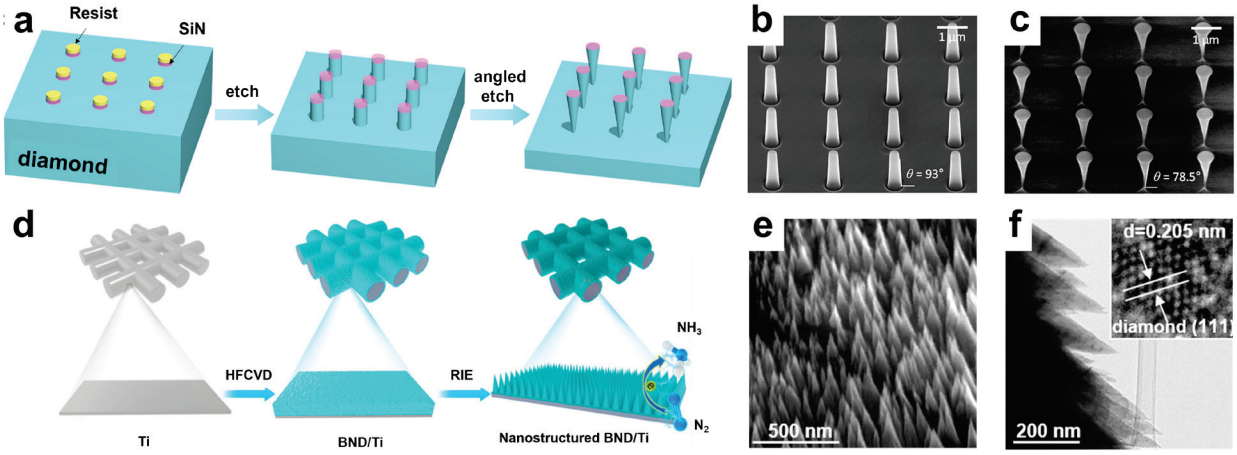

Figure 4. (a-c) (a) schematic of the synthesis of diamond nanorods and diamond inverted nanocones; SEM image of diamond nanorods (b) and diamond inverted nanocones (c) [58]; Reproduced under terms of the CC-BY license.[58] Copyright 2020, the Authors, published by American Chemical Society. (d-f) (d) schematic of the synthesis of diamond nanocones on Ti meshes; high-magnification SEM image (e) and TEM image (f) of it, the inset was HRTEM image [59]; Reproduced under terms of the CC-BY license.[59] Copyright 2020, the Authors, published by American Chemical Society.

Diamond nanorods/nanopillars have also been fabricated from the CVD overgrowth of 1D substrates/templates [60] that were produced by RIE (e.g., using O_2 plasma [61]) processes. For example, plenty of undoped and nitrogen-doped diamond nanorods (DNRs) have been synthesized. These nitrogen-doped DNRs showed high electrochemical activity, such as for simultaneous detection of Pb^{2+} and Cd^{2+} ions [61f], and for enhanced field electron emission with high densities of local electron emission sites with nitrogen impurities [61e].

2.4. Diamond nanothreads

Diamond nanothreads which were reported in 2015 for the first time, are one of the freshest 1D diamond-related materials [14c]. Much different from the well-studied 1D diamond nanostructures (e.g., nanowires, nanocones, nanoneedles), the studies on these newly born diamond nanothreads are on the initial period, although they possess lots of potential. For example, their mechanical properties are remarkably comparable to graphene and carbon nanotubes [62]; their deformability is extended from brittle to ductile [62b, 63]; their load transference to polymer is high, due to more irregular surface topography [14a, 64]; their mass sensitivity and quality factor are ultrahigh [65]; their electronic properties are tunable by tensile strain [66]. Therefore, the discovery of diamond nanothreads is a breakthrough in compression inducing phase conversion. It is expected to prolong the diamond-related materials community.

The idea to synthesize diamond nanothreads originates from pressure-induced polymerization (PIP) of aromatic molecules to construct the sp^3-hybrid carbon frameworks [67]. For many years, only polymers and extended amorphous products were synthesized with small volumes. Until 2015, the long, narrow, curved, crystallized diamond nanothread was proved to be possible to be synthesized as the first ordered product [14c]. Experimentally, benzene samples were compressed to 20 GPa at room temperature in an equipped diamond anvil, maintained for 1 h, and then recovered to ambient pressure at a low decompression rate. The finally gathered solid product was white. This newly synthesized material did not dissolve in light hydrocarbon organic solvents. It began to pyrolyze rather than melting in the air at 250 ℃, indicating that it was not composed primarily of small molecules. It exhibited a long-range parallel striation space of 6.4 Å and extended to tens of nanometers in its TEM imaging **(Figure 5a)**. The Bragg peaks in its total XPS spectrum indexed to a 2D hexagonal lattice **(Figure 5b)**. The layer lines observed in electron diffraction patterns of annealed bundle samples indicated it was ordered along their length [68]. These characterization results revealed that diamond nanothreads are in ordered. In addition, the sp^3-bonding inside diamond nanothreads is definitely the dominant carbon bonds. It was based on the nearest-neighbor C-C bonds with a distance of 1.52 Å. The coordination numbers are extracted from the neutron. Namely, every carbon has one hydrogen and three carbon neighbours **(Figure 5c)** [14c, 69]. Comprehensively, this new product is 1D strand of sp^3 carbon and its outer surface is terminated in hydrogen. It is about as wide as the progenitor

benzene molecules and processes a hexagonal lattice. The choice of the name of nanothread is because the nanothreads disqualified the definition of traditional polymers, nanowires, and nanotubes. They have multiple covalent bonds across the cross-section. However, they have no central hollow or local planarity structures. The first-principles modeling also strongly supported such nanothreads. The name of "diamond nanothreads" came from the local diamond-like tetrahedral motif structure [14c].

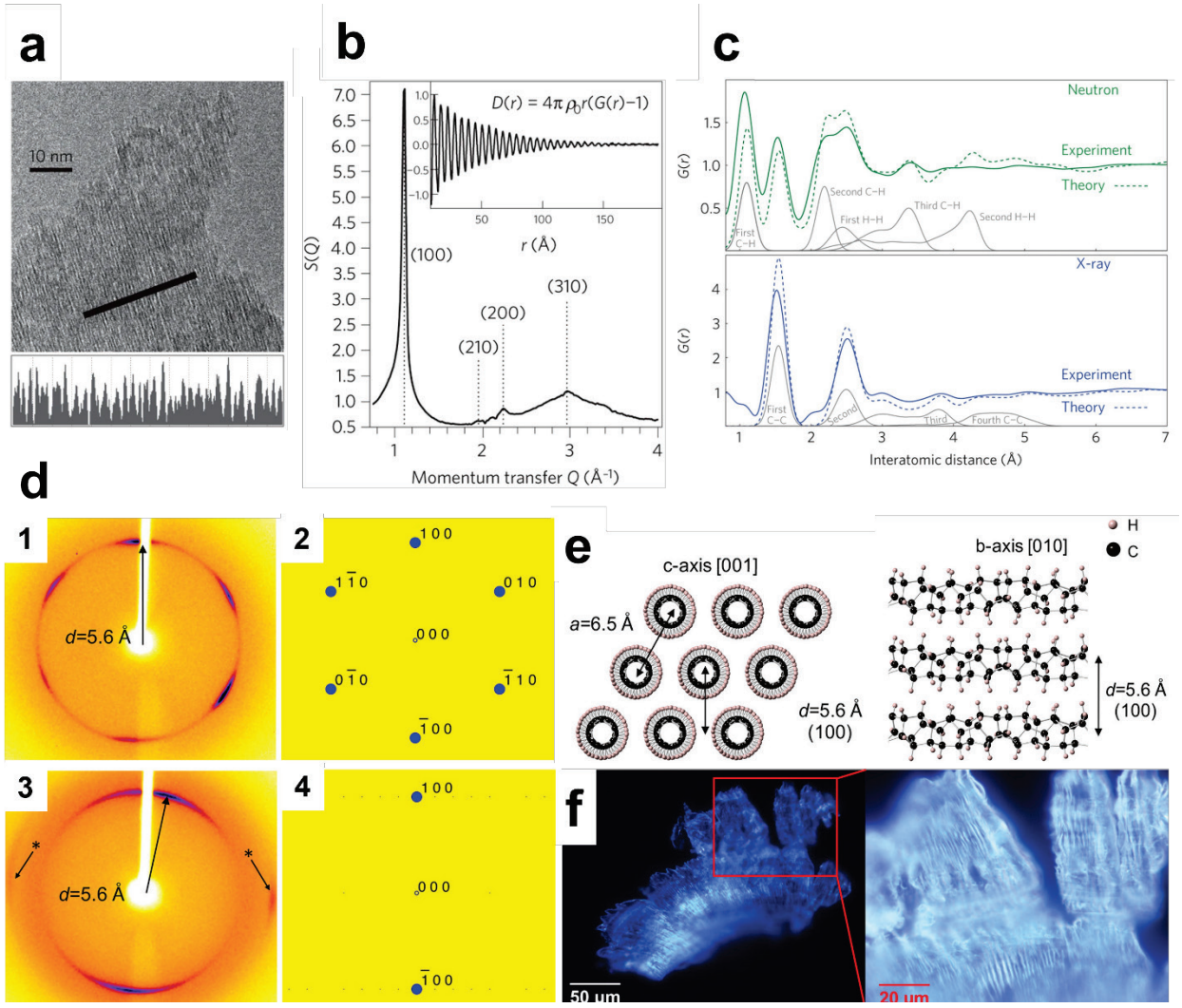

Figure 5. the first synthesis of diamond nanothread: (a) bright-field TEM image showing striations spaced 6.4 Å apart extending for tens of nanometers; (b) X-ray scattering with Bragg peaks, inset is the width of the prominent (100) peak; (c) both X-ray and neutron data [14c]; Reproduced with permission. [14c] Copyright 2014, Springer Nature. diamond nanothread single crystalline: (d) X-ray diffractions showing a hexagonal pattern (d1) and after rotation (d3), counterpart predicted ones (d2 and d4); (e) images of 1D parallel combinational macroscopic striations; (f) diffraction patterns of predicted packing nanothread crystal from top view down *c*-axis (left) and side view along *b*-axis (right) [70]. Reproduced with permission.[70] Copyright 2017,

American Chemistry Society.

In 2017, the preparation of diamond nanothread single crystals was reported [70]. The biggest difference with the firstly synthesized diamond nanothread is that, this time the compression rate was slower. The polycrystalline mixtures of benzene phases were compressed to 23 GPa at room temperature. In a two-consecutive compression program, the rates were 2-3 and 0.6-1.2 GPa h^{-1}, respectively. The uniaxial stress was then released to ambient pressure at the same rates within the same pressure ranges as for the compression process. The X-ray beam diffraction patterns of 6-fold arcs **(Figure 5d)** agreed with the predicted values. In more detail, the hexagonal unit cell that was obtained from benzene powder owned a *c*-axis zone [001] of a representative array of nanothreads with a 6.5-Å-lattice constant and an interval of 5.6 Å **(Figure 5e)**. These nanothread crystals can be mechanically exfoliated into fibers. This is consistent with an ordered packing of aligned and stiff threads that are bound by van der Waals forces. The macroscopic single crystal was assembled into close-packed crystals over hundreds of microns long **(Figure 5f)**.

The possible reasons for such a successful synthesis have been further discussed. It was believed that spontaneous self-assembly of benzene monomers into single crystal packing was guided by uniaxial stress rather than topochemical reaction, based on mechanochemical compression. This is because dramatic geometric changes will happen as the van der Waals separations between benzene are replaced by shorter, kinetically stable covalent C-C bonds. This shrink breaks up the crystal order, leading to amorphous products as the result of the constraint of topochemical reactions [69-70]. Moreover, the slow decompression rate of 2 GPa h^{-1} can act as the crux [14c]. The derivation of the synthesis pathway was assumed to be a long benzene polymer that emerged from a series of [4π+2π] cycloaddition reactions. This polymer is not fully sp^3 hybridized nanothreads at this step and is thus called “degree-4” (4 sp^3 bonds and a single unsaturated C-C double bond per benzene ring). Once an intramolecular reaction happens, aligned olefin functions are oriented for a zipper cascade to give a fully sp^3 hybridized nanothreads. This product is called “degree-6” (6 sp^3 bonds per formula unit) **(Figure 6a)**. Both steps are promoted under high pressures, while the later evolution was believed to be aided by the slow decompression operation. A slow release of the pressure was thus the key to retaining a well-ordered stable sample [14c, 71]. Furthermore, slower compression is possible for the strong kinetic preference of the single lowest-barrier pathway that is implied by slow compression at

room temperature. This might facilitate the formation of well-ordered nanothread crystals by means of suppressing less favorable reactions (e.g., cross-linking the nascent threads) [70]. Note that in these reports many details of these diamond nanothreads have not been disclosed. For example, their precise atomic structures [14c, 68-69, 71-72] and their reaction pathways [73] are still not clear.

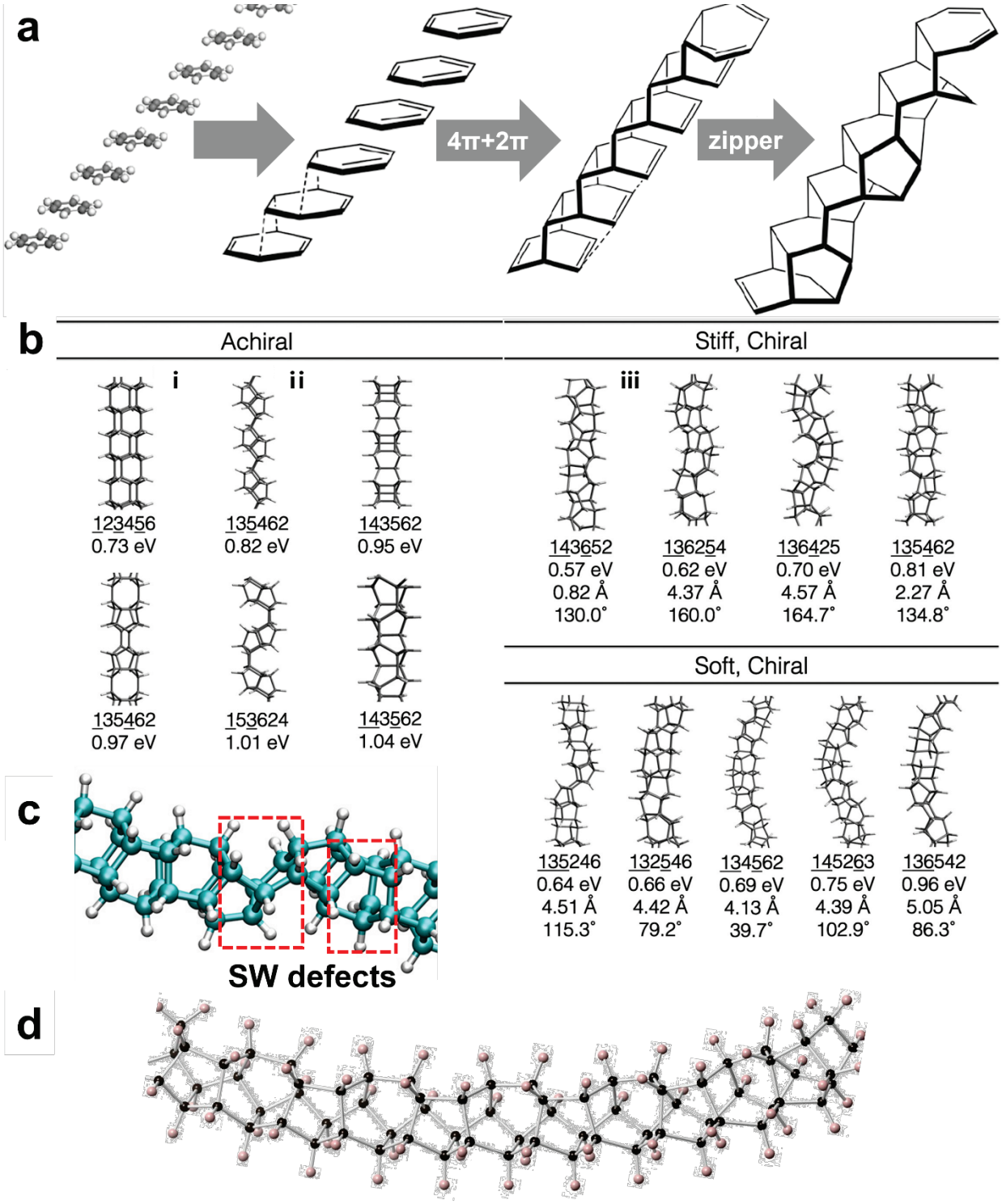

Figure 6. (a) reaction mechanism that forms a sp^3 diamond nanothread from benzene molecules, from left to right: an axis stacking extracted structure in the leftmost column, a series of [4π+2π] cycloaddition reactions to form a benzene polymer, and aligned olefin functions are then well oriented for a zipper cascade to give a fully sp^3 hybridized nanothread [14c]; Reproduced with

permission.[14c] Copyright 2014, Springer Nature. (b) atomic configurations of the unit cells of 15 kinds of energetically favorable diamond nanothreads, including Achiral, Stiff-chiral, Soft-chiral, and three previously reported nanothreads (i) sp^3 tube (3,0), (ii) polymer I, (iii) polytwistane [72]; Reproduced with permission.[72] Copyright 2015, American Chemistry Society. (c) simulation snapshot of nanothread model with two Stone−Wales defects [62a]; Reproduced with permission.[62a] Copyright 2015, American Chemistry Society. (d) ball-and-stick model of nanothread, it's curved in isolation [14c].

Considering that each ring has six covalent bonds to neighboring rings up and down the column, 50 kinds of possible nanothreads having different topological distances were enumerated according to Crespi's theoretical predictions [72]. Among them, 15 are within 80 meV per carbon atom **(Figure 6b)**, identified as energetically favorable. They were then divided into three classes: achiral, stiff-chiral, and soft-chiral. Many inferences about the properties of diamond nanothreads are then based on the three kinds of these fifteen structures. Obviously, the properties of different atomic structures are then varied. The most stable structure is the chiral one, revealed by the optimization of its aperiodic helicity. The stiff-chiral polytwistane is the lowest energy allotrope. In the literature, three nanothreads were already proposed: (3,0) sp^3 nanotube [74], polymer I [75], and polytwistane [76]. The (3,0) sp^3 nanotube and polymer I are the lowest energy achiral nanothreads **(Figure 6b)**. A random polymer intermediate was actually proposed in the structure between tube (3,0) and polymer I, as interrelated by two successive Stone-Wales (SW) transformations. It is a rotation by 90° of a carbon-carbon dimer **(Figure 6c)**, as an approximant to the nanothread **(Figure 6d)**. The calculated pair distribution functions well matched the experimental data, even better than either tube (3,0) or polymer I alone [14c]. Inside 15 kinds of enumerations, every benzene has been assumed to have hexavalent bonding geometries. According to the conjecture of synthesis pathways, the product should be totally consisted of sp^3 carbon. However, their analysis results by means of solid-state nuclear magnetic resonance (NMR) technique already confirmed about 20% sp^2 carbon. Later, more theoretical calculations revealed that semi-ordered diamond nanothreads are actually the combination of degree-4 and degree-6 with different degrees. The fraction of degree-6 is between 20% − 50% and that of degree-4 is about 30%, as confirmed by their NMR spectra [69, 71] and their electron energy-loss spectroscopy characterization [68]. Again, it must be highlighted here that precise atomic structures of diamond nanothreads have not been elucidated. In other words, what their atomic structure is and how degree-4/degree-6 is arranged have not yet been determined,

although the exitance and fractions of degree-4 and degree-6 carbon are ensured. The SW defect is an intrinsic component of diamond nanothreads. The *ab initio* calculations revealed that the energy of (3,0) sp^3 nanotube is decreased with an increase of the SW composition. The minimum formation energy arrives when the composition reaches 50%. However, the position and content of SW in the 15 structures are also still uncertain [66]. More studies are required to figure out the exact connection between benzene molecules.

Meanwhile, the formation mechanism of nanothreads is quite complicated. Take the (3,0) sp^3 nanotube, polymer I and polytwistane as examples, the elucidated polymerization ways of completely saturated nanothreads [73] demonstrated that eight topologically distinct degree-two polymers were found, where each with one or more conformers to form C−C bond rotations. The degree-2 polymer only emerges as an intermediate, due to its poor kinetic persistence. It transfers to a degree-4 polymer [69]. Some unstable conformers collapse without an energy barrier to the degree-4 polymers through the [4π+2π] cycloaddition, including 23 topologically distinct degree-4 polymers. Among them, only the degree-4 ones with double bonds in each ring approximately on the same side of the chain have the chance to proceed to the degree-6 nanothreads after zipping [73].

Since the organic solid-state benzene-to-nanothreads reaction is mostly controlled by its ability to overcome reaction barriers, rather than solely by thermodynamics, there are rich opportunities to tune or to impact synthetic outcomes [69]. Regardless of the employed precursors, controlling the slow rise and release of the applied pressure is expected to mainly induce polymerization of aromatics. Namely, it is crucial to successfully synthesize nanothreads. However, the reaction pressure is different according to the molecular structures of precursors. For example, benzene and pyridine are cyclic arrays, whose stability arises from large delocalization, intrinsic delocalized resonance energies of ~0.060 eV per π electron. The calculated activation barriers for nanothreads initiation in benzene and pyridine exceed 58 kcal mol^{-1}. Consequently, they are not typically vulnerable to addition reactions, likely necessitating higher pressures to break this array and induce reactivity in nanothreads-forming reactions [77]. The synthetic pressure of thiophene [78], especially compared with furan [77] or cubane [79], was even higher than that of benzene. This is because once the intrinsic electronic energy barrier of the thiophene reaction is higher at 1 atm, thiophene is more aromatic. Therefore, it is less susceptible to initial reactions where aromaticity is lost. Smaller volumes of activation than for furan were calculated for chain-

initiating thiophene [4π+2π] cycloadditions. The reduction of the enthalpic barrier by the pressure is then lower for thiophene polymerizations [78b]. As for the cubane-saturated, but immensely strained, cage-like molecule, it is a saturated one. Unlike aromatics, it exhibits extraordinary chemical stability under high pressures. Such molecules are therefore usually not considered as reactive precursors [79].

The choose of suitable precursors to replace benzene was proved to be an effective method to introduce functional groups into diamond nanothreads. For example, the reaction of pyridine under a slow compression at 23 GPa for 1 h and then a slow decompression to ambient over 8 - 10 h led to the formation of a well-ordered sp^3 carbon nitride nanothread product (with an empirical formula of C_5NH_5) [80]. It was reported that the product yield was greater than 30% when the pressure was around 14-18 GPa and the temperature was between 400 and 500 K [81]. In another report, nitride nanothread provided an alternative way of chemical substitution of nitrogen into extended carbon networks while keeping isoelectronic. It also exhibited photoluminescence, probably due to defects or sp^2 carbon functions along their length or bandgap emission. It is thus promising for specific biological imaging applications [80]. Furthermore, nitride nanothread was found to exhibit a higher tensile and bending stiffness with the presence of nitrogen atoms [82]. Similar to original diamond nanothreads, mechanical characteristics, especially tensile properties of nitride nanothread were pronouncedly varied, depending on distinct differences in the molecular morphology, atomic arrangement, and distribution of nitrogen atoms in the loading skeleton. One of them, named Polymer I_3-3_25 CNNT, showed similar intriguing transversion from brittle failure behavior to extraordinarily ductile behavior at a critical temperature of 15 K. It was thus believed as a lightweight material that can be used as robust energy-absorbed fibers in outer space and extreme experimental environments [83].

Certainly, these nanothreads obtained from different precursors have their unique features. It has been expected that more polymers result in the expansion of the sizes of certain threads as the synthesis pressure continues to be reduced. Take furan as an example, the scalable synthesis of nanothread based on molecular furan has been achieved through ambient temperature pressure-induced polymerization (where an onset reaction pressure was only 10 GPa). When slowly compressed to 15 GPa and gradually decompressed to 1.5 GPa, a sharp 6-fold diffraction pattern was observed *in situ*, the formation of a well-ordered crystalline material from liquid

furan. The structure of furan did comprise a cyclic array of π-orbitals, yet the added stability from them was far less. The electronegativity of the oxygen atom in furan reduced this energy to only 0.007 eV per electron, meaning its vulnerability to addition reactions. Both merits reduced the aromaticity of furan compared to benzene or pyridine, aiding the synthesis at reduced pressure [77]. One ^{13}C-enrichment nanothread from furan, characterized by the use of a full complement of advanced solid-state NMR techniques, represented the first molecular-level identification of a specific type of nanothread. The typical length of a perfect, fully saturated thread segment was around 14-18 bonds. Accordingly, they constituted small clusters that likely reside within an overall hexagonal thread packing along with other, less-perfect, or less-saturated brethren [84]. Similarly, crystalline poly-2,5-Furandicarboxylic acid (poly-FDCA) carbon nanothread with a uniform syn-configuration was obtained above 11 GPa, with the help of perfectly aligned π–π stacked molecules and strong intermolecular hydrogen bonds. Benefiting from the abundant carbonyl groups, the poly-FDCA showed a high specific capacity of 375 mAh g^{-1} as an anode material of a lithium battery, with excellent Coulombic efficiency and rate performance [85].

More precursors and features of their derived nanothreads are summarized in **Table 1** together with the experimental conditions (e.g., pressure, temperature). In short, different precursors as reactants do bring new synthesis mechanisms, unique features, and potential applications of different diamond nanothreads.

Table 1. Diamond nanothreads synthesized using various precursors

	Precursor(s)	Experimental details (compressed precursors to)	Features	Ref.
Experimental synthesis	Aniline	33 GPa at 550 K for 24 h	fully sp^3 hybridized; -NH_2 groups as potential active sites	[86]
	Aryl/Perfluoroaryl Co-crystals (ArOH:ArFCHO and ArCHO:ArFOH)	21 GPa		[87]
	Azobenzene	20 GPa at room temperature	high density; with azo group	[88]

Cubane	30 GPa at 523 K	extremely small thickness ~0.2 nm; commensurate stiffness	[79]
Diphenylacetylene	25-30 GPa at room temperature	optical bandgap of 1.74 eV potential as an organic semiconductor with outstanding mechanical properties	[89]
1,2-diazine	32 GPa	uniform chemical structure with exceptional long-range order; heteroatom incorporation	[90]
Furan	15 GPa for 10-12 h	low reaction onset pressure	[77, 84]
2,5-furandicarboxylic acid	11 GPa followed by heating at 593 K and 623 K for 20 minutes or 12 GPa at 603 K and 623 K for 20 minutes	high specific capacity of 375 mAh g^{-1} benefiting from the abundant -COOH groups	[85]
Pyridine	23 GPa for 1 h then released to ambient over 8−10 h.	exhibiting photoluminescence and a higher tensile and bending stiffness	[80, 82]
Thiophene	35 GPa for 10-12 h	high tensile Young's modulus; high tensile strength and excellent ductility	[78a, 91]
s-Triazine	10.2 GPa at 573K	hexagonally stacked tube (3,0) structure with perfect intrathread ordering and uniform azimuthal orientation	[92]

	Precursor(s)	Theoretical Methods	Features	Ref.
Theoretical derivation	toluene (-CH_3) aniline (-NH_2) phenol (-OH) fluorobenzene (-F)	DFT calculations	functional groups with atoms more electronegative than carbon confer a polar character to the material	[93]
	borazine	DFT calculations	high mechanical strength; properties such as piezoelectricity and flexoelectricity may be accessible to the polar lattice	[94]
	polycyclic aromatic	DFT calculations and	improved 1D strength and bending	[95]

hydrocarbon (11 different molecules)	classical MD simulations	modulus due to larger diameters	
Porphyrin	DFT calculations	remarkable mechanical strength and conducting behavior	[96]

Despite the uncertainty of such atomic structures, there are still many works that deserved to be done. The properties of diamond nanothreads have been extensively investigated by computation. It is believed that the strength and stiffness of diamond nanothreads are higher than that of carbon nanotubes or conventional high-strength polymers, originating from a diamond-like sp^3 structure. In this context, the mechanical properties of soft-chiral diamond nanothreads were explored using full atomistic molecular dynamics (MD) simulations. Some simulated results include Young's modulus of 29 GPa, a failure strength of 79 GPa, an axial stiffness of approximately 665 − 850 GPa, a strength of 26.4 nN (134 GPa), an extension of 14.9%, the bending rigidity of 5.3×10^{-28} N m^2, and the specific strength of 3.9×10^7 to 4.1×10^7 N·m kg^{-1}, when the structure is one kind of soft-chair with two SW defects [62a]. As for stiff-chiral nanothreads, Young's modulus and failure strength are as high as 109 and 141 GPa, respectively [97]. Later, these mechanical properties were confirmed by means of the DFT simulations. The ideal strength of diamond nanothreads is as high as 15.7 nN (or 2.6×10^7 N m kg^{-1}) and the stiffness is as high as 168 nN (or 2.8×10^8 N m kg^{-1}) [62d]. The mechanical properties of 15 stable nanothreads vary. The failure strength and Young's modulus for the stiff-chiral ones are 141 GPa and 1.1 TPa at 1 K, respectively. They were believed to originate from the different stress distributions, as determined by their structures, namely achiral, stiff-chiral, and soft-chiral [97]. The purely 6-membered rings on the surface demonstrated superior tensile stiffness, strength and mechanical toughness to others. Those of nonlinear soft chiral structures showed significantly lower tensile stiffness than those of straight chiral and still chiral as a result of their helically coiled morphologies [63]. The purely 6-membered carbon rings have high thermal stability and melting points, whereas nanothreads with dissimilar and distorted carbon polygons have lower melting points [98].

In addition to the extraordinary mechanical properties, diamond nanothreads exhibit intriguing and different mechanical responses. They can be transferred from brittle to ductile behavior. In a

long diamond nanothreads molecule, the SW defect is considered as the grain boundary that interrupts the consistency of the poly-benzene rings. When the length of poly-benzene between two defects is decreased, it shows a brittle to ductile transformation. Such a transition arises from the hardening process of the SW defects under tension [62b]. Different from the study on the effect of different SW contents on their tensile properties, the tensile and bending mechanical properties of diamond nanothreads were considered using full atomistic first principles-based ReaxFF MD simulations, where 15 energy-favorable nanothreads and dehydrogenation counterparts were researched. Diamond nanothreads #8 (kind of stiff-chiral) and #14 (kind of soft-chiral) undergo a brittle to ductile transition at a high temperature of 2000 K. The straight diamond nanothreads that are composed of purely hexagonal carbon rings on the surface (achiral) show superior tensile stiffness, strength and mechanical toughness to other nanothreads. For those of nonlinear soft-chiral structures, they have significantly lower tensile stiffness than those of straight achiral and stiff-chiral ones as a result of their helically coiled morphologies. Further MD simulations of dehydrogenated nanothreads demonstrated that dehydrogenation strongly affects their tensile and bending properties. For tensile tests, it was found that dehydrogenation has a strongly strengthened effect on the tensile stiffness, but not on the failure strains. The tensile stiffness, toughness and ductility are enhanced by approximately 1-fold, 2-folds and 3-folds as much of their pristine values, respectively. Similar to the thermal-induced transition of fracture patterns, dehydrogenation also changes the fracture pattern from brittle to ductile at low temperatures. This can be explained by that atomic stress distribution in units is changed as a consequence of the changes in the dehydrogenated carbon in nanothreads [63]

The impact of SW defects on nanothreads is manifested in their thermal stability [98] and thermal conductivities [62c]. The melting point of DNTs decreases with the increase of the density of SW defects [98]. Due to the existence of the SW transformations, DNTs exhibit a superlattice thermal transport characteristic. Their thermal conductivity shows uniform reduction and then enhancement profile with respect to the number of poly-benzene rings. Such a phenomenon is supposed to result from the transition from wave-dominated to particle-dominated transport regions [62c].

Diamond nanothreads possess ultrahigh mass sensitivity as well as a very high-quality factor. On the one hand, the studied diamond nanothreads demonstrated an extreme mass resolution of ~0.58 yg (1 yg = 10^{-24} g). Moreover, the sensing performance of nanothreads was highly tunable

owing to their tailorable structures. Diamond nanothreads exhibit a very low intrinsic energy dissipation and thus a high-quality factor that is generally two times higher than that of carbon nanotubes [65]. They also possess higher interfacial thermal conductance. The interfacial thermal resistance is 3.1×10^{-9} K m^2 W^{-1}. Both compressive and stretching interfacial distances were found to enhance their interfacial thermal conductance. Particularly, diamond nanothreads having a hydrogenated surface were ready to introduce covalent linkers in the polymer matrix, remarkably enhancing their interfacial thermal conductance [62e].

Thanks to these excellent mechanical properties, diamond nanothreads have been predicted to be promising candidates for reinforcement in polymer composites [14a, 62e, 64, 99]. Some possible reasons have been proposed and discussed. For example, diamond nanothreads is robust and with ultra-light density. It can strengthen the mechanical properties of the polymer but not gain excessive weight [14a, 64, 99a-f]. Moreover, diamond nanothreads own irregular surfaces to facilitate interfacial load transformation, especially compensating the van der Waals interactions weakened by hydrogen atoms [14a, 99b]; Furthermore, hydrogen-terminated diamond nanothreads are useful for introducing functional groups to enhance covalent mechanical interlocking in interfacial load transfer [14a, 64, 99b, 99e]. Last but at least, diamond nanothreads are thermally conductive. The interfacial thermal resistance between two roots of nanothreads is as low as 3.1×10^{-9} K m^2 W^{-1}, even smaller than that of CNTs. They are thus excellent alternative nanofillers for polymer composites with enhanced thermal conductivities [62e]. For instance, Young's modulus and yielding stress of methyl methacrylate (PMMA) were enhanced by 85% and 15% after the incorporation of DNTs [64]. Their interfacial shear strength was 34% above that of CNTs. The related glass transition temperature (T_g) was enhanced to 70 K [99b, 99d]. The cross-links between fillers and polymers were further introduced to provide bidirectional hindrance for free motions of polymer chains [99b]. The atomistic simulations showed that diamond nanothreads can act as the nano-attractor to reduce the tensile crazing damage in polymer nanocomposites [99g]. The friction coefficient of PMMA was significantly reduced by a factor of 26% after the incorporation of diamond nanothreads. The degradation mechanism was attributed to the generation of free volume at the interface, decreased interfacial shear strength, restrained movements of the polymer chains near the interface, and reduced surface attachment of polymer chains [99e].

Note that most considerations of current studies on diamond nanothread are only focused on

the axial insertion of one single or perfectly aligned several nanothreads [14a, 64, 99a, 99b, 99d-g] into polymers. This aims to explore changes in the properties of diamond nanothread, where the mechanical properties of the polymers can be increased. For practical applications, the reinforcer is more randomly distributed in the polymer matrixes. For example, the deterioration on tensile properties was found [99c, 99f], due to the introduction of continuous lower-density interphases that surrounded the nanothreads. In other words, the mobility of PMMA chains was promoted [99c]. The axial thermal conductivity of polyethylene nanocomposites was linearly increased with the content of regularly aligned fillers. It was irrelevant with randomly dispersed nanothreads for lacking effective heat transfer channels and the transverse thermal conductivity was degraded [99f]. These findings shed light on the gap between theoretical assumptions and practical possibilities, that randomly dispersed nanothreads can not achieve the requirement for mechanical properties enhancement. Tracing the changes after the introduction of different functional groups is one the of research directions for future work on diamond nanothreads.

Diamond nanothreads have been predicted to be promising candidates for fiber applications [14b, 100], owing to their ultrathin dimensions and non-smooth surfaces. For example, diamond nanothreads possess excellent torsional deformation capability and excellent load-transfer efficiency. Their sp^3 structure makes them easy to build into inter-thread cross-links, which provide strong interface load-transfer efficiencies. According to high-throughput large-scale MD simulations, the torsional behavior of nanothreads bundles was strongly dependent on the loading direction. Therefore, diamond nanothreads are ideal for next-generation high-performance fiber applications [14b, 100a]. In addition, nanothreads bundles exhibited a high mechanical energy storage density. The gravimetric energy density reached 1.76 $M \cdot J\ kg^{-1}$ under pure tension, which was higher than that of a steel spring. A decrease in the number of filaments led to the reduction of torsion and tension as two dominant contributors. The mechanical energy storage capacity of nanothreads bundles was comparable to that of carbon nanotubes. The nanothreads bundles had better structural stability at strain, and bigger maximum elastic torsional deformation [100b].

In addition to the applications of nanothreads or their parallel compositions with bundles, the development of more complex 2D or 3D diamond nanothreads has been triggered [101], especially the related theoretical exploration. For example, 2D porous diamond nanothreads were named as diamond nanomesh and the 3D diamond nanothreads as diamond nanofoam. They were believed

to be composed of C-C covalent bonds after the partial surface dehydrogenation, or changing to polycyclic aromatic hydrocarbon (PAH) molecule as the precursor, which was different from the synthesis of 1D nanothreads from PAH in the previous session. Both 2D diamond nanomesh and 3D diamond nanofoam were proved to have high mechanical strength analogously to diamond nanothreads, low densities, high porosities, and consequently high specific surface areas. They are thus promising in the applications of reinforced nanocomposites, gas storage/separation, and sensor formation.

2.5. Diamond fibers

Encapsulation of a fiber substrate with successive diamond nanoparticles or diamond films by means of the CVD technique is a common approach to create core-shell diamond nanostructures. The used fibers include carbon fibers [3, 7, 102], CNTs [103], silicon fibers [104], and metal fibers [4]. Since carbon fiber is a sp^2-hybrid carbon material, it is easy to be attacked by hydrogen plasma in a harsh CVD environment. To avoid being etched during the CVD process, it is necessary to choose the appropriate fiber or coat carbon fibers with a corrosion-resistant layer. For example, carbon fibers with larger crystallite sizes are less susceptible to be etched compared to carbon fibers with smaller ones. A dense seeding with smaller-sized nanodiamonds resulted in faster coalescence, which provided significant benefits as the diamond layer protects the carbon fiber [102]. The addition of a TiC interlayer between the BDD film and the carbon fiber surface [3a, 7] improved the adhesion of the core and the shell as well as impeded significant hydrogen etching of the carbon fibers.

These core-shell diamond film/carbon fiber products combine the properties of carbon fibers with those of diamond. For example, they are promising candidates of wearable electronics, owning to their good conductivity, excellent flexibility, ultra-weight from carbon fiber and wide potential windows, and long-term stability of diamond. The fiber-based supercapacitors possessed outperforming gravimetric and volumetric energy- and power- densities, even under severe bending state. They facilitated their applications for these flexible electrodes in the energy and electronics fields [7]. These fibers were also used as mini-implants for monitoring both electrophysiological and biochemical biomarkers. For the small carbon fibers that have similar diameters to the soma of individual neurons, lower electrode failure and less tissue damage were realized. Their biochemical longevity, well tolerated *in vivo*, additional with exceptionally long-

lasting and electrochemically robust *in vivo* of the diamond film determined that diamond fibers were ideal for high-resolution and single neuron neural interface electrodes for closed-loop medical devices [3b].

3. 2D diamond nanostructures

3.1. Diamond films

After synthetic diamond deposition on flat substrates by means of the CVD technique was proposed in 1952 [105], diamond film has become one of the most common synthetic products. The employed substrates cover silicon, quartz, and metals. Such diamond film is the basis of many diamond structures. In addition, there are many other methods to synthesize diamond films, such as physical vapor deposition (PVD) [106] or combustion flame synthesis [107].

For the CVD growth of diamond films on a selected substrate, the thermal expansion coefficient (CTE) difference between the substrate and diamond film is one of the most important parameters that need to be considered. For example, a silicon substrate is the most frequently used, originating from its slight CTE mismatch with a diamond film. Meanwhile, silicon is stable during the hash CVD environment. It is also commercially available. For some practical applications, other substrates have been applied, such as stainless steel for food as well as medical treatment [108], SiC for high-efficiency power electronics [109], and cemented carbide for machining [110]. Unfortunately, the CTE mismatches between these substrates and diamond films are too big. In other words, diamond films are hard to be successfully attached in some cases. To overcome such a challenge, an interlayer between the substrate and the as-grown diamond layer was added since it is indispensable to prevent film flaking and wearing. The interlayers studied up to now include AlN [111], Al/AlSiN [108c], Cr/CrN [108a], Cr/CrSiN [108e], Cr/Cr-Al-N [109], and Cr/CrN/CrTiAlN [108b]. Among them, Al and Cr have gained much attention. This is because alumina or chromium carbides can be formed on the diamond surface, suppressing the formation of cracks and their propagation and eventually enhancing diamond adhesion. For example, the Cr interlayer protected stainless steel/diamond films improved diamond toughness, corrosion resistance, and biocompatibility [108]. These interlayer materials served as the barriers to suppress the carbon diffusion inwards and iron diffusion outwards. The catalytic reaction of iron or nickel in the stainless steel led to the formation of a graphite phase

[108a]. Composing aluminum or chromium-related materials (for a synergistic effect) or the addition of extra Si (to increase the amount of chromium carbides) have been found useful for improving the attachment of diamond films on these substrates [108b-f].

Thanks to the development of the CVD technology, nowadays it is more possible to obtain smooth, continuous, and pinhole-free diamond films. Inside a CVD reaction chamber, the growth of diamond films follows the Volmer-Weber model principle. The impacting adatoms are preferentially combined with the existing fixed seeds. Subsequently, isolated 3D islands are grown horizontally and vertically, leading to the formation of a coalesced diamond film. Nowadays, large and high-quality diamond films with high-growth speed diamond films are still required.

With respect to thinner diamond films, the CVD experimental conditions must be precisely controlled, including the subtracted temperature, vacuum pressure, and the composition/proportion of gas precursors. Again, the choice of a suitable substrate that matches TEC with diamond films is extremely critical. The use of transition metal materials must be avoided since they are possible to etch diamond. The nucleation densities of diamond nanoparticles on the substrates must be enhanced and it is of pivotal importance. This is because the growth on diamond seeds is possible in all directions. The denser the seeds are distributed, the faster they coalesce on the plane, eventually ending with longitudinal growth and a thinner film. The nucleation generally includes abrasion, micro-chipping, electrostatic self-assembly seeding, and chemical nucleation [105]. The abrasion and micro-chipping denote physical scratching through diamond seeds on the substrate. They are efficient and simple, but leave score or embed residual diamond on the substrate, causing inhomogeneous and damage. Self-assembly seeding refers to the adsorption of deagglomerated or charged diamond nanoparticles to the substrate surface as high density and homogeneity as possible with the help of chemical reactant(s) or physical means (e.g., in an ultrasonic bath). Up to now, the seeding densities with the aid of self-assembly seeding are possible to be varied in a wide range [112].

Theoretical predictions have pointed out that continuous diamond coating on a foreign substrate requires a minimum film thickness of 100 nm. The reduction of diamond film thickness is of pivotal importance to endow ultrathin diamond films with high optical transparency and a certain flexibility, heightened its applications in material science, engineering, chemistry, and physics. A piece of quartz glass has been coated with a 50-nm thick diamond nanofilm. It

exhibited a high optical transparency of 90% in air and 98% underwater in UV–vis range. In assistance of intrinsic properties of underwater superoleophobicity and self-cleaning ability, such thin diamond nanofilms were suggested to be promising as aircraft fairing and window or optical lens [113]. Diamond is originally the hardest natural material in the world. However, as long as the thickness of a diamond film is thin enough, its flexural rigidities are greatly reduced. Namely, such thin diamond films own a certain degree of softness. By thinning nanocrystalline diamond membranes, the 40 nm thick free-standing membranes have been successfully rolled into a variety of 3D complicated architectures [114].

Smooth and thin diamond films have been investigated. For example, nitrogen or argon have been injected into the CVD reactor during the selection of CVD experimental gases (e.g., the necessary carbon source and hydrogen). It has been assumed that heavier atoms impact the carbon source molecules to obtain more C_2 structures, strengthen the secondary nucleation, limit competitive overgrowth, and reduce the height difference from peak to valley between large grains. Smoother diamond films were then obtained. On the other hand, the rich sp^2 carbon phase on the grain boundary of diamond films needs to be taken into consideration. Taking the WC-Co substrate as an example, the substrate material had to be treated before diamond deposition. In this way, Co diffusion was prevented. The segregation of Co to the surface of cemented carbide material catalyzed the graphite phase, leading to the formation of the non-uniform diamond film and seriously affecting diamond adhesion [112e, 115].

In addition to the condition control before or during the CVD growth, post-experimental processing is an effective method to grow smooth and thin diamond films. Mechanical/chemical polishing is the most frequently applied method to get smooth diamond films, surface damage or contamination introduced takes place though. Mechanical grinding, as the name implies, is to use od a corundum grinding wheel to polish diamond films. Nowadays, chemical grinding or chemical-physical grinding has been more frequently employed. Active metals, iron, and titanium must be added on the basis of physical grinding. The active metal first reacts with the diamond. In other words, diamond is graphitized or the formation of carbides occurs. These softer non-diamond phases and carbides are possible to be removed by abrasives [116]. In order to enhance the efficiency of chemical polishing, oxalic acid was added to the grinding slurry. The final roughness of such polished diamond films was only about 1.8 nm [117].

Synthesis of large area and thin diamond films with high speed is one hot topic of diamond

growth. For example, three-point plasma sources have been arranged to produce large-sized diamond films. Precise control of reactive gases ratios varied the power density of a CVD reactor. Another approach to achieve high-speed growth is by precise control of reactive gas ratios during the CVD process[118]. New in-liquid MWCVD processes with the addition of alcohols have been used to grow continuous diamond films only within 3 min [119]. In a laser-assisted CVD reactor, the photogenerated reactive species, OH, CH and C_2 radicals were found to play critical roles in the growth of large-area diamond films. The OH radicals etched the surface-bond hydrogen and stabilized the sp^3 hybridized surface carbon bonds; the CH or C_2 radicals were believed to be energetically favorable and made the growth of the existing crystal proceed readily. Photolysis of hydrocarbon and suppression of nondiamond accumulation significantly shortened nucleation time, promoting diamond film growth rates and quality [120].

Dimond film is an interesting material for mid-infrared spectroscopy (MIR) due to its transparency, comparatively low refractive index, excellent broadband transmission properties, and extreme inert and resist physical damage. Attenuated total reflection (ATR) crystals are commonly used as MIR waveguides for probing liquid-phase and solid samples, by taking advantage of the evanescent field generated via internal total reflection. The applied ATR waveguide made from diamond can be utilized in most demanding circumstances. In contrast with commonly crystal materials, diamond ATR crystals are suitable for corrosive media as well as sharp-edged solids [121]. In 2014, the microfabricated diamond strip waveguides as optical transducers for MIR chemical sensing was presented for the first time. The ability to detect acetone in D_2O of this MIR sensor equipped with thin-film diamond was competitive to GaAs/AlGaAs semiconductor waveguides [121b]. Then, the analytical sensing platform for protein amide I bands in bovine serum albumin [122], or glucose in human saliva sample [123] were built up, contributed by the biocompatibility of diamond. Recently, diamond waveguide coupled to a tunable quantum cascade laser was proved to be suitable for the analysis of real-world samples such as the quantification of caffeine. According to the correlation between the absorbance spectrum of the C=O vibrations and the concentration, the limit of detection (LOD) was 0.019 %w/w [121c]. This kind of innovative diamond thin-film-waveguide-based sensors has been confirmed as an innovative analytical tool, which may be used in a wide range of application scenarios, ranging from environmental to biomedical sensing.

3.2. Diamanes

Diamane, an incipient 2D film, was theoretically predicted in 2009 [15d] and experimentally confirmed in 2020 [124]. Theoretical derivations have predicted that when bilayer graphene is arranged in parallel either in AB or AA stacking way, the interlayer C-C covalent bonds will be established between two carbon atoms at the top and the bottom. The prerequisite is that neighbor carbon atoms in near sublattice are passivated by hydrogen atoms. Under such conditions, every carbon atom is in the sp^3 hybridization state, accomplishing translation from the sp^2 hybridization to the sp^3 hybridization. The name of diamane is thus referred to the terminology regular of graphane, derived from graphene hydrogenation. More strictly, there are two kinds of configurations for diamane: AA-staking (Lonsdaleite) and AB-staking (Bernal) **(Figure 7a, 7b, 7c)**.

The first and up to now the only report [124] about total conversation from two-layer graphene film to genuine diamane was performed by chemisorption of hydrogen, which was generated from the dissociation of H_2 in a hot filament reactor at a temperature of 325 ℃ and a pressure of 50 Torr. The UV Raman spectroscopy has been applied to characterize as-synthesized diamane, in order to avoid the high performance of sp^2 carbon in normal Raman scattering. For bilayer graphene, it is known that the sharp G peak at around 1582 cm^{-1} results from typical sp^2 carbon stretching. After the application of a hydrogenation process on them, drastic changes were observed in their UV Raman spectra, where no G peaks were detectable. A new sharp peak appeared at around 1344 - 1367 cm^{-1} **(Figure 7d, 7e)**. This peak was assumed to be resulted from the bond stretching between sp^3 carbon in diamane. According to *ab initio* calculations, the Raman peak of diamane is expected to show up at near 1320 cm^{-1} [124-125]. The difference between experimental and theoretical values of these wavelengths was explained from the following aspects. Firstly, the stacking way of diamane has not been fully revealed. Only the exitance of AB or AA stacking was proved. Note that the stacking way of bilayer graphene is actually random. Secondly, the stress or strain at the grain boundaries between graphenic and diamane domains is expected to affect the C-C interlayer bonding and the resultant variety of up-shifted positions of the peak. The selected area diffraction pattern of diamane shew a single domain, close to an AB (or AA) stacking bilayer graphene domain **(Figure 7f, 7g)** [124].

The two examples above discussed the phase translation of two-layered graphene after chemisorption of hydrogen on its surface. There are two factors deserving of pondering. The first

one is that the phase transition is triggered by hydrogen chemisorption on the surface. Generally speaking, surface modification can optimize the properties of the material, far less to change the noumenon. In this case, there is a bilayer structure. In contrast to 3D bulk, its lattice organization underneath should still be compelled to change its thickness (namely at the nanometer scale), although the downward effect of surface modification is quite small. This kind of conversion touched off by surface hydrogen adsorption under reduced or no pressure was divided into "chemically induced phase transition". The principle of this transition is that surface conditions directly affect thermodynamics. In more detail, surface adsorption of hydrogen atoms causes a high strain of atomic lattice by unpaired electrons of carbon atoms that are not bonded to hydrogen. The binding of neighboring graphene layers forms a bilayer sp^3 diamond lattice without an activation barrier. The subsequent propagation through the graphene in-plane leads to the formation of interlayer carbon bonds.

Normally, phase conversion from bilayer graphite to diamond was occurred under high pressure and high temperature. But high pressure was with possibility no more the unavoidable condition if monodispersed transition metals, such as Ta, Ir, Zr, Ag, Pt, Re, and Hf, participated the transformation. The atomic radius of these metal atoms was 0.136−0.160 nm [126]. The results from first-principles calculations shew that affecting the energy barrier of the conversion are the outer valence orbital and the atomic radius of metal atoms. During the conversion, the p-orbital of C atoms with dangling bonds hybridize with the d-orbital of the metal atom to form bonds, making the sp^2 to sp^3 bonding easier. The greater charge transfer and proper position of charge accumulation between the metal and the dangling C atoms formed stronger metal−C bonds with a lower energy barrier of transition [126d].

The second question was if chemisorption is enough for bilayer graphene, how about the few layers of graphene (FLG). If hydrogen atoms can provoke this transition, how about other active species? To answer these questions, it is necessary to describe diamane and some already-appeared derivatives. The bilayer interlayer sp^3-bonded graphene is called as diamane, while the few-layer one is diamanoïd (transversion happened only in the top two layers) [125, 127]. When the surface is passivated by halogen atoms, the products are X-diamane [128]. Other related materials are kind of composites containing sp^2 and sp^3 hybridization carbon, different with the definition of full sp^3 hybridization carbon of diamane, such as diamene (without any passivation) [129] and diamondene (only the top layer was terminated by -OH groups) [130].

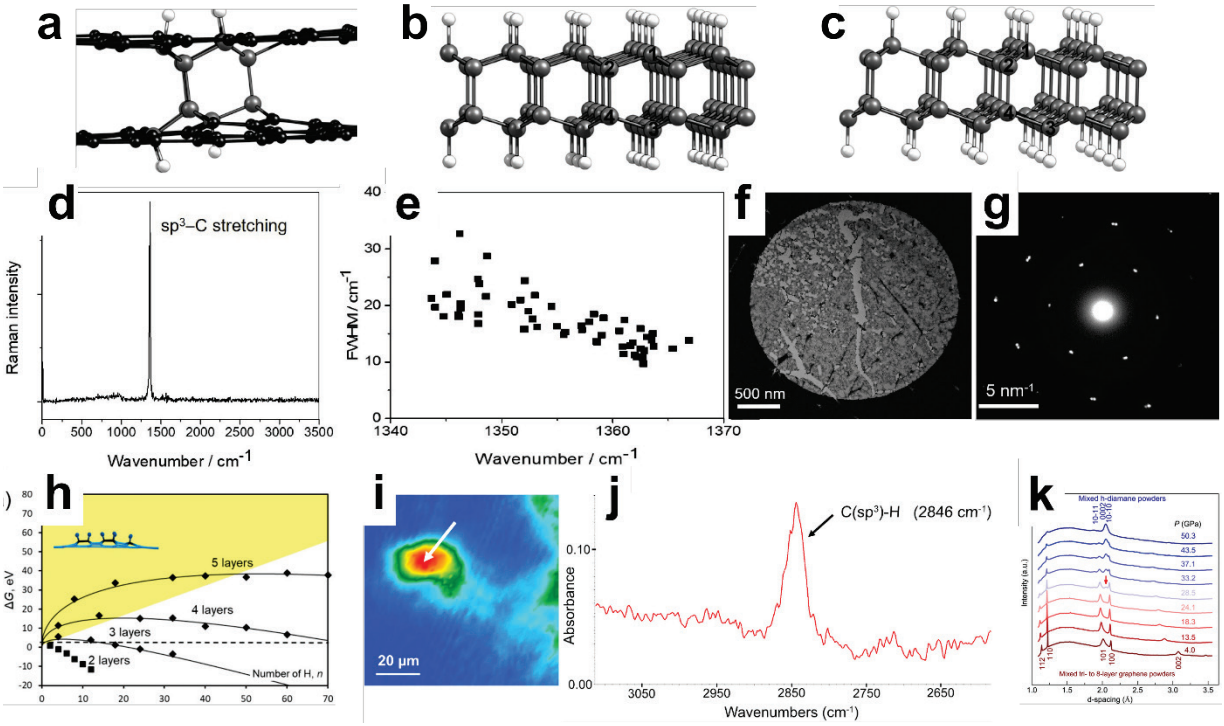

Figure 7. (a) scheme of a interlayer C-C bond formation process of one diamane nuclei; atomic structures of (b) AA stacking and (c) AB stacking, white, black, or gray spheres representing H atoms and in-plane carbon atoms, respectively [15d]; Reproduced with permission.[15d] Copyright 2009, Springer Nature. (d) typical Raman spectrum obtained on diamane; (e) full width at half maximum (FWHM) as a function of wavenumber of sp^3-C stretching peak in (d); (f) image of diamane; (g) diffraction patterns of diamane in (f) [124]; Reproduced with permission.[124] Copyright 2020, Elsevier Ltd. (h) transformation energy (ΔG) plotted versus the number of H atoms chemisorbed at the surface without external pressure, yellow shading marks the area of diamond nucleus instability and reversal, preventing diamane formation [131]; Reproduced with permission.[131] Copyright 2020, John Wiley and Sons. (i) typical FTIR-ATR microscopy image processed on the integrated intensity of C-H stretching band of diamanoïd, indicated by the white arrow; (j) typical absorbance FTIR spectrum taken in the region in (i) [125]; Reproduced with permission.[125] Copyright 2019, Elsevier Ltd. (k) XRD results of FLG to diamanoïd under pressure, a new peak arose indicated by the red arrow [127b]. Reproduced with permission.[127b] Copyright 2020, American Chemistry Society.

3.2.1. Diamanoïds

Right before the first synthesis of diamane from bilayer graphene, few-layer graphene (FLG) was chosen as the reactant in the early studies [125, 127c]. This is probably because free-standing single-layer or bilayer graphene was hard to obtain at that time. The related products were then named as diamanoïd. Since diamanoïd was obtained from FLG, it owned a structure with several layers. Only the top surface was passivated by hydrogen atoms and contacted with the second top layer with interlayer C-C bonds, while the bottom layers were graphene. Therefore, diamanoïd is

one kind of carbon composite with bottom sp^2 and top sp^3 carbon.

Later, theoretical predictions proved that the chemisorption of hydrogen atoms on the graphene surface indeed induced phase change. However, such lattice reorganization downward is too small to cause phase change over several layers. As more hydrogen atoms are absorbed on the graphene surface in the hydrogen-rich environment, diamane forms spontaneously. Under such conditions, the thermodynamic threshold of FLG appears significantly increasing. Some necessitating assistance is indispensable, such as pressure. The pressure is expected to increase as the thickness of the applied graphene layers becomes bigger **(Figure 7h)** [131]. For example, compressing trilayer and thicker graphene at room temperature to hexagonal polymorphs (h-diamanoïd) has been demonstrated when a pressure of about 20 GPa was employed. The h-diamanoïd was preserved upon the decompression to about 1.0 GPa [127b]. With the assistance of high pressure, not only hydrogen atoms can compel phase conversion, but also hydroxyl group make contributions [127a, 131]. In a range of 4 - 6 GPa, bilayer, five-layer graphene and graphite were indicated to realize partial phase transition in diamond anvil cells (DACs), in which water was used as the pressure transmitting medium (PTM) to offer -H or -OH functional groups. Such an evolution process was confirmed using MD simulations. The phase transition started from the top two layers after functional groups were absorbed on the top surface. Then covalent bonds between the top sp^3 carbon with underneath graphene layers formed when the pressure was the indispensable prerequisite [127a].

Although diamanoïd differs from diamane, its characterization can provide some reference values for diamane, for example by use of FT-IR (Fourier Transform Infrared) [125], typical electron diffraction pattern [124, 127c], XRD diffraction [127b], and transparency [127a, 127b]. There was a narrow stretching band centered at around 2846 cm^{-1} after hydrogenation of diamanoïd, indicating diamanoïd indeed processed C-H bonding. In its FTIP-ATR (Attenuated Total Reflection mode) spectra, the C-H bonding was shown in a large circular area of about 150 μm^2. Namely, the C-H bonds inside diamanoïd were not the defects at the edge area, but as a result of chemisorption in the planar plane of graphene **(Figure 7i, 7j)** [125]. When the conversion continued, with the increase of pressure, diamanoïd became transparent and a new broad diffraction peak appeared in the XRD pattern **(Figure 7k)** [127a, 127b].

3.2.2. Halogenated diamanes

The synthesis of fluorinated diamane (F-diamane) was actually achieved earlier than that of diamane [128a]. This is because the interlayer C-C bonds can form as a consequence of surface chemisorption at ambient atmosphere, without the need of pressure. Using the synthesis steps of fluorination of graphite as the reference [128e], the AB-stacking bilayer graphene was moved to a XeF_2 vapor rich chamber at near room temperature and under atmospheric pressure. The F-diamane was then obtained after a several-hour exposure. Due to the strongly polarized C-F bonds, F-diamane was identified by means of comprehensive and convincing experimental tools, including XPS, Raman spectroscopy, TEM, and electron energy loss spectroscopy (EELS). In its XPS spectrum, the carbon atoms were found to directly bond to fluorine atoms, resulting from the C-F peak at 288.1 eV. Another peak located at about 285 eV originated from carbon atoms that were not directly bonded with F. The intensities of these two peaks were gradually increased when the fluorination time was increased from 2-3 h to more than 12 h, where their maximum values were kept. In contrast, the intensity of the main peak at 284.2 eV that contributed to sp^2 C-C bonds of the reactant is decreased as a function of the fluorination time **(Figure 8a, 8b)**. The intensity changes of these XPS peaks demonstrated the predicted phase change, although the atomic structure of F-diamane cannot be determined. Later, a supplementary explanation was added by use of ionic signals that were attributed to F-Cu or F-Ni (metal substrate), illustrating the graphene membrane was permeable to fluorine. The presence of fluorine at the interlayer of graphene and the substrate led to the possibility of termination at both sides. The two Raman signatures belonging to pristine graphene — G band and D band — were completely suppressed after the conversion **(Figure 8c)**. The atomic arrangement of F-diamane was further explored using high-resolution TEM **(Figure 8d, 8e)**. The interlayer separation of graphene (3.24 - 3.41 Å) was significantly altered to 2.05 Å (1.93 - 2.18 Å, average 2.05 Å), very close to that of diamond (2.068 Å). This constant agreed well with the DFT calculation results using PBEsol functional [128d]. The characteristic interatomic distance was 1.58 - 1.89 Å and the hexagonal lattice constant was found to be 2.546 Å [128d]. These results indicated the complete phase transition over a large area and kept high stability during the data collecting period for about 48 h. When comparing the synthesis conditions with diamene, diamondene, or diamane itself, the experimental environment of F-diamane was much milder. For example, the ultra-high temperature, pressure or high initial gas energy was not necessary [128a]. This experimental accomplishment was believed to pave the path for the realization of other diamane counterparts, such as those synthesizable from

chlorinated or brominated graphene.

Among the emerged 2D sp^3 ordered structures, the synthesis process of diamane and F-diamane was truly simple. The stability of F-diamane was high (e.g., as emphasized for its existence about 48 h). The reasons were explained as follows. One can express the theoretical nucleation barrier of diamane and F-diamane formation using the ΔG (Gibbs free energy), namely the energy difference between the sp^3-diamond state of the chemically bonded interior and the all sp^2-graphene layers. For diamane or F-diamane, continuous decline of ΔG took place when H or F absorption on the active species of graphene continued happening, namely when the formation of diamane and F-diamane were spontaneously formed from a thermodynamic perspective [131]. The dynamic stability of diamane and F-diamane was then examined by calculating the phonon dispersion relations along the high symmetry directions. For F-diamane, there was the absence of imaginary frequency throughout the whole first Brillouin zone in the phonon dispersion relations, confirming the dynamical and structural stability [128b, 128g]. The thermal stability of F-diamane was better than that of diamane. This was because the formation energy in the case of fluorinations was significantly lower (almost 1 eV), stemming from the weaker bond in F_2 compared with the H_2 molecule and the reduced configuration space [132]. The binding energy E_B of F-diamane was calculated to be 6.672 eV per atom, whose energetic stability was better than other X-diamane, such as Cl-diamane and Br-diamane [128g].

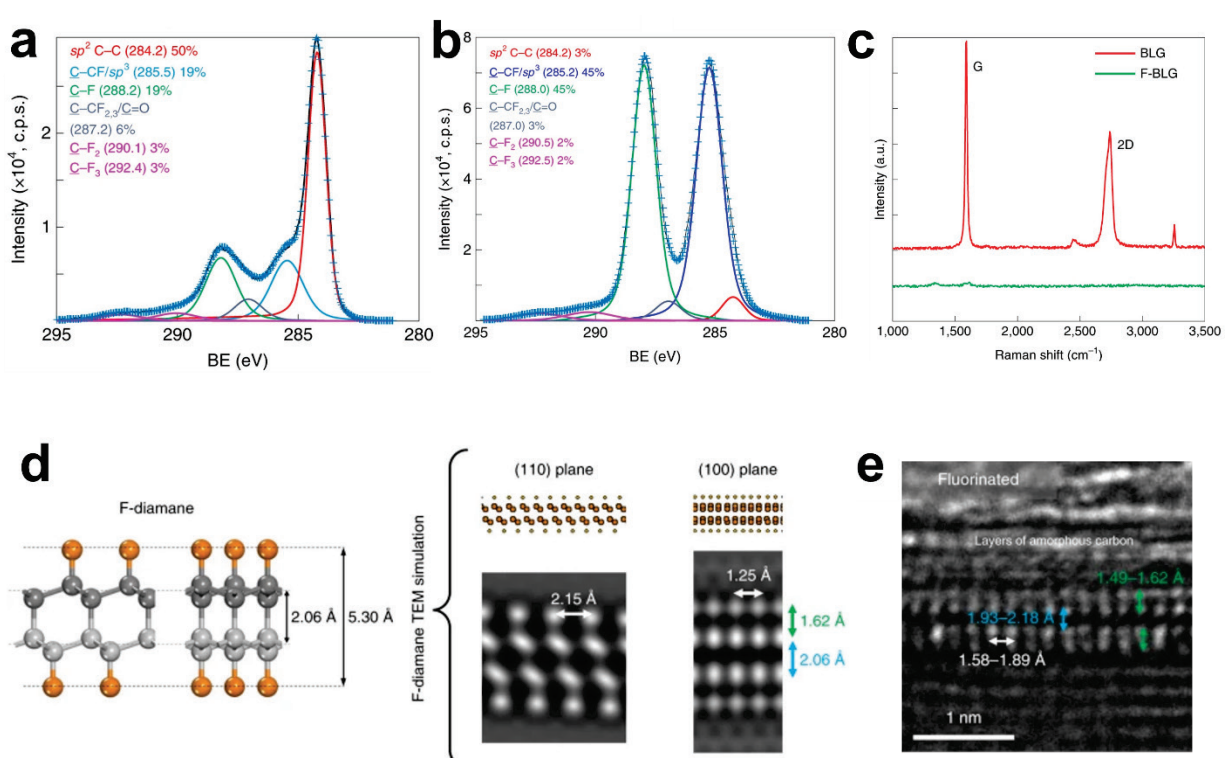

Figure 8. (a-b) XPS characterizations of bilayer graphene fluorinated about 2-3 h (a), and over 12 h (b); (c) Raman spectra, (d) simulated HR-TEM images, (e) high-resolution cross-sectional TEM of F-diamane [128a]. Reproduced with permission.[128a] Copyright 2019, Springer Nature.

It is worth mentioning that chemical inducing lattice swift with H, F, or Cl (diamane, F-diamane or Cl-diamane) atoms has been developed as the main pathway to vary nanometer scale thickness layers under milder thermodynamic conditions [131]. The calculation results of various properties of halogenated diamane have been accomplished **(Table 2)**. The phonon dispersion showed that halogenated diamanes are dynamic and structure stable. Their electronic band structures and absorption ability proved that halogenated diamanes are highly promising in the assembly of electronic and optoelectronic devices [128b, 128f, 128g].

Table 2. Properties of pristine diamane and five types of halogenated diamanes

C_4X_2	C_4H_2	C_4F_2	C_4Cl_2	C_4HF	C_4HCl	C_4FCl
Phase space ($\times 10^{-4}$) [128d]	5.79	14.1	20.8	9.94	12.6	17.8

Thickness (Å) [128d]	6.95	8.23	9.5	7.59	8.22	8.55
Young's modulus (N/m) [128c, 133]	491	481	395	-	-	-
Shear modulus (N/m) [128c, 133]	226	217	168	-	-	-
Elastic modulus (GPa) [128b, 134]	692	574	430	633	550	522
Tensile strength [128b]	62.5	47.2	19.7	-	-	-
Band gap (eV)-HSE06 [128b-d, 128g, 133]	3.86	5.68	2.42	4.17	0.86	2.05
Thermal conductivity (W/mK) [128d]	1145	377	146	454	244	196
Optical absorption properties [128b, 128f, 133]	ultraviolet region		visible and near-ultraviolet region	-	-	visible and near-ultraviolet region
Structures [128d]	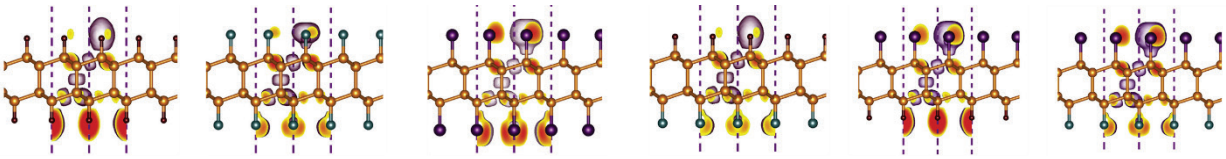					

Reproduced with permission.[128d] Copyright 2020, Elsevier Ltd.

3.2.3. Diamene

Different from diamane, diamanoïd, or F-diamane, the synthesis of diamene and diamondene [130] must be performed under high pressures. The biggest distinction between diamene and diamane is that both surfaces of diamene are not been terminated by hydrogen atoms. Their structures are more similar to graphene than graphane. Diamene was first observed in 2018 [129a]

and later post-scripted [129c-e]. Experimentally, two layers of epitaxial graphene films were placed on a SiC substrate at room temperature. A top-down nano-indentation on the order of 100 nN was then imposed on the surface to indent films **(Figure 9a, 9b, 9c)**. The changes of corresponding properties (e.g., stiffness, hardness, and electrical conductivity) relative to two-layer epitaxial graphene were detected, illustrating the transformation. The first uplifting discovery was the transverse stiffness (> 400 GPa). It was much larger than the previous one. This transverse Young's modulus was even higher than that of the SiC substrate. Among other hard film structures as a reference, such as CVD diamond (923±78 GPa) and sapphire (412±36 GPa), the indentation modulus of diamene (1079±69 GPa) was the biggest **(Figure 9d)** [129e]. Similar results from the microhardness experiments were discovered. No residual indent was found on the surface of in an AFM topographic imaging when the loading force up to 12 μN was performed, indicating close hardness between diamond indenter and diamene **(Figure 9e)**. Once the electrical current flew between the metallic AFM tip and the diamene surface, the load-dependent conductive AFM showed a sudden drop when the load force was larger than 260 nN **(Figure 9f)**. These changes together with the DFT calculations indicated a phase switch from the graphene to diamond.

It has been also revealed that the pressure-induced transversion was only feasible for bilayer graphene and such transversion was reversible. The possible reason was that diamene is unstable. It only exists under high pressures [129a, 129b]. When the indenter leaves away from the surface, all the changes disappear. That is also the reason that its further characterizations using standard techniques (e.g., Raman, FTIR, XPS) were not possible. Here, a popular viewpoint is that diamene is without any passivation [15a]. Some DFT calculations have been carried out, where the upper of diamene was assumed to be terminated by H or OH groups. Note that no evidence was available for such assumptions. Diamene is one kind of sp^2 and sp^3 orbital hybridized carbon on the same plane, which is different from the combination way of diamanoïd, consisting of a layer structure. The phase transformation from 3- or 4-layer was hindered by the layer-stacking configuration. While for bilayer graphene, transformation always happens regardless of the stacking of AA or AB. Moreover, the definition of precursor-bilayer graphene is quite different from that of diamane and related materials. Because the precursor was delimited as a combination of one layer of graphene and one buffer layer. The buffer layer is an interfacial layer between the graphene and the SiC substrate, strongly bonded with the SiC. The synthesis of

diamene was favored by buckling distortions of this buffer layer. In addition, the transition did not occur on other substrates such as SiO_2 [129a, 129c]. Because diamene is ultrahard, it can only persist on the SiC surface under high presser, leading to a straight application to protect the SiC surface. The experiments showed up to 100% increase in hardness and 50-80% increase in elastic modulus of SiC when diamene was formed above. This increase leveled off to about 30% when the indentation load furnace was 10 mN and indentations depths reached 175 nm [129d]. Diamene is isotropic for in-plane thermal expansion with a coefficient of 8.3×10^{-6} K^{-1} [129b]. Except SiC substrate, it was found that metal substrates was energetically favorable to form sp^3 bonds between neighboring carbon layers. When the AB-stacked bilayer graphene was hydrogenated on a metal substrate, the "chair-like" carbon layer could not only be stabilized at the more reactive interface, such as cobalt (0001) and nickel (111), but also could form stable covalent bonds with less reactive interface, such as copper (111). The main driving force for this transformation comes from the hybridization between sp^3 orbitals and dz^2 orbitals on the metal surface [135].

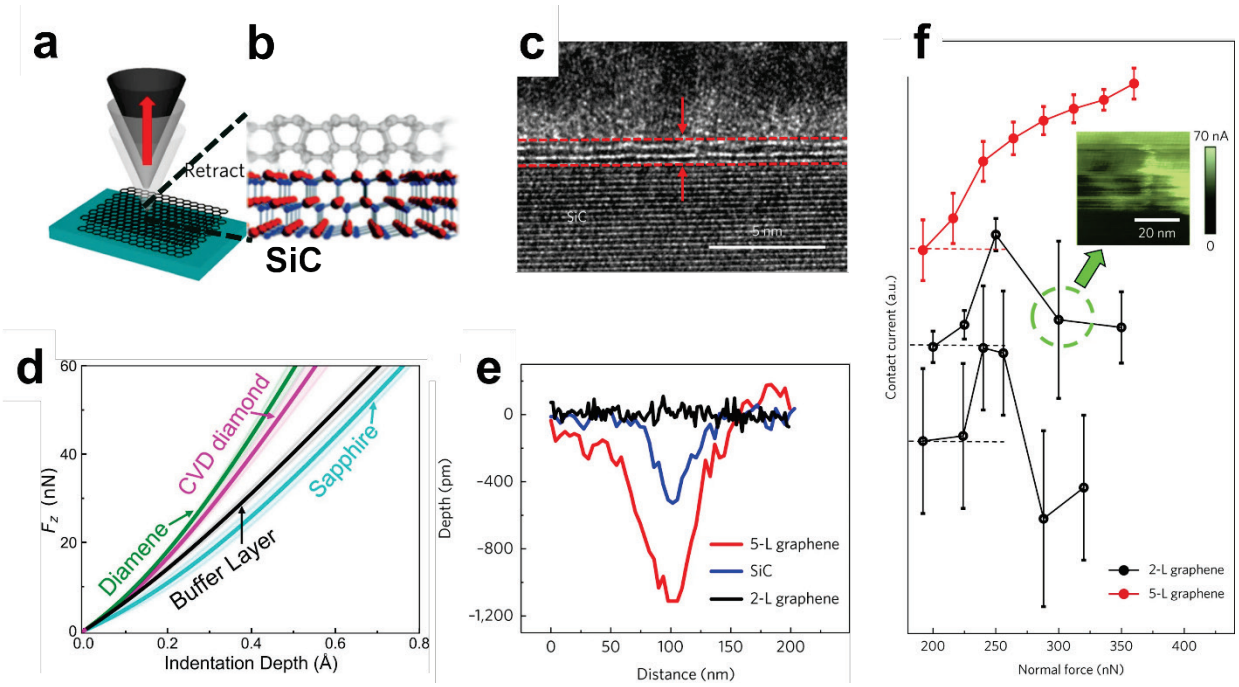

Figure 9. (a) schematic synthesis procedure, two-layer graphene on SiC substrate under nano-indentation and lower layer connected with the substrate [129a]; Reproduced with permission.[129a] Copyright 2017, Springer Nature. (b) scheme of pressure activated diamene structure [129d]; Reproduced under terms of the CC-BY license.[129d] Copyright 2023, the Authors, published by John Wiley and Sons. (c) TEM image (within the red dashed range) [129a]; (d) force versus indentation depth curves [129e]; Reproduced with permission.[129e] Copyright 2018, Elsevier B.V. (e) cross-section profile of residual indents in 5-L graphene, SiC and 2-L graphene, no residual indent occurred in 2-L graphene which was diamene; (f) average current signal versus normal

load of diamene [129a].

3.2.4. Diamondene

Diamondene (or diamondol) is the hybridization combination of sp^2 and sp^3 carbon. As one kind of special diamane, the top H atoms of diamondene are OH groups and its bottom H atoms are removed. Different from diamene, the bottom layer of diamondene is not in contact with the substrate. During the synthesis of diamondene, the compression-induced transition was also not permanent, similar to the conversion process of diamene. Diamondene was not stable because of periodic arranged dangling bonds on the bottom layer. In 2011, diamondene was yielded by a combination of staking, physical-chemical modification and pressure [130a]. The bilayer graphene flakes were observed by means of AFM. Controlled loading force was employed onto graphene flakes by an electric force microscopy (EFM) tip and meanwhile pressure-dependent charge injection experiments were accompanied **(Figure 10a)**. The current change was explained to be due to the rehybridization process and consequent opening of the gap in the upper layers **(Figure 10b)**. This force was to induce phase transition and the charge injection was to test whether the transition really happened. This is because the amount of injection charges will decrease. The exitance of water, in other words, hydroxyl groups might substantially decrease the pressure required, facilitating the phase transition. The recorded Raman spectra [130b] showed that the G band was steeper, and broader and underwent blueshift with an increased pressure, associated with the interlayer coupling **(Figure 10c)**. Such a 2D film was thus a ferromagnetic insulator with a bandgap of 0.6 eV and a magnetic moment of 1 Bohr magneton per unit cell. The formation mechanism was carried out with DFT as well as MD simulations. The interlayer bonds were found to definitely emerge as the initial distance of the two layers was closer than 2.7 Å. The interlayer C-C bond length was 1.66 Å **(Figure 10d, 10e)**. Recently, geometry models of diamondene nanotubes were proposed with two concentric CNTs, expecting the similar toughness of CNTs [136]. Unfortunately, no more details have been released.

Although research reports of diamane-related materials are still relatively rare, we can make some brief comparisons and summaries. As expected from theoretical simulations, phase conversion of bilayer graphene can be caused by surface chemisorption. It can be more effective for FLG when pressure is applied. The chemisorption and pressure induced transversion of graphene layers are two main pathways to the synthesis of diamane related materials. Sometimes

the phase switch might be more effective. Diamane and F-diamane are stable, due to the significant binding energy of functional atoms. Diamane is passivated by Cl and has lower stability as the prediction [131]. Up to now, the synthesis of X-diamanes with other halogen atoms has not been realized. More effort is in demand for the synthesis of stable X-diamane as well as their characterizations and application exploration. The SiC substrate was essential for diamene conversion for offering electrons to saturate the dangling bonds. The Pt (111) substrate is expected to terminate interfacial sp^3 carbon atoms and stabilize the diamondlike few-layer structure through the Pt-C bonds [137]. The effects that the employed substrate devotes to the chemisorption and pressure induced transversion of graphene layers still require to be clarified. The conversion of diamene and diamondene was demonstrated to be reversible. However, it is worth noting that the temporary transfer always occurs regardless of the staking configuration in AA or AB of bilayer graphene. As for multi-layers, a widely accepted opinion is that the underneath layer horizontally displaces [127a, 127c, 131]. Unfortunately, there is no universal conclusion about how the displacement happens.

The electrical flow applied to monitor diamene formation suddenly dropped at the time when phase change, similar phenomena were observed in diamanoïd, and diamondene. An indirect energy gap is 2.8±0.3 eV for h-diamanoïd [127b], the band gap of AB stacking diamane is about 3.9 eV (based on HSE functional) [125]. These results consistently identify that diamane and related materials are semiconductors or insulators. However, there is still no clarity about the value of the band gap [15b].

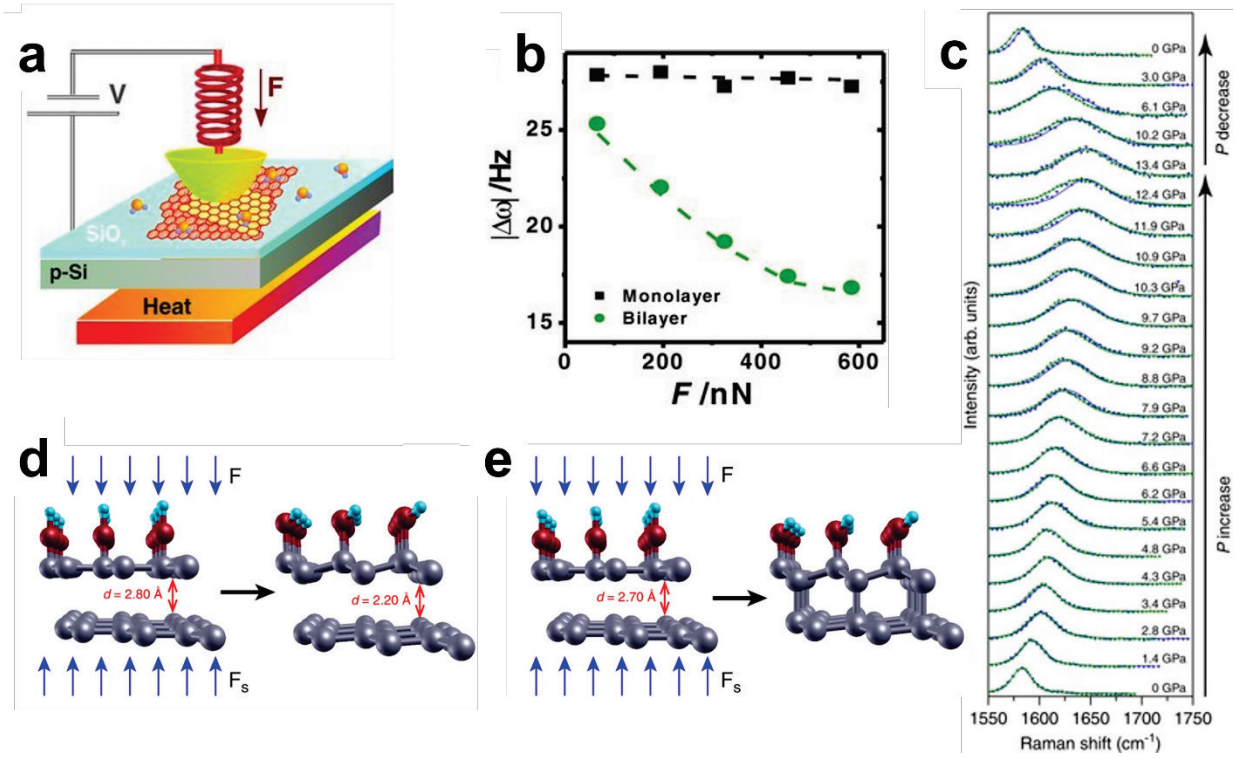

Figure 10. (a) schematic of the experimental setup and procedures; (b) graph of the electric force dependent response versus [130a]; Reproduced with permission.[130a] Copyright 2011, John Wiley and Sons. (c) Raman spectroscopy when bilayer graphene under high pressure using water as the pressure transmission medium (G band broadens and is reversible upon pressure releasing as pressure increasing) of diamondene; (d-e) geometrics for diamondene formation (blue, red, and gray spheres illustrating H, O and C atoms, respectively) [130b]. Reproduced under terms of the CC-BY license.[130b] Copyright 2017, the Authors, published by Springer Nature.

In addition to its wide band gap, diamane has aroused much attention due to its unique mechanical, electronical and thermodynamic properties. Hydrogen atoms that are introduced to its both sides passivate all carbon dangling bonds, leading to a high thermal stability. The formation energy from bilayer graphene is -13.66 or -3.97 eV for AB or AA staking, respectively. It indicates that diamane is stable from the thermodynamic aspect [138]. Moreover, the in-plane Young's modulus was about 1 TGPa. It is close to that of a bulk diamond and related to the staking way, direction (zigzag or armchair direction) and temperature. The shear modulus was 226 J m^{-2} [128c, 129a]. Furthermore, the in-plane elastic constants were comparable to that of bulk diamond, exhibiting a remarkably high resistance to in-plane plastic deformation [128c]. In addition, its high bending stiffness was around 3600 eV Å [139]. Its high natural frequency and a larger quality factor (Q-factor) were on the order of 10^5, processing extraordinary vibrational characteristics [140]. Diamane processed a thermal conductivity of 1960 and 2240 W m^{-1} K^{-1} at

300 K for AB staking and AA staking, respectively. They were mainly contributed by the acoustic out-of-plane phonon modes and were superior to most 2D materials, MoS_2, hexagonal boron-nitride, or phosphorene [141].

Although the research on diamane and diamane-related nanomaterials is mostly on the theoretical stage, they have shown great potential for many applications such as in optoelectronics [129a], nanoelectronics [141], spintronics [140] or as ultra-sensitive resonator-based sensors [128g]. For the super stiffness of diamene, it can act as ultra-hard and ultra-light thermally conductive coatings to help the SiC substrate to enhance mechanical properties [129d]. One point similar to another theoretical diamond material-diamond nanothread is that diamane reinforces the tensile properties of polymer nanocomposites-PMMA. The PMMA nanocomposites exhibited much better tensile performance when the diamane fillers were uniformly aligned along the in-plane direction of diamane [142]. Diamane is also a promising candidate for constructing spiral structures with a high gravimetric energy density of about 564 Wh kg^{-1} [143].

4. 3D diamond nanostructures

Traditional bottom-up overgrowth of 3D scaffolds and top-down etching of thick diamond films are widely reported approaches to produce 3D diamond nanostructures. The variation of experimental parameters adjusts the morphology, compositions, and finally features of these 3D diamond nanostructures.

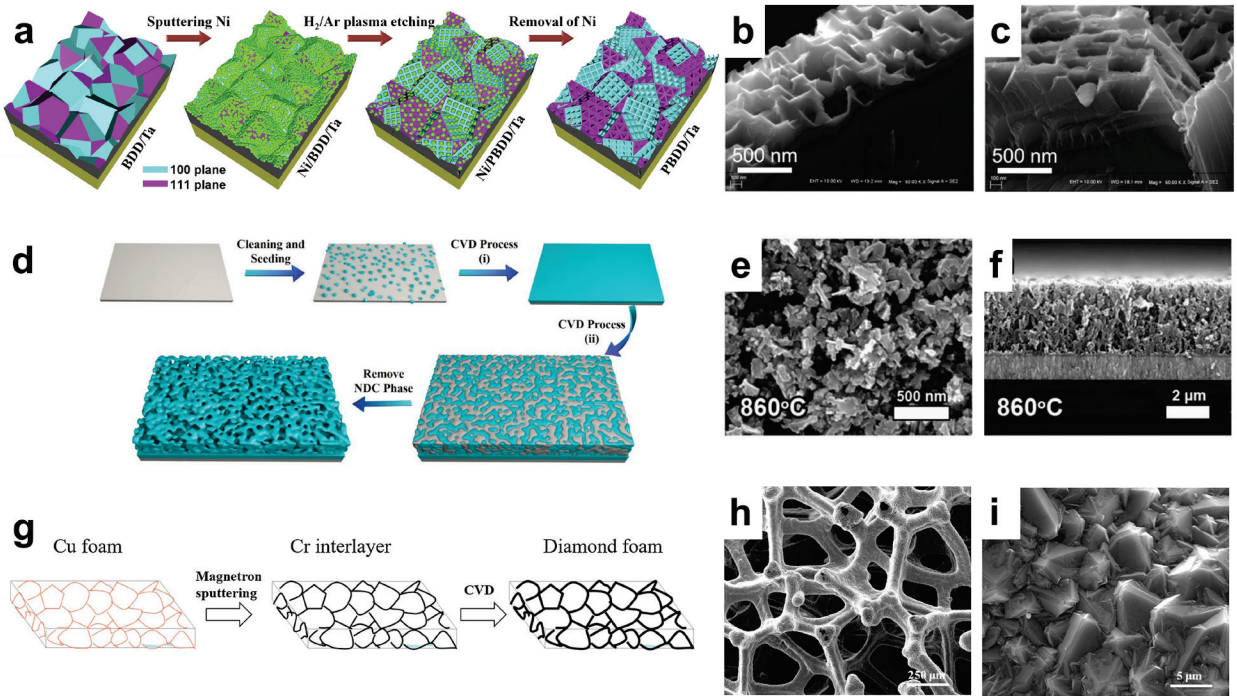

Figure 11. (a-c) (a) schematic of the synthesis of porous diamond structure through etching with, Ni particles acted as catalyzer; SEM images of (111) planes (b) and (100) planes (c) after etching[12c]; Reproduced with permission.[12c] Copyright 2018, Elsevier Ltd. (d-f) (d) schematic of the synthesis of porous diamond structure on SiC substrate; SEM images of porous BDD films from top view (e) and front view (f) [144]; Reproduced with permission.[144] Copyright 2022, Elsevier Ltd. (g-i) (g) schematic of the synthesis of porous diamond structure on Cu foam substrate; SEM images of diamond foam from lower magnifications (h) to high magnifications (i) [145]; Reproduced with permission.[145] Copyright 2019, Elsevier Ltd.

4.1. Top-down etching methods

The top-down etching methods mainly include dry etching [9, 13, 146], wet etching [11], and metal catalytic conversion [10, 12, 147]. The Dry etching method covers electron beam-induced etching (EBIE) [13, 146a], plasma etching [9], and molten salt etching [146b]. The EBIE is a direct-write lithography technique where an electron beam is used to etch materials through reactions that involve surface-adsorbed precursor molecules. When different electron beams are applied, the etching effect is different. For example, anisotropic etching happened when pure H_2 was applied. In this case, the etching rate was low, resulting in topographic surface patterns with symmetries. On the contrary, oxygen gave rise to rapid, isotropic etching. The sponge-like surface textures were seen at the etch pit [13].

The main feature of a wet etching method is the introduction of water vapor into an etching

reaction chamber. Within water vapor, the metal catalyst film is firstly oxidated. When the carbon atoms are moved from the diamond to the metal-diamond interface and then dissolved in the metal film, they react with O in the metal film, leading to the formation of CO gas. As CO partial pressure continues to increase, more stable forms after the reaction between CO and vapor. This kind of reaction mechanism results in a constant carbon concentration gradient from the diamond to the metal catalyst layer and then to the free space. When CO_2 is carried away from the reaction chamber, a constant rate of dissolution of the diamond happens, achieving the goal of catalytic etching [11b].

A more commonly used etching method is the catalytic phase transformation of metals such as Ni [10b, 12b, 12c, 13, 147b, 147d, 148] **(Figure 11a)**, Fe [10a, 12a], Cu [147c] and their complex (mainly Ni particles). The etching principle is demonstrated as follows. On the metal-diamond interface, carbon is decomposed in a perpendicular orientation with respect to the surface of the diamond [147d] and diffused to the interface. If the metal catalyst is of strong carbon solubility, carbon diffuses into the gas phase through the reaction of the catalyst with H to form methane. The gasification process controls the reaction rate of the entire catalytic etching. If the carbon solubility into the metal catalyst is low, carbon is gradually deposited on the interface and formed a layer of graphite to hinder the more migration. The formation rate of this layer determines the size of the etching hole. Namely, when the carbon layer on the metal nanoparticle surface is saturated, the catalytic etching stops and the hole size is held [10, 12a, 147a, 147c]. It is also worth noting that the catalytic etching of polycrystalline diamond often shows anisotropy. The etching primarily occurred on the [111] plane to get a triangular pit **(Figure 11b)**, then carried out on the [100] plane, resulting in the appearance of rectangular nanoholes **(Figure 11c)**. The reason behind this is that the surface Gibbs free energy of the [100] plane is higher than that of the [111] plane. The [111] plane has a double close-packed crystal structure, although the interactions between the two planes in close-packed double planes is strong, the interactions between two close-packed double planes are weak. Both reasons determine that the diamond [111] plane is easier to be etched. The difference in the shape of the pits is related to the arrangement of carbon on two different crystal surfaces [12c, 147b]. Another interesting thing is that the [111] plane of the BDD is not easy to be etched. This is because there is more B atom doping on the [111] plane, leading to much higher B-C bond energy inside BDD than the C-C bond energy. The etching of the BDD thus always occurs firstly on the diamond [100] plane [9b]. The anisotropic etching is

not a theorem. Different experimental conditions resulted in different diamond surface structures.

4.2. Bottom-up overgrowth methods

Many attempts have been made to overgrow diamond film on 3D structures, such as clustered SiO_2 microspheres template [149], wire-like SiO_2, Ti template spin [150], porous TiO_2 layer [151], 3D network metal foam [6a, 145], and organic polymer [152]. Meanwhile, the deposition of diamond films on template-free diamond-SiC **(Figure 11d)** [153] and diamond-nanodiamond particles [144, 154] has been reported, where some composite phases were selectively etched away in the later step by post-acid removement **(Figure 11e, 11f)**. The first method may require multiple-times deposition, like flipping the substrate to evenly deposit diamond films on all aspects, and thus lacks the composition of nanocrystals. The morphology of the composite is completely determined by the substrate. The template-free deposition method is more flexible in adjusting the synthesis parameters to obtain a high-quality diamond film, which possesses a 3D interconnected porous structure and tunable pore size **(Figure 11g, 11h, 11i)** [154]. Another "template-free" method [155] is to employ diamond seeds as the template of a porous structure. This template, namely diamond nanoparticle re-agglomeration was formed by repeatedly inserting the substrate into diamond seed suspension, followed by the traditional CVD diamond growth to consolidate randomly distributed diamond nanoparticles.

Vertically arranged, maze-like diamond-graphite heterojunction nanowalls have been obtained by means of a bottom-up overgrowth approach. Diamond-graphite material has a core-shell structure. It is made of diamond as the core, surrounded by a graphite layer as the shell. When the external graphite layer stabilizes, it hinders the continuing growth of diamond. The composite structure is arranged vertically on the substrate like carbon nanowalls. When viewed from the top, it presents a disordered maze shape. In order to obtain the diamond-graphite composite, experimental conditions were adjusted from two main tactics: the increase of the methane concentration [156] or the introduction of nitrogen gas [157]. A well-accepted theory predicted that the orientation of diamond crystals is determined by the concentration of CH_3 and C_2 radical groups in the reaction chamber. Since the CH_3 radicals facilitate the growth of the [111] plane, while the C_2 radicals favor the growth of [100] planes. When the methane concentration increases, a change of the [111] domain into the [100] domain occurs when more C_2 radicals exist. However, an even higher C_2/CH_3 fraction is accounted for the drastic re-nucleation at grain

boundaries. Microcrystalline diamond will rupture to nanocrystalline. Meanwhile, the formation rate of the sp^2 carbon phase is higher because the atomic hydrogen is not able to totally etch them away, resulting in the formation of diamond/graphite nanostructure. The CH species stuck to these diamond grains creates a hydrocarbon layer surrounding diamond grains. This makes the active C_2 species impossible to directly contact with the diamond core. As a result, more new diamond clusters emerge, instead of increasing the size of the present diamond clusters. In a range of methane proportion between 0 to 12%, the more the methane volume ratio became, the thicker and larger the graphite phase was [158]. What's more, diamond elongated growth happened as a result of C_2 species as the dominant. A high microwave power and a high chamber pressure are also the keys to the nanocomposite film formation [159]. However, excessive methane concentration might inhibit the formation of diamond stems. If nitrogen is introduced, the CN species preferentially adheres to some lattice planes of nanodiamond clusters for the low bond energy, then enhancing the attachment of active carbon or C_2 species onto these lattice planes, leading to more second nucleation as well as thicker graphite shell. The CN species preferentially adheres on the definite faces, determining anisotropic and high-aspect-ratio growth. Moreover, a transversion from wall-like to more needle-like branching morphology happened with an increase of N_2 addition. Such a transversion to an acicular shape needs a high temperature of ~ 700 °C as the formation of CN requires a high activation energy [157b, 160]. The application of low-cost organic matter butylamine as the sole carbon and nitrogen source was another solution to synthesize vertical composite films. In addition to methane and nitrogen, B_2H_6 was believed to be mainly responsible for the developed morphology. The BH_x specials replaced partially the CN molecules at the definite edges, causing re-nucleation expanded length of nanowalls [161].

The vertically and randomly arranged diamond/graphite nanostructures owned an inner diamond nanoplatelet and a highly conducting graphite layer as the shell. They thus exhibited improved structural and mechanical stability, large specific surfaces, and great electrical conductivity. These features significantly extended their applications, especially in the fields of electrochemical sensing and catalysis [162], energy storage and conversion [160, 163], surface-enhanced Raman scattering [164], as well as electron field emission [156b, 157b, 161c, 162d, 165]. For example, their favorable conductivity mainly originated from the graphite out layer, while their low background current and wide potential window were resulted from the diamond core [159a, 162b, 162c, 162e]. The stability and electrochemical merits of diamond stem, plus with conductivity

contributed by graphite, made this complex suitable for the assembly of supercapacitors [157a, 163, 166]. The power density and energy density of the diamond-graphite composite grown on the flexible carbon cloth substrate were 6.3 μW cm^{-2} and 3.7 μWh cm^{-2} for an electrical double layer capacitor (EDLC), respectively [166b]. An effective enhancement of charge-trapping properties was observed after hydrogen plasma etching, which was believed to be useful in battery applications [163]. Among all mentioned applications, the performance of diamond-graphite complex in electron field emission (EFE) was mostly concerned, which was better than that of a polycrystalline diamond film. The reasons for advanced performance were devoted from special surface morphology and increased conductivity of these diamond composites. The uniform, sharp, and dense protrusions on the film sur-face greatly improves the field emission performance [156b, 165b]. From this point of view, all these merits come from the graphite shells. Note that the EFE efficiency was always unsatisfactory, due to its poor stability and short life time. It was jigsaw-like, compensated by the external stability of the diamond [156b, 161c]. It was demonstrated with a low turn-on field, a high emission current density, a large field enhancement factor, and prominently high lifetime stability in electron field emission (EFE) applications. For example, a repeated diamond deposition on the hybrid showed much better EFE behavior: a low turn-on potential (E_o) of 4.3 V μm^{-1}, a high current density (J_e V μm^{-1}) of 20.81 mA cm^{-1} [161c, 165a].

4.3. High temperature high pressure methods

High temperature and high pressure is one of the most effective ways to achieve the transformation from graphite to diamond phase. As mentioned earlier, both diamond nanothreads and diamanes were achieved in harsh experimental environments. The same method is also applicable to the preparation of new three-dimensional diamond materials, such as nanotwined diamond.

Diamond is the hardest known natural mineral. The hardness of single-crystalline cubic diamond is as high as 100 GPa. In industry, diamond has been widely used as the cutting and grinding tool, or to build up diamond anvil cell in laboratory. But science has never stopped pursuing artificial materials with higher hardness, originating from the endless pursuit of better performance of man-made, such as the artificial polycrystalline diamond. The Knoop hardness of man-made polycrystalline with grain size of 10-30 nm is 110-140 GPa, and the Vicker hardness of nanocrystalline diamond is 167 GPa [167]. What could be concluded is as the grain size

decreasing, the mechanical properties enhanced, which was well known as Hall-Petch effect [168]. This is because as the concentration of grain boundaries rising, the grain boundaries in polycrystalline impede the nucleation and the dislocation glide to resist the shape deformation [169]. But this kind of trend of grain particles is not endless. Firstly, the high excess energy of grain boundaries and the synthesis temperature would promote the grain growth, resulting the further decreasing the grain size of great technical challenge. secondly, softening instead of hardening would happen when the grain size decreases below a certain threshold (about 10 nm), according to the reverse Hall-Petch effect. Poorly sintered grain boundaries or sliding motions at the boundaries becomes significant [170]. In theory, further enhancement of hardness by reducing grains size could be achieved in nanotwined structures. Twins were a type of planar defect produced via both phase transformation and deformation [171]. It is widely accepted that the twin boundaries (TBs) played similar role to grain boundaries. What's more, the twin boundaries exhibit lower excess energy than grain ones. Both make the stable existence of smaller twin size possible [172].

In 2014, nanotwined diamond (nt-diamond) was firstly reported [173]. Onion carbon was picked as the precursor, then transferred into nt-diamond through the martensitic transformation after a high pressure and high temperature (HPHT) process **(Figure 12a)** [170b, 173]. The sp^2 carbon atoms in onion-structured precursors puckered into carbon bilayers and linked into sp^3 bonded carbon, with C-C bonds forming between neighboring bilayers [174]. Pure and transparent product was recovered from an 18-25 GPa and 1850-2000 ℃ treatment **(Figure 12b, 12c)** [173]. The stacking sequence of carbon bilayer was exclusively of 3C type [174]. The sample changed to black and opaque, which was identified later as composite of nt-diamond and other carbon phase, under lower pressure and lower temperature [173]. The average twin thickness (λ) was 5-8 nm, which was mainly determined by pressure and reached minimum at 20 GPa [171, 173]. The turnover from carbon onion to nt-diamond combined with two processes. The first was transformation and growth of diamond from precursors. The value of λ decreased monotonically with increasing synthesis pressure. In the second process of mechanical twinning due to plastic deformation, λ could be further reduced. The amplitude of the deviatoric stress was expected to increase with synthesis pressure owing to the increased elastic anisotropy of diamond. Once the deviatoric stress level exceeded a certain threshold, twin-producing glide-set dislocations ceased to be the dominant deformation mechanism, and λ could not be further reduced. This threshold stress

appeared to be reached at a synthesis pressure between 20 and 25 GPa [171]. Obvious changes of XRD patterns [173] and Raman spectra **(Figure 12d)** [167] validated transformation from carbon onion. Only diffraction and vibration peaks which belonged to cubic diamond exhibited in XRD and Raman characterization, respectively. Lamellar {111} nanotwins were present in TEM images [173]. Under similar synthesis conditions, the transition from multiwalled carbon nanotube (MWCNT) films to nanotwin bundles also made success [175]. Preferentially oriented diamond nanotwin bundles succeeded structure from superaligned MWCNT films. These nanotwin bundles had an average twin thickness of 2.9 nm, which was closely related to the small transverse section of MWCNTs. The main difference between nt-diamond and nanotwin bundles was the TBs in nt-diamond was interwove, but the preferentially oriented nanotwins lay in nanotwin bundles. The microstructure divergence led to tuning of mechanical properties, which would be discussed below.

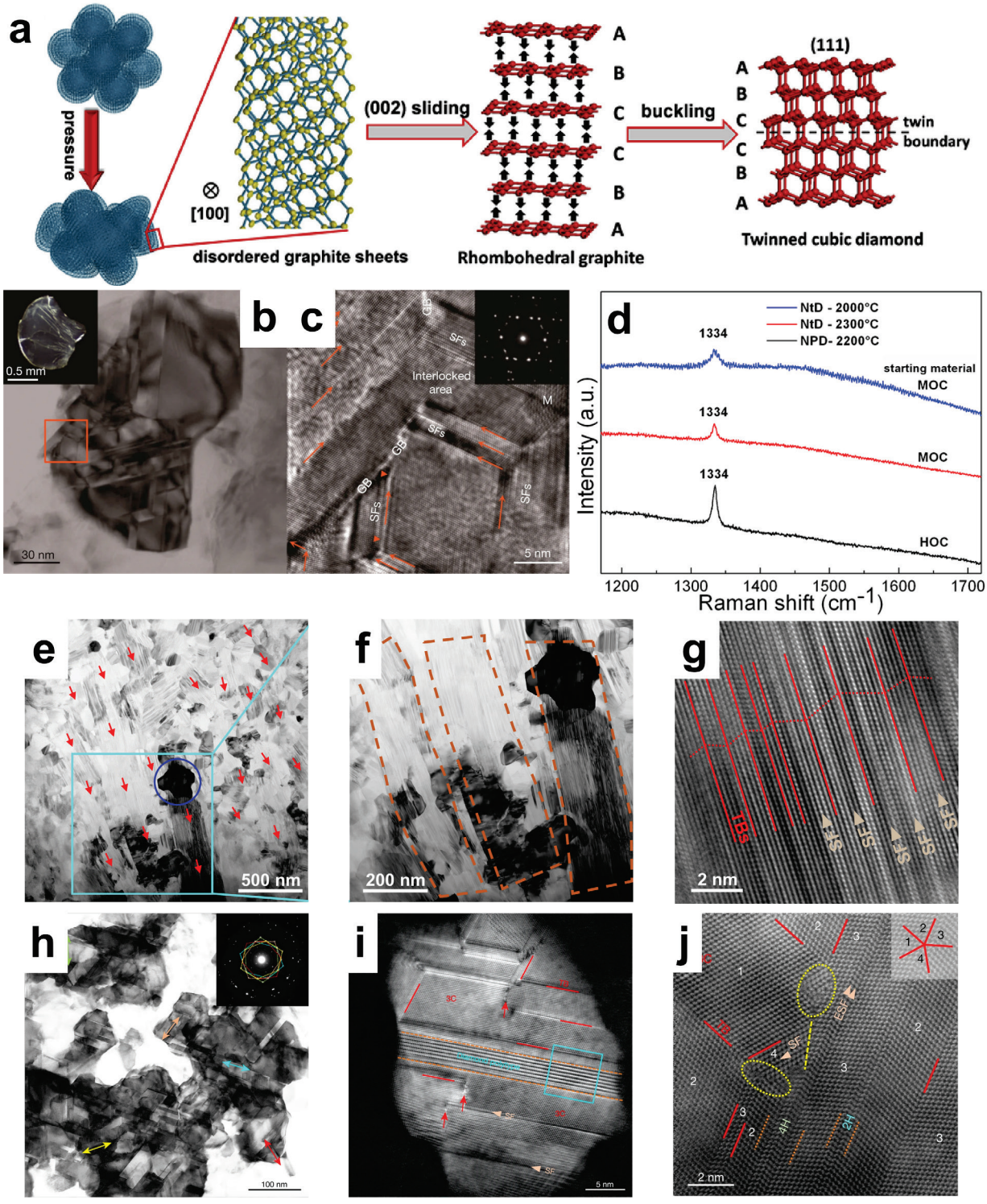

Figure 12. (a) schematic of the synthesis transformation from onion carbon to cubic nt-diamond via a martensitic process at HPHT [170b]; Reproduced with permission.[170b] Copyright 2018, Elsevier Ltd. (b-c) (b) TEM image of nt-diamond, inset: photograph of the transparent sample, diameter was about 1 mm; (c) HRTEM image of intersecting nt-diamond, twin boundaries (TBs)

were marked with red arrows, inset: SAED pattern of nt-diamond [173]; Reproduced with permission.[173] Copyright 2014, Springer Nature. (d) Raman spectra of nt-diamond [167]; Reproduced with permission.[167] Copyright 2017, Elsevier Ltd. (e-g) (e) BF-STEM image of the synthetic diamond with a bundle-like microstructure; (f) BF-STEM image from the cyan-boxed region in (e), clearly revealing micrometer-sized preferentially oriented nanotwin bundles running across multiple diamond nanograins; (g) HRTEM image of the nanotwin bundles [175]; Reproduced with permission.[175] Copyright 2021, Nature. (h-j) (h) low-magnification bright-field STEM image showing interlocked grains constituted of nt-diamond composite, inset: the corresponding SAED pattern with an apparent fivefold symmetry due to multiple twinning in the interlocked grains; (i) high-magnification ADF-STEM image of a grain with nanotwins and coherently embedded diamond polytype domains, TBs were marked with red lines; (j) HAADF-STEM images of nt-diamond composite, showing TBs, stacking fault, extrinsic stacking fault and diamond polytypes [174]; Reproduced with permission.[174] Copyright 2020, Nature.

The most attention-grabbing feature of nt-diamond was the unprecedentedly high hardness. The Vickers and Knoop hardness values were 175-203 and 168-196 GPa, respectively, which was about twice the commonly single-crystal diamond. Not only that, the fracture toughness values of nt-diamond ranged from 9.7 to 14.8 MPa $m^{0.5}$ under high loads. The onset oxidation temperature of nt-diamond was about 980 ℃, which was much higher than that of natural diamond (about 770 ℃) [173]. Inspired by the extraordinarily high hardness in nt-diamond, as well as the trade-off between hardness and toughness, the improved thermal stability, the reason how and why these phenomena happened were waiting for suitable explanation urgently.

First and of most importance is the colossal hardness, exceeded than all previously reported materials. The blocking effect of TBs on dislocation slips was believed to play a crucial role in producing giant hardness [167, 171, 173, 176]. And TBs originated from the stacking faults than other various defects in the carbon onion precursors [167, 170b, 177]. The high-energy metastable carbon onion was consisted of several concentric graphitic shells. This kind of structure determined the high concentration of puckered layers and stacking faults [170b, 173, 178]. The relative (002) sliding motions within the onion-like structures were restricted which induced an accumulation of stress along the shear direction. The release of the stress re-aligns the C-C bonds at the boundary leaded to the formation of {111} twinned structures [170b]. The deeper insights to elucidate the mechanism behind the unusually high hardness remained elusive. At the beginning, Tian's team draw an conclusion that both the Hall-Petch effect and quantum confinement effect contributing to the hardness [171]. Another kind of opinion was the robust mechanism for bond realignment from a TB-induced stress concentration, producing a giant indentation strain stiffening in nt-

diamond [177]. Later they offered more detailed explanation based on the investigation of the interactions between dislocations and twin planes in nt-diamond [179]. There were two factors, the high lattice frictional stress due to the strong sp^3 C-C bonding in diamond, and the high athermal stress due to the Hall-Petch effect. Both factors stemmed from the low activation volumes and high activation energy for dislocation nucleation and propagation in diamond twin planes. The mechanical properties of nt-diamond was isotropic, originating from randomly oriented equiaxed nanotwins. In contrast, the hardness of diamond nanotwin bundles **(Figure 12e, 12f, 12g)** shew extreme anisotropy [175]. The maximum Knoop hardness reached as high as 241 GPa with the long axis of the indenter perpendicular to nanotwin bundles, while 138 GPa with the long axis parallel to nanotwin bundles. Molecular dynamics simulations attributed that the dense twin boundaries along the perpendicular direction to bundles significantly hindered the motion of dislocations under indention. While such a resistance was much weaker in the direction along the nanotwin bundles.

In addition to the extraordinary hardness of nt-diamond, the reverse Hall-Petch relation was inapplicable for the nt-diamond and diamond nanotwin bundles unexpectedly [178, 180]. Results from molecular dynamics and first-principles calculations indicated that the mechanically stable TBs was again the main reason. In nt-diamond, shuffle-set dislocations propagation remain dominated the plastic deformation. But TBs resisted their propagation across twin domains and inhibited the reverse Hall-Petch relation [180]. Theoretically feasible was the hardness of nt-diamond increasing with the decreasing of TB thickness (λ), or introducing more TBs into the microstructure [171, 176, 181]. For example, the novel intersectional nt-diamond (int-diamond), with coexist and interwove two kinds of TBs, was designed to confirm the hypothesis [181]. Calculations based on the Sachs model proved that the int-diamond was much harder than nt-diamond. The additional hardness was attributed to the intersectional TBs blocking dislocations motions and resulting in the increased critical resolved shear stress.

Before, the toughness of diamond was sacrificed with the demand of higher hardness. Improving toughness and hardness simultaneously was challenging because of the intrinsic brittleness of diamond. Fortunately, this old paradigm was broken by nt-diamond. The gliding of dislocations along densely distributed twin boundaries enhanced fracture toughness [169c, 182]. What's more, a higher fracture toughness value of 26.6 MPa $m^{0.5}$ without sacrificing hardness was verified in the aforementioned black and opaque product [173-174]. This kind of product was

consisted of main nt-diamond and thin slices of metastable carbon phase **(Figure 12h, 12i, 12j)**. The uncertain carbon phase was actually several non-3C (cubic) diamond. Totally different with diamond crystal, M-diamond had a monoclinic structure with lattice parameters of a=0.436 nm, b=0.251 nm, c=1.248nm and β=90.9º [173]. Speculating about the synthesis mechanism of the non-3C polytypes was the driving force under low pressure was not sufficient to transfer partial onion carbon to stable 3C structure. The non-3C diamond polytypes were coherently embedded in nt-diamond mosaic-structures. The composite hierarchically assembled with coherently interfaced diamond polytypes, interwoven nanotwins and interlocked nanograins played an essential role in toughness. When fracture occurred, a crack propagated through diamond nanotwins along {111} planes, via a zigzag path. As the crack encountered regions of non-3C polytypes, its propagation was diffused into sinuous fractures, with local transformation into 3C diamond near the fracture surfaces. Both processes dissipated strain energy, thereby enhancing toughness. There was another peculiarity discovery from the single-edge notched beam (SENB) tests, that crack in nt-diamond composite healed to a considerable extent. Reasonable explanation about the partial self-healing would be re-bonding of some dangling carbon bonds on two opposite fractured surfaces near the crack tip after unloading [174]. Large-scale molecular dynamics (MD) simulation using the large-scale atomic/molecular massively parallel simulator (LAMMPS) package was performed to analysis underlying mechanism behind the crack healing [183]. The simulations showed that the crack healing occurred during unloading, and its extent was associated with whether the fracture surfaces were clean. In detail, full crack healing could finish for nt-diamond and 4H diamond (kind of non-3C polytypes). Because the fracture surfaces of both samples were clean. However, for other polytype diamonds and nt-diamond composites, the crack only partially healed. The reason was there were disordered atoms clusters or atomic chains on fracture surfaces when the crack tip tended to close .

The nt-diamond was a promising tool material for next generation high-precision, high efficiency cutting. Ultrahigh hardness is definitely a surprising merit of nt-diamond, but also becomes a stumbling block in its potential use as the tool, especially in ultra-precision cutting of hard-to-machine materials [184]. Before it's actually put into production, how to fabricate nt-diamond is waiting to be resolved. Luckly, both traditional mechanical polishing [184a] and femtosecond pulsed laser milling technique [184b] worked. Under the synergistic effect of mechanical loading and Fe nanoparticles catalyzing, nt-diamond was transferred to a hard sp^2-sp^3

mixed amorphous carbon. Due to the isotropy and the binder-free characteristics of nt-D, the phase transition and the subsequent removal of formed amorphous carbon were uninterrupted. The surface of the amorphous carbon layer and the interface between amorphous carbon and nt-D were both smooth after polishing. The final surface roughness R_a was 0.29 nm [184a]. Compared with the conventional mechanical methods, the femtosecond pulsed laser milling technique was with higher efficiency, and possibility to shape nt-diamond related cutting tool. The cubic diamond within nt-diamond was transformed into amorphization directly. The dewetting of a certain amount of diamond grain boundaries led to the formation of the falling-off pits of the nt-D grain clusters, which influenced the surface roughness. By upgrading milling with trochoidal trajectory, the penetration depth of teat and the depth of the falling-off pits were apparently reduced. The average surface roughness of this high-precise nt-diamond tool was 33 nm, and an edge radius was 0.47 μm [184b]. The nt-diamond fabricated by the pulsed femtosecond-laser was already used as the *in-situ* TEM indenter to test phenomenon and mechanism of aforementioned elastic deformation of needle-like diamond samples [47]. At the meantime, nt-diamond pillars made with length about 361 nm, served as the object under testing. The corresponding selected area electron diffraction (SAED) pattern containing the (111), (022), and (113) diffraction rings of the diamond further demonstrated the polycrystalline feature of the nt-diamond nanopillar. And permanent plastic deformation occurred, about 5.8%.

5. Conclusions and Outlooks

This review summarizes the research progress and achievements in the past decades about the synthesis and applications of diamond nanomaterials with different dimensions. For decades, the polycrystalline diamond synthesized by the method gives full play to the properties of diamond. For example, the enlarged surface area of a 3D porous diamond structures, in combination with its high conductivity and chemical stability endow it suitable for electrochemical sensing and electron field emission applications. The 3D diamond nanomaterials also show great potential in terms of energy storage and conversion, due to its wide potential window and good chemical inert. Diamond nanoneedles can not only finish antibiosis easily with their sharp tips and strong robustness but also biopsy in cylindrical shape for their biocompatibility from another angle. Moreover, surprising ultra-elasticity was found on the diamond nanoneedle and microbridge structures, which provide important support for the potential progress of diamond materials in

the field of deep elastic strain engineering for photonics, electronics, and quantum information technology. And the unpresented ultrahigh hardness of nt-diamond broke through the limits of all previous materials.

For these diamond nanostructures, it is still necessary to consider the design of diamond material structures by using different substrates or patterning on the surface of a diamond film. This is already a relatively mature technology. Different from that, direct phase transformation, which can be chemically or pressure induced, from inorganic graphene or organic aromatic compound is a new technology. Two approaches are already available: i) the conversion of benzene and its derivatives to obtain diamond nanothreads and ii) the interlayer bonding of graphene to obtain diamanes. Although diamond nanothreads and diamanes are far away from real applications, their extraordinary mechanical properties (e.g., high strength and stiffness), as well as high thermal stability have already been investigated theoretically. The transfer behavior (namely from brittle to ductile) and high thermal conductivity will be very promising for many applications. Again, this kind of research is still in the theoretical stage, where more effort and energy are required.

So far, the surprising elasticity of diamond nanoneedles has been discovered. This elasticity is based on the elasticity of defects in the small volume diamond nanostructures and to the relatively smooth surfaces compared with those of microscale and larger specimens. How they can play a role in practice still needs to be considered, and it is also uncertain whether it is possible to extend to larger-size nanostructures. Comparatively speaking, the synthesis progress of diamond nanothreads is faster and more comprehensive than that of diamanes. However, for diamond nanothreads, whether it is benzene as the precursor or many other precursors that have appeared, the synthesis reaction steps and precise molecular structure are still unclear. Based on the progress in the synthesis of nanothreads, it is necessary to determine the structure judgment and look towards practical applications. For diamanes, only diamane and F-diamene have been successfully prepared, indicating that chemical adsorption conversion only affects the bilayer structure. How to achieve the conversion of multi-layer structures or under other surface terminations, what the role of substrate materials is in the reaction still pend. The synthesis may still be a topic in the later stage.

In summary, diamond nanostructures at different dimensions have been extensively investigated, ranging from their synthesis, characterization, and applications. It is hoped that this

review article will attract more researchers from different fields to work more on diamond nanostructures, especially on the experimental synthesis, characterization, and applications of diamond nanothreads, diamanes, and nt-diamond in the upcoming years.

Acknowledgements

Y.L. thanks the China Scholarship Council (CSC) for the financial support (No. 202108420055). N.Y. thanks the financial support from the Deutsche Forschungsgemein-schaft (DFG, German Research Foundation) under the Project No. 457444676.

Received: ( )

Revised: ( )

Published online: ( )

6. References

[1] a) S. Yu, S. Liu, X. Jiang, N. Yang, *Carbon* **2022**, 200, 517; b) N. Yang, X. Jiang, *Acc. Chem. Res.* **2023**, 56, 117; c) N. Yang, S. Yu, J. V. Macpherson, Y. Einaga, H. Zhao, G. Zhao, G. M. Swain, X. Jiang, *Chem. Soc. Rev.* **2019**, 48, 157.

[2] a) W. Long, H. Li, B. Yang, N. Huang, L. Liu, Z. Gai, X. Jiang, *J. Mater. Sci. Technol.* **2020**, 48, 1; b) D. Aradilla, F. Gao, G. Lewes-Malandrakis, W. Müller-Sebert, P. Gentile, S. Pouget, C. E. Nebel, G. Bidan, *Electrochim. Acta* **2017**, 242, 173.

[3] a) Z. Jian, M. Heide, N. Yang, C. Engelhard, X. Jiang, *Carbon* **2021**, 175, 36; b) M. A. Hejazi, W. Tong, A. Stacey, A. Soto-Breceda, M. R. Ibbotson, M. Yunzab, M. I. Maturana, A. Almasi, Y. J. Jung, S. Sun, H. Meffin, J. Fang, M. E. M. Stamp, K. Ganesan, K. Fox, A. Rifai, A. Nadarajah, S. Falahatdoost, S. Prawer, N. V. Apollo, D. J. Garrett, *Biomaterials* **2020**, 230; c) J. Millán-Barba, H. Bakkali, F. Lloret, M. Gutiérrez, R. Guzmán de Villoria, M. Domínguez, K. Haenen, D. Araujo, *Appl. Surf. Sci.* **2023**, 615.

[4] J. Zhang, Z. Zhao, Z. Zhang, L. Guo, L. Xu, P. Sun, M. Wang, M. Gao, Y. Li, D. Li, R. Boukherroub, *J. Colloid Interface Sci.* **2023**, 629, 813.

[5] S. Handschuh-Wang, T. Wang, Y. Tang, *Small* **2021**, 17, e2007529.

[6] a) N. Hu, H. Li, Q. Wei, K. Zhou, W. Zhu, L. Zhang, S. Li, W. Ye, Z. Jiao, J. Luo, L. Ma, Q. Yan, C.-T. Lin, *Compos. B. Eng.* **2020**, 200; b) D. Miao, Z. Li, Y. Chen, G. Liu, Z. Deng, Y. Yu, S. Li, K. Zhou, L. Ma, Q. Wei, *Chem. Eng. J.* **2022**, 429.

[7] Z. Jian, N. Yang, M. Vogel, S. Leith, A. Schulte, H. Schönherr, T. Jiao, W. Zhang, J. Müller, B. Butz, X. Jiang, *Adv. Energy Mater.* **2020**, 10.

[8] I. Moraleda, S. Cotillas, J. Llanos, C. Sáez, P. Cañizares, L. Pupunat, M. A. Rodrigo, *J. Electroanal. Chem.* **2019**, 850.

[9] a) D. Shi, L. Liu, Z. Zhai, B. Chen, Z. Lu, C. Zhang, Z. Yuan, M. Zhou, B. Yang, N. Huang, X. Jiang, *J. Mater. Sci. Technol.* **2021**, 86, 1; b) F. Liu, Z. Deng, D. Miao, W. Chen, Y. Wang, K. Zhou, L. Ma, Q. Wei, *J. Environ. Chem. Eng.* **2021**, 9.

[10] a) J. Li, X. Liu, L. Wan, W. Fang, Y. Yan, Y. Li, P. Gao, *Ceram. Int.* **2021**, 47, 35002; b) H. Li, K. Zhou, J. Cao, Q. Wei, C.-T. Lin, S. E. Pei, L. Ma, N. Hu, Y. Guo, Z. Deng, Z. Yu, S. Zeng, W. Yang, L. Meng, *Carbon* **2021**, 171, 16.

[11] a) Z. Ma, Q. Wang, N. Gao, H. Li, *Microchem. J.* **2020**, 157; b) Y. Li, Y. Kim, P. V. Bakharev, W. K. Seong, C. Hyun, D. C. Camacho-Mojica, L. Zhang, B. V. Cunning, T. J. Shin, G. Lee, R. S. Ruoff, *Chem. Mater.* **2022**, 34, 2599.

[12] a) A. Chepurov, V. Sonin, D. Shcheglov, A. Latyshev, E. Filatov, A. Yelisseyev, *Int. J. Refract. Hard. Met.* **2018**, 76, 12; b) Y. Li, H. Li, M. Li, C. Li, D. Sun, B. Yang, *Electrochim. Acta* **2017**, 258, 744; c) X. Li, H. Li, M. Li, C. Li, D. Sun, Y. Lei, B. Yang, *Carbon* **2018**, 129, 543.

[13] J. Bishop, M. Fronzi, C. Elbadawi, V. Nikam, J. Pritchard, J. E. Froch, N. M. H. Duong, M. J. Ford, I. Aharonovich, C. J. Lobo, M. Toth, *ACS Nano* **2018**, 12, 2873.

[14] a) H. Zhan, G. Zhang, V. B. C. Tan, Y. Cheng, J. M. Bell, Y.-W. Zhang, Y. Gu, *Adv. Funct. Mater.* **2016**, 26, 5279; b) H. Zhan, G. Zhang, V. B. Tan, Y. Gu, *Nat. Commun.* **2017**, 8, 14863; c) T. C. Fitzgibbons, M. Guthrie, E. S. Xu, V. H. Crespi, S. K. Davidowski, G. D. Cody, N. Alem, J. V. Badding, *Nat. Mater.* **2015**, 14, 43.

[15] a) F. Lavini, M. Rejhon, E. Riedo, *Nat. Rev. Mater.* **2022**, 7, 814; b) P. B. Sorokin, B. I. Yakobson, *Nano Lett.* **2021**, 21, 5475; c) S. K. Tiwari, R. Pandey, N. Wang, V. Kumar, O. J. Sunday, M. Bystrzejewski, Y. Zhu, Y. K. Mishra, *Adv. Sci.* **2022**, 9; d) L. A. Chernozatonskii, P. B. Sorokin, A. G. Kvashnin, D. G. Kvashnin, *JETP Letters* **2009**, 90, 134.

[16] a) J.-X. Qin, X.-G. Yang, C.-F. Lv, Y.-Z. Li, K.-K. Liu, J.-H. Zang, X. Yang, L. Dong, C.-X. Shan, *Mater. Des.* **2021**, 210; b) L. Basso, M. Cazzanelli, M. Orlandi, A. Miotello, *Applied Sciences* **2020**, 10.

[17] C. Chen, Y. Mei, J. Cui, X. Li, M. Jiang, S. Lu, X. Hu, *Carbon* **2018**, 139, 982.

[18] Vlasov, Il, A. A. Shiryaev, T. Rendler, S. Steinert, S. Y. Lee, D. Antonov, M. Voros, F. Jelezko, A. V. Fisenko, L. F. Semjonova, J. Biskupek, U. Kaiser, O. I. Lebedev, I. Sildos, P. R. Hemmer, V. I. Konov, A. Gali, J. Wrachtrup, *Nat Nanotechnol* **2014**, 9, 54.

[19] B. Rodiek, M. Lopez, H. Hofer, G. Porrovecchio, M. Smid, X.-L. Chu, S. Gotzinger, V. Sandoghdar, S. Lindner, C. Becher, S. Kuck, *Optica* **2017**, 4.

[20] K. Wakui, Y. Yonezu, T. Aoki, M. Takeoka, K. Semba, *Jpn. J. Appl. Phys.* **2017**, 56.

[21] a) X. Peng, J. Chu, L. Wang, S. Duan, P. Feng, *Sens. Actuators B Chem.* **2017**, 241, 383; b) S. Li, C.-H. Li, B.-W. Zhao, Y. Dong, C.-C. Li, X.-D. Chen, Y.-S. Ge, F.-W. Sun, *Chinese Phys. Lett.* **2017**, 34.

[22] X. Peng, Y. Li, S. Duan, J. Chu, P. Feng, *Mater. Lett.* **2020**, 265.

[23] P. Subramanian, S. Kolagatla, S. Szunerits, Y. Coffinier, W. S. Yeap, K. Haenen, R. Boukherroub, A. Schechter, *J. Phys. Chem. C.* **2017**, 121, 3397.

[24] a) C. H. Lee, Y. K. Lim, E. S. Lee, H. J. Lee, H. D. Park, D. S. Lim, *RSC Adv.* **2018**, 8, 11102; b) C.-H. Lee, E.-S. Lee, Y.-K. Lim, K.-H. Park, H.-D. Park, D.-S. Lim, *RSC Adv.* **2017**, 7, 6229.

[25] S.-K. Lee, M.-J. Song, D.-S. Lim, *J. Electroanal. Chem.* **2018**, 820, 140.

[26] a) Y. Gao, S. Okada, *Diam. Relat. Mater.* **2022**, 125; b) F. Marsusi, S. M. Monavari, *Diam. Relat. Mater.* **2020**, 109.

[27] L. Arnoldi, M. Spies, J. Houard, I. Blum, A. Etienne, R. Ismagilov, A. Obraztsov, A. Vella, *Appl. Phys. Lett.* **2018**, 112.

[28] Z. Zhang, Z. M. Hossain, *Nanotechnology* **2020**, 31, 095709.

[29] X. Qu, J. Gu, *RSC Adv.* **2020**, 10, 1243.

[30] a) A. F. Zhou, R. Velazquez, X. Wang, P. X. Feng, *ACS Appl. Mater. Interfaces* **2019**, 11, 38068; b) E. Pacheco, B. Zhou, A. Aldalbahi, A. F. Zhou, P. X. Feng, *Ceram. Int.* **2022**, 48, 3757.

[31] a) G. Hazell, P. W. May, P. Taylor, A. H. Nobbs, C. C. Welch, B. Su, *Biomater. Sci.* **2018**, 6, 1424; b) O. Dunseath, E. J. W. Smith, T. Al-Jeda, J. A. Smith, S. King, P. W. May, A. H. Nobbs, G. Hazell, C. C. Welch, B. Su, *Sci. Rep.* **2019**, 9, 8815.

[32] a) A. M. Alexeev, R. R. Ismagilov, A. N. Obraztsov, *Diam. Relat. Mater.* **2018**, 87, 261; b) J. Lu, B. Yang, B. Yu, H. Li, N. Huang, L. Liu, X. Jiang, *Adv. Opt. Mater.* **2021**, 9.

[33] a) L. Rigutti, L. Venturi, J. Houard, A. Normand, E. P. Silaeva, M. Borz, S. A. Malykhin, A. N. Obraztsov, A. Vella, *Nano Lett.* **2017**, 17, 7401; b) S. A. Malykhin, R. R. Ismagilov, F. T. Tuyakova, E. A. Obraztsova, P. V. Fedotov, A. Ermakova, P. Siyushev, K. G. Katamadze, F. Jelezko, Y. P. Rakovich, A. N. Obraztsov, *Opt. Mater.* **2018**, 75, 49; c) M. Borz, M. H. Mammez, I. Blum, J. Houard, G. Da Costa, F. Delaroche, S. Idlahcen, A. Haboucha, A. Hideur, V. I. Kleshch, A. N. Obraztsov, A. Vella, *Nanoscale* **2019**, 11, 6852; d) V. I. Kleshch, V. Porshyn, A. S. Orekhov, A. S. Orekhov, D. Lützenkirchen-Hecht, A. N. Obraztsov, *Carbon* **2021**, 171, 154; e) L. Golubewa, Y. Padrez, S. Malykhin, T. Kulahava, E. Shamova, I. Timoshchenko, M. Franckevicius, A. Selskis, R. Karpicz, A. Obraztsov, Y. Svirko, P. Kuzhir, *Adv. Opt. Mater.* **2022**, 10; f) S. Malykhin, Y. Mindarava, R. Ismagilov, F. Jelezko, A. Obraztsov, *Diam. Relat. Mater.* **2022**, 125.

[34] Y. Wang, Y. Yang, L. Yan, S. Y. Kwok, W. Li, Z. Wang, X. Zhu, G. Zhu, W. Zhang, X. Chen, P. Shi, *Nat. Commun.* **2014**, 5, 4466.

[35] X. Zhu, M. F. Yuen, L. Yan, Z. Zhang, F. Ai, Y. Yang, P. K. Yu, G. Zhu, W. Zhang, X. Chen, *Adv. Healthc. Mater.* **2016**, 5, 1157.

[36] Y. Wang, Z. Wang, K. Xie, X. Zhao, X. Jiang, B. Chen, Y. Han, Y. Lu, L. Huang, W. Zhang, Y. Yang, P. Shi, *Nano Lett.* **2020**, 20, 5473.

[37] X. Zhao, X. Ji, J. Qu, K. Xie, Z. Wang, P. Fang, Y. Wang, Y. Wan, Y. Yang, W. Zhang, P. Shi, *J. Am. Chem. Soc.* **2022**, 144, 6010.

[38] a) Z. Wang, L. Qi, Y. Yang, M. Lu, K. Xie, X. Zhao, E. H. C. Cheung, L. Qi, Y. Yang, Y. W. X. J. W. Zhang, L. Huang, X. Wang, P. Shi, *Sci. Adv.* **2020**, 6; b) K. Xie, Z. Wang, L. Qi, X. Zhao, Y. Wang, J. Qu, P. Xu, L.

Huang, W. Zhang, Y. Yang, X. Wang, P. Shi, *ACS Nano* **2021**, 15, 4881.
[39] M. Born, K. Huang, M. Lax, *American Journal of Physics* **1955**, 23, 474.
[40] R. H. Telling, C. J. Pickard, M. C. Payne, J. E. Field, *Phys. Rev. Lett.* **2000**, 84, 5160.
[41] Y. Zhang, H. Sun, C. Chen, *Physical Review B* **2006**, 73.
[42] X. Luo, Z. Liu, B. Xu, D. Yu, Y. Tian, H.-T. Wang, J. He, *J. Phys. Chem. C* **2010**, 114, 17851.
[43] A. Banerjee, D. Bernoulli, H. Zhang, M.-F. Yuen, J. Liu, J. Dong, F. Ding, J. Lu, M. Dao, W. Zhang, Y. Lu, S. Suresh, *Science* **2018**, 360, 300.
[44] T. Zhu, J. Li, *Progress in Materials Science* **2010**, 55, 710.
[45] J. Li, Z. Shan, E. Ma, *MRS Bulletin* **2014**, 39, 108.
[46] A. Nie, Y. Bu, P. Li, Y. Zhang, T. Jin, J. Liu, Z. Su, Y. Wang, J. He, Z. Liu, H. Wang, Y. Tian, W. Yang, *Nat. Commun.* **2019**, 10, 5533.
[47] Y. Zhang, Y. Bu, J. Huang, T. Jin, A. Nie, H. Wang, Y. Tian, *Science China Materials* **2020**, 63, 2335.
[48] A. Banerjee, D. Bernoulli, H. Zhang, M.-F. Yuen, J. Liu, J. Dong, F. Ding, J. Lu, M. Dao, Wenjun, Zhang, Y. Lu, S. Suresh, *science* **2018**, 360, 300.
[49] A. Nie, Y. Bu, P. Li, Y. Zhang, T. Jin, J. Liu, Z. Su, Y. Wang, J. He, Z. Liu, H. Wang, Y. Tian, W. Yang, *Nat Commun* **2019**, 10, 5533.
[50] C. Dang, J.-P. Chou, B. Dai, C.-T. Chou, Y. Yang, R. Fan, W. Lin, F. Meng, A. Hu, J. Zhu, Jiecai, Han, A. M. Minor, J. Li, Y. Lu, *science* **2021**, 371, 76.
[51] B. Regan, A. Aghajamali, J. Froech, T. T. Tran, J. Scott, J. Bishop, I. Suarez-Martinez, Y. Liu, J. M. Cairney, N. A. Marks, M. Toth, I. Aharonovich, *Adv. Mater.* **2020**, 32.
[52] C. Dang, J.-P. Chou, B. Dai, C.-T. Chou, Y. Yang, R. Fan, W. Lin, F. Meng, A. Hu, J. Zhu, J. Han, A. M. Minor, J. Li, Y. Lu, *Science* **2021**, 371, 76.
[53] A. Nie, Y. Bu, J. Huang, Y. Shao, Y. Zhang, W. Hu, J. Liu, Y. Wang, B. Xu, Z. Liu, H. Wang, W. Yang, Y. Tian, *Matter* **2020**, 2, 1222.
[54] L. E. Fisher, Y. Yang, M. F. Yuen, W. Zhang, A. H. Nobbs, B. Su, *Biointerphases* **2016**, 11, 011014.
[55] S. Kunuku, K. J. Sankaran, K.-C. Leou, I. N. Lin, *Mater. Res. Express.* **2017**, 4.
[56] a) T. Hao, W. Li, Z. Liu, Y. Sun, L. Jin, J. Li, C. Gu, *Diam. Relat. Mater.* **2017**, 75, 91; b) T. Zhu, Y. Liang, Z. Liu, J. Fu, Y. Wang, G. Shao, D. Zhao, J. Wang, R. Wang, Q. Wei, W. Wang, F. Wen, T. Min, H. Wang, *Coatings* **2020**, 10.
[57] L. Shi, F. Xu, J. Gao, M. Yuen, S. Sun, J. Xu, K. Jia, D. Zuo, *Diam. Relat. Mater.* **2020**, 109.
[58] S.-W. Jeon, J. Lee, H. Jung, S.-W. Han, Y.-W. Cho, Y.-S. Kim, H.-T. Lim, Y. Kim, M. Niethammer, W. C. Lim, J. Song, S. Onoda, T. Ohshima, R. Reuter, A. Denisenko, J. Wrachtrup, S.-Y. Lee, *ACS Photonics* **2020**, 7, 2739.
[59] B. Liu, Y. Zheng, H.-Q. Peng, B. Ji, Y. Yang, Y. Tang, C.-S. Lee, W. Zhang, *ACS Energy Lett.* **2020**, 5, 2590.
[60] D. Shi, N. Huang, L. Liu, B. Yang, Z. Zhai, Y. Wang, Z. Yuan, H. Li, Z. Gai, X. Jiang, *Appl. Surf. Sci.* **2020**, 512.
[61] a) T. Zhi, T. Tao, B. Liu, X. Wang, W. Hu, K. Chen, Z. Xie, R. Zhang, *Diam. Relat. Mater.* **2021**, 119; b) A. Schmidt, J. Bernardoff, K. Singer, J. P. Reithmaier, C. Popov, *Phys. Status Solidi A* **2019**, 216; c) K. J. Sankaran, C. J. Yeh, S. Drijkoningen, P. Pobedinskas, M. K. Van Bael, K. C. Leou, I. N. Lin, K. Haenen, *Nanotechnology* **2017**, 28, 065701; d) R. Ramaneti, K. J. Sankaran, S. Korneychuk, C. J. Yeh, G. Degutis, K. C. Leou, J. Verbeeck, M. K. Van Bael, I. N. Lin, K. Haenen, *APL Mater.* **2017**, 5; e) S. Deshmukh, K. J. Sankaran, K. Srinivasu, S. Korneychuk, D. Banerjee, A. Barman, G. Bhattacharya, D. M. Phase, M. Gupta, J. Verbeeck, K. C. Leou, I. N. Lin, K. Haenen, S. S. Roy, *Diam. Relat. Mater.* **2018**, 83, 118; f) S. Deshmukh, K. J. Sankaran, S. Korneychuk, J. Verbeeck, J. McLaughlin, K. Haenen, S. S. Roy, *Electrochim. Acta* **2018**, 283, 1871; g) G. Bhattacharya, K. Jothiramalingam Sankaran, S. B. Srivastava, J. P. Thomas, S. Deshmukh, P. Pobedinskas, S. P. Singh, K. T. Leung, M. K. Van Bael, K. Haenen, S. S.

Roy, *Electrochim. Acta* **2017**, 246, 68.
[62] a) R. E. Roman, K. Kwan, S. W. Cranford, *Nano Lett.* **2015**, 15, 1585; b) H. Zhan, G. Zhang, V. B. Tan, Y. Cheng, J. M. Bell, Y. W. Zhang, Y. Gu, *Nanoscale* **2016**, 8, 11177; c) H. Zhan, G. Zhang, Y. Zhang, V. B. C. Tan, J. M. Bell, Y. Gu, *Carbon* **2016**, 98, 232; d) J. F. R. V. Silveira, A. R. Muniz, *Carbon* **2017**, 113, 260; e) H. Zhan, G. Zhang, X. Zhuang, R. Timon, Y. Gu, *Carbon* **2020**, 165, 216.
[63] C. Feng, J. Xu, Z. Zhang, J. Wu, *Carbon* **2017**, 124, 9.
[64] L. W. Zhang, W. M. Ji, K. M. Liew, *Carbon* **2018**, 132, 232.
[65] K. Duan, Y. Li, L. Li, Y. Hu, X. Wang, *Nanoscale* **2018**, 10, 8058.
[66] J. Gao, G. Zhang, B. I. Yakobson, Y. W. Zhang, *Nanoscale* **2018**, 10, 9664.
[67] Y. Wang, X. Dong, X. Tang, H. Zheng, K. Li, X. Lin, L. Fang, G. Sun, X. Chen, L. Xie, C. L. Bull, N. P. Funnell, T. Hattori, A. Sano-Furukawa, J. Chen, D. K. Hensley, G. D. Cody, Y. Ren, H. H. Lee, H. K. Mao, *Angew. Chem. Int. Ed. Engl.* **2019**, 58, 1468.
[68] S. J. Juhl, T. Wang, B. Vermilyea, X. Li, V. H. Crespi, J. V. Badding, N. Alem, *J. Am. Chem. Soc.* **2019**, 141, 6937.
[69] P. Duan, X. Li, T. Wang, B. Chen, S. J. Juhl, D. Koeplinger, V. H. Crespi, J. V. Badding, K. Schmidt-Rohr, *J. Am. Chem. Soc.* **2018**, 140, 7658.
[70] X. Li, M. Baldini, T. Wang, B. Chen, E. S. Xu, B. Vermilyea, V. H. Crespi, R. Hoffmann, J. J. Molaison, C. A. Tulk, M. Guthrie, S. Sinogeikin, J. V. Badding, *J. Am. Chem. Soc.* **2017**, 139, 16343.
[71] T. Wang, P. Duan, E. S. Xu, B. Vermilyea, B. Chen, X. Li, J. V. Badding, K. Schmidt-Rohr, V. H. Crespi, *Nano Lett.* **2018**, 18, 4934.
[72] E. S. Xu, P. E. Lammert, V. H. Crespi, *Nano Lett.* **2015**, 15, 5124.
[73] B. Chen, R. Hoffmann, N. W. Ashcroft, J. Badding, E. Xu, V. Crespi, *J. Am. Chem. Soc.* **2015**, 137, 14373.
[74] D. Stojkovic, P. Zhang, V. H. Crespi, *Phys. Rev. Lett.* **2001**, 87, 125502.
[75] X. D. Wen, R. Hoffmann, N. W. Ashcroft, *J. Am. Chem. Soc.* **2011**, 133, 9023.
[76] S. R. Barua, H. Quanz, M. Olbrich, P. R. Schreiner, D. Trauner, W. D. Allen, *Chem. Eur. J.* **2014**, 20, 1638.
[77] S. Huss, S. Wu, B. Chen, T. Wang, M. C. Gerthoffer, D. J. Ryan, S. E. Smith, V. H. Crespi, J. V. Badding, E. Elacqua, *ACS Nano* **2021**, 15, 4134.
[78] a) Y. Fu, J. Wu, S. Xiao, S. Liu, Z. Zhang, J. He, *Carbon* **2021**, 184, 146; b) B. Chen, V. H. Crespi, R. Hoffmann, *J. Am. Chem. Soc.* **2022**, 144, 9044.
[79] H. T. Huang, L. Zhu, M. D. Ward, T. Wang, B. Chen, B. L. Chaloux, Q. Wang, A. Biswas, J. L. Gray, B. Kuei, G. D. Cody, A. Epshteyn, V. H. Crespi, J. V. Badding, T. A. Strobel, *J. Am. Chem. Soc.* **2020**, 142, 17944.
[80] X. Li, T. Wang, P. Duan, M. Baldini, H. T. Huang, B. Chen, S. J. Juhl, D. Koeplinger, V. H. Crespi, K. Schmidt-Rohr, R. Hoffmann, N. Alem, M. Guthrie, X. Zhang, J. V. Badding, *J. Am. Chem. Soc.* **2018**, 140, 4969.
[81] S. Fanetti, M. Santoro, F. Alabarse, B. Enrico, R. Bini, *Nanoscale* **2020**, 12, 5233.
[82] Z. Zheng, H. Zhan, Y. Nie, X. Xu, Y. Gu, *J. Phys. Chem. C.* **2019**, 123, 28977.
[83] Y. Fu, K. Xu, J. Wu, Z. Zhang, J. He, *Nanoscale* **2020**, 12, 12462.
[84] B. S. Matsuura, S. Huss, Z. Zheng, S. Yuan, T. Wang, B. Chen, J. V. Badding, D. Trauner, E. Elacqua, A. C. T. van Duin, V. H. Crespi, K. Schmidt-Rohr, *J. Am. Chem. Soc.* **2021**, DOI: 10.1021/jacs.1c03671.
[85] X. Wang, X. Yang, Y. Wang, X. Tang, H. Zheng, P. Zhang, D. Gao, G. Che, Z. Wang, A. Guan, J. F. Xiang, M. Tang, X. Dong, K. Li, H. K. Mao, *J. Am. Chem. Soc.* **2022**, 144, 21837.
[86] M. M. Nobrega, E. Teixeira-Neto, A. B. Cairns, M. L. A. Temperini, R. Bini, *Chem. Sci.* **2018**, 9, 254.
[87] M. C. Gerthoffer, B. Xu, S. Wu, J. Cox, S. Huss, S. M. Oburn, S. A. Lopez, V. H. Crespi, J. V. Badding, E. Elacqua, *Polym. Chem.* **2022**, 13, 1359.

[88] S. Romi, S. Fanetti, F. Alabarse, A. M. Mio, R. Bini, *Chem. Sci.* **2021**, 12, 7048.
[89] S. Romi, S. Fanetti, F. G. Alabarse, R. Bini, M. Santoro, *Chem. Mater.* **2022**, 34, 2422.
[90] S. G. Dunning, L. Zhu, B. Chen, S. Chariton, V. B. Prakapenka, M. Somayazulu, T. A. Strobel, *J. Am. Chem. Soc.* **2022**, 144, 2073.
[91] A. Biswas, M. D. Ward, T. Wang, L. Zhu, H. T. Huang, J. V. Badding, V. H. Crespi, T. A. Strobel, *J. Phys. Chem. Lett.* **2019**, 10, 7164.
[92] D. Gao, X. T. J. Xua, X. Yang, P. Z. G. Che, Y. Wang, Y. Chen, X. Gao, X. Dong, H. Zheng, K. Li, H.-k. Mao, *Proc. Natl. Acad. Sci.* **2022**, 119.
[93] J. F. Silveira, A. R. Muniz, *Phys. Chem. Chem. Phys.* **2017**, 19, 7132.
[94] T. Wang, E. S. Xu, B. Chen, R. Hoffmann, V. H. Crespi, *ACS Nano* **2022**, 16, 15884.
[95] P. G. Demingos, A. R. Muniz, *Carbon* **2018**, 140, 644.
[96] S. M. Vasconcelos, N. P. Neme, M. S. C. Mazzoni, *J. Phys. Chem. Lett.* **2021**, 12, 10788.
[97] H. Zhan, G. Zhang, J. M. Bell, Y. Gu, *Carbon* **2016**, 107, 304.
[98] M. Eidani, H. Akbarzadeh, E. Mehrjouei, M. Abbaspour, S. Salemi, H. Yaghoubi, *Colloids Surf. A Physicochem. Eng. Asp.* **2022**, 655.
[99] a) K. Duan, J. Zhang, L. Li, Y. Hu, W. Zhu, X. Wang, *Compos. Sci. Technol.* **2019**, 174, 84; b) W. M. Ji, L. W. Zhang, *Compos. Sci. Technol.* **2019**, 183; c) C. Li, H. Wei, H. Zhan, J. Bai, L. Kou, Y. Gu, *Macromolecules* **2021**, 54, 11486; d) X. Q. Wang, C. L. Chow, D. Lau, *Appl. Mater. Today* **2023**, 32; e) B. B. Yin, J. S. Huang, W. M. Ji, K. M. Liew, *Carbon* **2022**, 200, 10; f) H. Zhan, Y. Zhou, G. Zhang, J. Zhu, W. Zhang, C. Lu, Y. Gu, *Nanoscale* **2021**, 13, 6934; g) L. W. Zhang, W. M. Ji, Y. Hu, K. M. Liew, *Research* **2020**, 2020, 7815462.
[100] a) P. Wang, H. Zhan, Y. Gu, *ACS Appl. Nano Mater.* **2020**, 3, 10218; b) H. Zhan, G. Zhang, J. M. Bell, V. B. C. Tan, Y. Gu, *Nat. Commun.* **2020**, 11, 1905.
[101] a) J. F. R. V. Silveira, A. R. Muniz, *Carbon* **2018**, 139, 789; b) J. F. R. V. Silveira, A. R. Muniz, *J. Membr. Sci.* **2019**, 585, 184.
[102] J. O. Orwa, J. Reiner, A. Juma, A. Stacey, K. Sears, J. A. Schütz, A. Merenda, L. Hyde, R. Guijt, V. R. Adineh, Q. Li, M. Naebe, A. Z. Kouzani, L. F. Dumée, *Diam. Relat. Mater.* **2021**, 115.
[103] Z. Xue, J. Lu, H. Huang, *Diam. Relat. Mater.* **2022**, 128.
[104] A. T. Hendrickson, K. W. Hemawan, M. G. Coco, S. C. Aro, S. A. McDaniel, P. J. Sazio, G. Cook, J. V. Badding, R. J. Hemley, *AIP Adv.* **2020**, 10.
[105] H.-W. Stephan, T. Wang, Y. Tang, *Small* **2021**, 17, e2007529.
[106] A. Zkria, H. Gima, E. Abubakr, A. Mahmoud, A. Haque, T. Yoshitake, *Nanomaterials* **2022**, 12.
[107] Y. Okumura, K. Kanayama, H. Nishiguchi, *P. Combust. Inst.* **2017**, 36, 4409.
[108] a) X. Li, J. Ye, H. Zhang, T. Feng, J. Chen, X. Hu, *Appl. Surf. Sci.* **2017**, 412, 366; b) X. Li, J. Chen, J. Ye, T. Feng, X. Hu, *Diam. Relat. Mater.* **2018**, 81, 176; c) X. Li, C. Li, C. Chen, C. Liu, F. Lyu, M. Jiang, X. Hu, *Appl. Surf. Sci.* **2019**, 487, 464; d) X. Li, C. Wang, C. Chen, M. Jiang, X. Hu, *Appl. Surf. Sci.* **2020**, 532; e) F. Lyu, X. Li, C. Chen, C. Liu, C. Li, M. Jiang, X. Hu, *Appl. Surf. Sci.* **2020**, 528; f) X. Li, F. Xia, C. Wang, C. Chen, M. Jiang, J. Pan, S. Lu, A. A. Khomich, I. Vlasov, X. Hu, *Surf. Coat. Technol.* **2022**, 449.
[109] D. Mukherjee, F. Oliveira, S. C. Trippe, S. Rotter, M. Neto, R. Silva, A. K. Mallik, K. Haenen, C.-M. Zetterling, J. C. Mendes, *Diam. Relat. Mater.* **2020**, 101.
[110] D. Xiang, Z. Su, Y. Li, Z. Zhang, *Diam. Relat. Mater.* **2022**, 130.
[111] S. Mandal, C. Yuan, F. Massabuau, J. W. Pomeroy, J. Cuenca, H. Bland, E. Thomas, D. Wallis, T. Batten, D. Morgan, R. Oliver, M. Kuball, O. A. Williams, *ACS Appl. Mater. Interfaces* **2019**, 11, 40826.
[112] a) S. Zhao, J. Huang, X. Zhou, B. Ren, K. Tang, Y. Xi, L. Wang, L. Wang, Y. Lu, *Appl. Surf. Sci.* **2018**, 434, 260; b) T. Wang, S. Handschuh-Wang, S. Zhang, X. Zhou, Y. Tang, *J. Colloid Interface Sci.* **2017**, 506, 543; c) T. Wang, L. Huang, S. Handschuh-Wang, S. Zhang, X. Li, B. Chen, Y. Yang, X. Zhou, Y. Tang, *Appl. Surf. Sci.* **2018**, 456, 75; d) L. Huang, T. Wang, X. Li, B. Chen, W. Zhang, C.-S. Lee, Y. Tang, *Surf.*

Coat. Technol. **2019**, 357, 870; e) L. Li, Q. Wei, L. Ma, Y. Luo, K. Zhou, M. Yi, B. Deng, Y. Chen, *Int. J. Refract. Hard. Met.* **2020**, 87.

[113] L. Huang, T. Wang, X. Li, X. Wang, W. Zhang, Y. Yang, Y. Tang, *Appl. Surf. Sci.* **2020**, 527.

[114] Z. Tian, L. Zhang, Y. Fang, B. Xu, S. Tang, N. Hu, Z. An, Z. Chen, Y. Mei, *Adv. Mater.* **2017**, 29.

[115] Y. Saiki, T. Bando, T. Harigai, H. Takikawa, T. Hattori, H. Sugita, N. Kawahara, K. Tanaka, *Diam. Relat. Mater.* **2023**, 132.

[116] a) H. Xu, J. Zang, G. Yang, S. Jia, P. Tian, Y. Zhang, Y. Wang, Y. Yu, J. Lu, X. Xu, P. Zhang, *Diam. Relat. Mater.* **2017**, 80, 5; b) H. Xu, J. Zang, P. Tian, Y. Wang, Y. Yu, J. Lu, X. Xu, P. Zhang, *Int. J. Refract. Hard. Met.* **2018**, 71, 147; c) H. Xu, J. Zang, P. Tian, Y. Yuan, Y. Wang, Y. Yu, J. Lu, X. Xu, P. Zhang, *Ceram. Int.* **2018**, 44, 21641; d) H. Xu, J. Zang, G. Yang, P. Tian, Y. Wang, Y. Yu, J. Lu, X. Xu, P. Zhang, *Diam. Relat. Mater.* **2018**, 84, 119; e) M. Zhang, H. Xu, *Tribol. Lett.* **2021**, 155.

[117] S. Mandal, E. L. H. Thomas, L. Gines, D. Morgan, J. Green, E. B. Brousseau, O. A. Williams, *Carbon* **2018**, 130, 25.

[118] a) Y. Takamori, M. Nagai, T. Tabakoya, Y. Nakamura, S. Yamasaki, C. E. Nebel, X. Zhang, T. Matsumoto, T. Inokuma, N. Tokuda, *Diam. Relat. Mater.* **2021**, 118; b) T. Tsuji, H. Ishiwata, T. Sekiguchi, T. Iwasaki, M. Hatano, *Diam. Relat. Mater.* **2022**, 123.

[119] Y. Harada, R. Hishinuma, N. Spătaru, Y. Sakurai, K. Miyasaka, C. Terashima, H. Uetsuka, N. Suzuki, A. Fujishima, T. Kondo, M. Yuasa, *Diam. Relat. Mater.* **2019**, 92, 41.

[120] a) L. Constantin, L. Fan, C. Azina, K. Keramatnejad, J.-F. Silvain, Y. F. Lu, *Cryst. Growth Des.* **2018**, 18, 2458; b) L. S. Fan, L. Constantin, D. W. Li, L. Liu, K. Keramatnejad, C. Azina, X. Huang, H. R. Golgir, Y. Lu, Z. Ahmadi, F. Wang, J. Shield, B. Cui, J. F. Silvain, Y. F. Lu, *Light-Sci. Appl.* **2018**, 7, 17177.

[121] a) P. Forsberg, P. Hollman, M. Karlsson, *Analyst* **2021**, 146, 6981; b) X. Wang, M. Karlsson, P. Forsberg, M. Sieger, F. Nikolajeff, L. Osterlund, B. Mizaikoff, *Anal Chem* **2014**, 86, 8136; c) A. Teuber, G. Caniglia, M. Wild, M. Godejohann, C. Kranz, B. Mizaikoff, *ACS Sens* **2023**, 8, 1871; d) J. Haas, E. V. Catalan, P. Piron, F. Nikolajeff, L. Osterlund, M. Karlsson, B. Mizaikoff, *ACS Omega* **2018**, 3, 6190.

[122] Á. I. López-Lorente, P. Wang, M. Sieger, E. Vargas Catalan, M. Karlsson, F. Nikolajeff, L. Österlund, B. Mizaikoff, *Phys. Status Solidi A* **2016**, 213, 2117.

[123] J. Haas, E. V. Catalan, P. Piron, M. Karlsson, B. Mizaikoff, *Analyst* **2018**, 143, 5112.

[124] F. Piazza, C. Kelvin, M. Monthioux, P. Puech, I. Gerber, *Carbon* **2020**, 169, 129.

[125] F. Piazza, K. Gough, M. Monthioux, P. Puech, I. Gerber, R. Wiens, G. Paredes, C. Ozoria, *Carbon* **2019**, 145, 10.

[126] a) M. Jiang, C. Chen, P. Wang, D. Guo, S. Han, X. Li, S. Lu, X. Hu, *Proc. Natl. Acad. Sci.* **2022**, 119, e2201451119; b) X. Hu, C. Chen, S. Lu, *Carbon* **2016**, 98, 671; c) X. J. Hu, J. S. Ye, H. Hu, X. H. Chen, Y. G. Shen, *Appl. Phys. Lett.* **2011**, 99; d) C. Chen, Y. Li, D. Guo, C. Ke, D. Fan, S. Lu, X. Li, M. Jiang, X. Hu, *ACS Appl Mater Interfaces* **2023**, 15, 30684.

[127] a) L. G. Pimenta Martins, D. L. Silva, J. S. Smith, A.-Y. Lu, C. Su, M. Hempel, C. Occhialini, X. Ji, R. Pablo, R. S. Alencar, A. C. R. Souza, A. A. Pinto, A. B. de Oliveira, R. J. C. Batista, T. Palacios, M. S. C. Mazzoni, M. J. S. Matos, R. Comin, J. Kong, L. G. Cançado, *Carbon* **2021**, 173, 744; b) F. Ke, L. Zhang, Y. Chen, K. Yin, C. Wang, Y. K. Tzeng, Y. Lin, H. Dong, Z. Liu, J. S. Tse, W. L. Mao, J. Wu, B. Chen, *Nano Lett.* **2020**, 20, 5916; c) F. Piazza, M. Monthioux, P. Puech, I. C. Gerber, *Carbon* **2020**, 156, 234.

[128] a) P. V. Bakharev, M. Huang, M. Saxena, S. W. Lee, S. H. Joo, S. O. Park, J. Dong, D. C. Camacho-Mojica, S. Jin, Y. Kwon, M. Biswal, F. Ding, S. K. Kwak, Z. Lee, R. S. Ruoff, *Nat. Nanotechnol.* **2020**, 15, 59; b) B. Mortazavi, F. Shojaei, B. Javvaji, M. Azizi, H. Zhan, T. Rabczuk, X. Zhuang, *Appl. Surf. Sci.* **2020**, 528; c) T. Cheng, Z. Liu, Z. Liu, *J. Mater. Chem. C* **2020**, 8, 13819; d) M. Raeisi, B. Mortazavi, E. V. Podryabinkin, F. Shojaei, X. Zhuang, A. V. Shapeev, *Carbon* **2020**, 167, 51; e) X. Chen, M. Dubois, S. Radescu, A. Rawal, C. Zhao, *Carbon* **2021**, 175, 124; f) H. Shu, *Phys. Chem. Chem. Phys.* **2021**, 23, 18951; g) H. Shu, *J. Mater. Chem. C* **2021**, 9, 4505.

[129] a) Y. Gao, T. Cao, F. Cellini, C. Berger, W. A. de Heer, E. Tosatti, E. Riedo, A. Bongiorno, *Nat. Nanotechnol.* **2018**, 13, 133; b) J. Shi, K. Cai, Y. M. Xie, *Mater. Des.* **2018**, 156, 125; c) F. Cellini, F. Lavini, C. Berger, W. de Heer, E. Riedo, *2D Mater.* **2019**, 6; d) M. Rejhon, X. Zhou, F. Lavini, A. Zanut, F. Popovich, L. Schellack, L. Witek, P. Coelho, J. Kunc, E. Riedo, *Adv. Sci.* **2023**, 10; e) F. Cellini, F. Lavini, T. Cao, W. de Heer, C. Berger, A. Bongiorno, E. Riedo, *FlatChem* **2018**, 10, 8.

[130] a) A. P. Barboza, M. H. Guimaraes, D. V. Massote, L. C. Campos, N. M. Barbosa Neto, L. G. Cancado, R. G. Lacerda, H. Chacham, M. S. Mazzoni, B. R. Neves, *Adv. Mater.* **2011**, 23, 3014; b) L. G. P. Martins, M. J. S. Matos, A. R. Paschoal, P. T. C. Freire, N. F. Andrade, A. L. Aguiar, J. Kong, B. R. A. Neves, A. B. de Oliveira, M. S. C. Mazzoni, A. G. S. Filho, L. G. Cancado, *Nat. Commun.* **2017**, 8, 96.

[131] S. V. Erohin, Q. Ruan, P. B. Sorokin, B. I. Yakobson, *Small* **2020**, 16, e2004782.

[132] B. Liu, E. Emmanuel, T. Liang, B. Wang, *Nanoscale* **2023**, 15, 10498.

[133] K. D. Pham, *New J. Chem.* **2022**, 46, 9383.

[134] B. Javvaji, B. Mortazavi, X. Zhuang, T. Rabczuk, *Carbon* **2021**, 185, 558.

[135] a) D. Odkhuu, D. Shin, R. S. Ruoff, N. Park, *Sci Rep* **2013**, 3, 3276; b) G. Qin, L. Wu, H. Gou, *Functional Diamond* **2021**, 1, 83.

[136] a) K. Cai, L. Wang, Y. M. Xie, *Mater. Des.* **2018**, 149, 34; b) L. Wang, K. Cai, J. Shi, Q.-H. Qin, *Appl. Surf. Sci.* **2020**, 527; c) L. Wang, K. Cai, S. Wei, Y. M. Xie, *Phys. Chem. Chem. Phys.* **2018**, 20, 21136.

[137] S. Rajasekaran, F. Abild-Pedersen, H. Ogasawara, A. Nilsson, S. Kaya, *Phys. Rev. Lett.* **2013**, 111, 085503.

[138] T. Pakornchote, A. Ektarawong, B. Alling, U. Pinsook, S. Tancharakorn, W. Busayaporn, T. Bovornratanaraks, *Carbon* **2019**, 146, 468.

[139] Y.-C. Wu, J.-L. Shao, Z. Zheng, H. Zhan, *J. Phys. Chem. C.* **2020**, 125, 915.

[140] Z. Zheng, H. Zhan, Y. Nie, X. Xu, D. Qi, Y. Gu, *Carbon* **2020**, 161, 809.

[141] L. Zhu, W. Li, F. Ding, *Nanoscale* **2019**, 11, 4248.

[142] C. Li, Y. Nie, H. Zhan, J. Bai, T. Liu, Y. Gu, *Compos. Sci. Technol.* **2022**, 230.

[143] H. Zhan, B. Dong, G. Zhang, C. Lu, Y. Gu, *Small* **2022**, 18, e2203887.

[144] Z. Lu, N. Huang, Z. Zhai, B. Chen, L. Liu, H. Song, Z. Yuan, C. Zhang, B. Yang, X. Jiang, *J. Mater. Sci. Technol.* **2022**, 105, 26.

[145] L. Zhang, K. Zhou, Q. Wei, L. Ma, W. Ye, H. Li, B. Zhou, Z. Yu, C.-T. Lin, J. Luo, X. Gan, *Appl. Energy* **2019**, 233-234, 208.

[146] a) M. Fronzi, J. Bishop, A. A. Martin, M. H. N. Assadi, B. Regan, C. Stampfl, I. Aharonovich, M. J. Ford, M. Toth, *Carbon* **2020**, 164, 51; b) L. Li, X. Chen, W. Zhang, K. Peng, *Int. J. Refract. Hard. Met.* **2018**, 71, 129.

[147] a) Y. Jiang, Z. Deng, B. Zhou, Q. Wei, H. Long, Y. Wang, J. Li, N. Hu, L. Ma, C.-T. Lin, Z. Yu, K. Zhou, *Appl. Surf. Sci.* **2018**, 428, 264; b) Y. Li, H. Li, M. Li, C. Li, Y. Lei, D. Sun, B. Yang, *J. Alloys Compd.* **2018**, 743, 187; c) Q. Yuan, Y. Liu, C. Ye, H. Sun, D. Dai, Q. Wei, G. Lai, T. Wu, A. Yu, L. Fu, K. W. A. Chee, C. T. Lin, *Biosens. Bioelectron.* **2018**, 111, 117; d) S. Tulic, T. Waitz, M. Caplovicova, G. Habler, M. Varga, M. Kotlar, V. Vretenar, O. Romanyuk, A. Kromka, B. Rezek, V. Skakalova, *ACS Nano* **2019**, 13, 4621.

[148] X. Mei, Q. Wei, H. Long, Z. Yu, Z. Deng, L. Meng, J. Wang, J. Luo, C.-T. Lin, L. Ma, K. Zheng, N. Hu, *Electrochim. Acta* **2018**, 271, 84.

[149] J. Zhang, X. Yu, Z.-Q. Zhang, Z.-Y. Zhao, *Appl. Surf. Sci.* **2020**, 506.

[150] a) M. Baroch, S. Baluchová, A. Taylor, L. Míka, J. Fischer, H. Dejmková, V. Mortet, S. Sedláková, L. Klimša, J. Kopeček, K. Schwarzová-Pecková, *Electrochim. Acta* **2022**, 426; b) P. Ashcheulov, O. Hák, S. Sedláková, A. Taylor, S. Baluchová, K. Schwarzová-Pecková, M. Davydova, J. Kopeček, L. Klimša, M. Vondráček, J. Honolka, V. Mortet, *Adv. Mater. Interfaces* **2022**, 9.

[151] J. Xu, N. Yang, S. Heuser, S. Yu, A. Schulte, H. Schönherr, X. Jiang, *Adv. Energy Mater.* **2019**, 9.

[152] Y. Meng, L. Zhang, R. Xing, H. Huang, Y. Qu, T. Jiao, J. Zhou, Q. Peng, *Colloids Surf. A Physicochem.*

Eng. Asp. **2018**, 555, 787.

[153] S. Yu, N. Yang, H. Zhuang, S. Mandal, O. A. Williams, B. Yang, N. Huang, X. Jiang, *J. Mater. Chem. A* **2017**, 5, 1778.

[154] Z. Lu, L. Liu, W. Gao, Z. Zhai, H. Song, B. Chen, Z. Zheng, B. Yang, C. Geng, J. Liang, X. Jiang, N. Huang, *Sep. Purif. Technol.* **2022**, 302.

[155] a) J.-M. Cho, H.-J. Lee, Y.-J. Ko, H.-J. Choi, Y.-J. Baik, G. W. Hwang, J.-K. Park, J. Y. Kwak, J. Kim, J. Park, Y. Jeong, I. Kim, K.-S. Lee, W.-S. Lee, *Surf. Interfaces* **2022**, 34; b) J. Wang, Z. He, X. Tan, T. Wang, L. Liu, X. He, X. D. Liu, L. Zhang, K. Du, *Carbon* **2020**, 160, 71.

[156] a) S. Deshmukh, K. J. Sankaran, D. Banerjee, C.-J. Yeh, K.-C. Leou, D. M. Phase, M. Gupta, I. N. Lin, K. Haenen, S. S. Roy, P. R. Waghmare, *J. Mater. Chem. A* **2019**, 7, 19026; b) X. Jia, N. Huang, Y. Guo, L. Liu, P. Li, Z. Zhai, B. Yang, Z. Yuan, D. Shi, X. Jiang, *J. Mater. Sci. Technol.* **2018**, 34, 2398; c) C. Zhang, N. Huang, Z. Zhai, L. Liu, B. Chen, Z. Lu, M. Zhou, H. Song, D. Shi, B. Yang, N. Yang, X. Jiang, *Nanotechnology* **2021**, 33.

[157] a) S. Yu, K. J. Sankaran, S. Korneychuk, J. Verbeeck, K. Haenen, X. Jiang, N. Yang, *Nanoscale* **2019**, 11, 17939; b) K. J. Sankaran, C. J. Yeh, P. Y. Hsieh, P. Pobedinskas, S. Kunuku, K. C. Leou, N. H. Tai, I. N. Lin, K. Haenen, *ACS Appl. Mater. Interfaces* **2019**, 11, 25388.

[158] Z. Zhai, N. Huang, B. Yang, C. Wang, L. Liu, J. Qiu, D. Shi, Z. Yuan, Z. Lu, H. Song, M. Zhou, B. Chen, X. Jiang, *J. Phys. Chem. C.* **2019**, 123, 6018.

[159] a) Z. Zhai, N. Huang, H. Zhuang, L. Liu, B. Yang, C. Wang, Z. Gai, F. Guo, Z. Li, X. Jiang, *Appl. Surf. Sci.* **2018**, 457, 1192; b) Z. Zhai, N. Huang, X. Jiang, *Curr. Opin. Electrochem.* **2022**, 32.

[160] D. Banerjee, K. J. Sankaran, S. Deshmukh, C.-J. Yeh, M. Gupta, I. N. Lin, K. Haenen, A. Kanjilal, S. Sinha Roy, *Electrochim. Acta* **2021**, 397.

[161] a) K. Siuzdak, M. Ficek, M. Sobaszek, J. Ryl, M. Gnyba, P. Niedzialkowski, N. Malinowska, J. Karczewski, R. Bogdanowicz, *ACS Appl. Mater. Interfaces* **2017**, 9, 12982; b) M. Sobaszek, K. Siuzdak, J. Ryl, M. Sawczak, S. Gupta, S. B. Carrizosa, M. Ficek, B. Dec, K. Darowicki, R. Bogdanowicz, *J. Phys. Chem. C.* **2017**, 121, 20821; c) K. J. Sankaran, M. Ficek, S. Kunuku, K. Panda, C. J. Yeh, J. Y. Park, M. Sawczak, P. P. Michalowski, K. C. Leou, R. Bogdanowicz, I. N. Lin, K. Haenen, *Nanoscale* **2018**, 10, 1345.

[162] a) W. F. Paxton, J. L. Rozsa, M. M. Brooks, M. P. Running, D. J. Schultz, J. B. Jasinski, H. J. Jung, M. Z. Akram, *J. Nanobiotechnology* **2021**, 19, 458; b) Z. Zhai, B. Leng, N. Yang, B. Yang, L. Liu, N. Huang, X. Jiang, *Small* **2019**, 15, e1901527; c) N. F. Santos, S. O. Pereira, A. J. S. Fernandes, T. L. Vasconcelos, C. M. Fung, B. S. Archanjo, C. A. Achete, S. R. Teixeira, R. F. Silva, F. M. Costa, *ACS Appl. Mater. Interfaces* **2019**, 11, 8470; d) S. K. Sethy, M. Ficek, K. J. Sankaran, S. Sain, A. R. Tripathy, S. Gupta, J. Ryl, S. Sinha Roy, N. H. Tai, R. Bogdanowicz, *ACS Appl. Mater. Interfaces* **2021**, 13, 55687; e) M. Zhou, Z. Zhai, L. Liu, C. Zhang, Z. Yuan, Z. Lu, B. Chen, D. Shi, B. Yang, Q. Wei, N. Huang, X. Jiang, *Appl. Surf. Sci.* **2021**, 551.

[163] K. Panda, J. E. Kim, K. J. Sankaran, I. N. Lin, K. Haenen, G. S. Duesberg, J. Y. Park, *Nanoscale* **2021**, 13, 7308.

[164] a) H. Li, B. Yang, J. Lu, X. Guo, B. Yu, Y. Xiong, N. Huang, L. Liu, G. Xu, X. Jiang, *Appl. Surf. Sci.* **2022**, 599; b) H. Qu, H. Liu, B. Wang, L. Jiang, P. Zhang, G. Liu, Y. Xiong, *Diam. Relat. Mater.* **2022**, 121.

[165] a) Z. Zhai, N. Huang, B. Yang, L. Liu, H. Li, J. Chen, B. Zhang, X. Jiang, *ACS Appl. Mater. Interfaces* **2020**, 12, 8522; b) M. Ficek, B. Dec, K. J. Sankaran, K. Gajewski, P. Tatarczak, I. Wlasny, A. Wysmolek, K. Haenen, T. Gotszalk, R. Bogdanowicz, *Adv. Mater. Interfaces* **2021**, 8; c) W. Zhang, L. Guan, B. Wang, H. Liu, J. Wang, X. Hong, J. Long, S. Wei, X. Xiong, Y. Xiong, *J. Alloys Compd.* **2022**, 928.

[166] a) D. Banerjee, K. J. Sankaran, S. Deshmukh, M. Ficek, G. Bhattacharya, J. Ryl, D. M. Phase, M. Gupta, R. Bogdanowicz, I. N. Lin, A. Kanjilal, K. Haenen, S. S. Roy, *J. Phys. Chem. C.* **2019**, 123, 15458; b) J. Long, L. Guan, J. Wang, H. Liu, B. Wang, Y. Xiong, *Carbon* **2022**, 197, 400.

[167] Q. Tao, X. Wei, M. Lian, H. Wang, X. Wang, S. Dong, T. Cui, P. Zhu, *Carbon* **2017**, 120, 405.

[168] a) E. O. Hall, *Proc. Phys. Soc. B* **1951**, 64, 747; b) N. J. Petch, *J. Iron Steel Inst.* **1953**, 174, 25.
[169] a) X. Li, Y. Wei, L. Lu, K. Lu, H. Gao, *Nature* **2010**, 464, 877; b) B. Li, H. Sun, C. Chen, *Nat Commun* **2014**, 5, 4965; c) Q. An, K. M. Reddy, J. Qian, K. J. Hemker, M. W. Chen, W. A. Goddard, III, *Nat Commun* **2016**, 7, 11001.
[170] a) M. A. Meyers, A. Mishra, D. J. Benson, *Progress in Materials Science* **2006**, 51, 427; b) H. Tang, X. Yuan, P. Yu, Q. Hu, M. Wang, Y. Yao, L. Wu, Q. Zou, Y. Ke, Y. Zhao, L. Wang, X. Li, W. Yang, H. Gou, H.-k. Mao, W. L. Mao, *Carbon* **2018**, 129, 159.
[171] W. Hu, B. Wen, Q. Huang, J. Xiao, D. Yu, Y. Wang, Z. Zhao, J. He, Z. Liu, B. Xu, Y. Tian, *Science China Materials* **2017**, 60, 178.
[172] L. Lu, X. Chen, X. Huang, K. Lu, *Science* **2009**, 323, 607.
[173] Q. Huang, D. Yu, B. Xu, W. Hu, Y. Ma, Y. Wang, Z. Zhao, B. Wen, J. He, Z. Liu, Y. Tian, *Nature* **2014**, 510, 250.
[174] Y. Yue, Y. Gao, W. Hu, B. Xu, J. Wang, X. Zhang, Q. Zhang, Y. Wang, B. Ge, Z. Yang, Z. Li, P. Ying, X. Liu, D. Yu, B. Wei, Z. Wang, X. F. Zhou, L. Guo, Y. Tian, *Nature* **2020**, 582, 370.
[175] Y. Pan, P. Ying, Y. Gao, P. Liu, K. Tong, D. Yu, K. Jiang, W. Hu, B. Li, B. Liu, Z. Zhao, J. He, B. Xu, Z. Liu, Y. Tian, *Proc Natl Acad Sci U S A* **2021**, 118.
[176] C. Xu, G. He, C. Liu, H. Wang, *Ceram. Int.* **2018**, 44, 22121.
[177] B. Li, H. Sun, C. Chen, *Phys Rev Lett* **2016**, 117, 116103.
[178] L. Sun, X. He, J. Lu, *Carbon* **2018**, 127, 320.
[179] J. Xiao, H. Yang, X. Wu, F. Younus, P. Li, B. Wen, X. Zhang, Y. Wang, Y. Tian, *Sci. Adv.* **2018**, 4.
[180] B. Wen, B. Xu, Y. Wang, G. Gao, X.-F. Zhou, Z. Zhao, Y. Tian, *npj Computational Materials* **2019**, 5.
[181] J. Xiao, B. Wen, B. Xu, X. Zhang, Y. Wang, Y. Tian, *npj Computational Materials* **2020**, 6.
[182] B. Yang, X. Peng, C. Huang, Z. Wang, D. Yin, T. Fu, *Carbon* **2019**, 150, 1.
[183] Y. Zeng, Q. Zhang, Y. Wang, J. Jiang, H. Xing, X. Li, *Phys Rev Lett* **2021**, 127, 066101.
[184] a) T. Jin, M. Ma, B. Li, Y. Gao, Q. Zhao, Z. Zhao, J. Chen, Y. Tian, *Carbon* **2020**, 161, 1; b) T. Jin, J. Chen, T. Zhao, Q. Zhao, Y. Tian, *Journal of Materials Processing Technology* **2021**, 294.

Yao Li received her master's degree from Wuhan Institute of Technology (Wuhan, China), in 2021. She entered the University of Siegen (Siegen, Germany) in 2021 and is pursuing her doctor degree under supervision of Prof. Xin Jiang and Prof. Nianjun Yang. Her research interest focuses on design of polycrystalline diamond nanostructures and the application in electrochemical sensing.

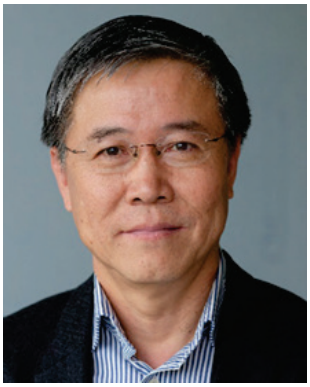

Dr. Xin Jiang has been a professor and the Chair holder of Surface and Materials Technology at University of Siegen (Siegen, Germany) since 2003. He was a Changjiang-Visiting Chair Professor at Dalian University and Science and Technology, China. His current research interests are on the growth, characterization and application of thin diamond film as well as functional nanomaterials.

Dr. Yang Lu has been one of "HKU-100 Scholar" professors in the Department of Mechanical Engineering at University of Hong Kong (Hong Kong, China) since 2023. He is an elected member of the Hong Kong Young Academy of Sciences (YASHK) in 2022. His research interests focus on experimental nanomechanics and nanomanufacturing.

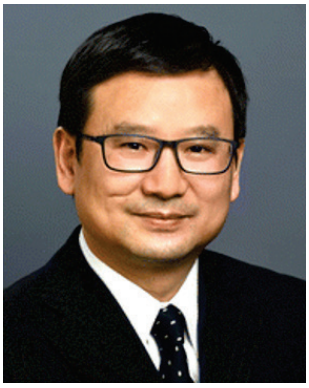

Dr. Nianjun Yang has been a professor of Electrochemistry and Catalysis at the Department of Chemistry and Institute of Materials Research (IMO-IMOEC) of Hasselt University (Dipenbeek, Belgium) since 2023. He works on the growth and characterization of functional materials especially carbon materials) as well as their electrochemical applications.

Diamond Nanostructures at Different Dimensions: Synthesis and Applications

Yao Li, Limin Yang, Xin Jiang, Yang Lu*, Cuiping Han, Yongbing Tang, Nianjun Yang**

This review article overviews the progress and achievements of the synthesis and applications of diamond materials at different nanoscales, including the newly born one-dimensional diamond nanothreads, two-dimensional diamanes, as well as nt-diamond grains. Their challenges and future perspectives are outlined and discussed.